THE UNIVERSITY OF MANITOBA

MICROSTRUCTURAL RESPONSES OF A NICKEL-BASE CAST IN-738 SUPERALLOY TO A VARIETY OF PRE-WELD HEAT-TREATMENTS

by

ANURAG THAKUR

A thesis

submitted to the faculty of graduate

studies in partial fulfillment of the

requirements for the degree of

Master of Science

METALLURGICAL SCIENCES LABORATORY

DEPARTMENT OF MECHANICAL AND INDUSTRIAL ENGINEERING

WINNIPEG, MANITOBA

SEPTEMBER 1997

THE UNIVERSITY OF MANITOBA

FACULTY OF GRADUATE STUDIES

*****

COPYRIGHT PERMISSION PAGE

MICROSTRUCTURAL RESPONSES OF A NICKEL BASE CAST IN-738 SUPERALLOY TO A VARIETY OF PRE-WELD HEAT-TREATMENTS

BY

ANURAG THAKUR

A Thesis/Practicum submitted to the Faculty of Graduate Studies of The University of Manitoba in partial fulfillment of the requirements of the degree

of

MASTER OF SCIENCE

Master of Science 1997 (c)

ACKNOWLEDGMENTS

I acknowledge Dr. M.C.Chaturvedi for extending me the opportunity to work on this project. I am extremely grateful to him for not only accepting me as a student but for his sincere guidance throughout the course of this work. I acknowledge Dr. N.L.Richards of Bristol Aerospace Ltd., for his active involvement and never-faltering encouragement. Many useful discussions with Dr. Qiang Xu are also gratefully acknowledged.

I acknowledge the financial support provided by Manitoba Hydro, Winnipeg, in the form of a research assistantship during the course of this investigation. I am thankful to Don Mardis and John Van Dorp for their technical assistance. Ending on a personal note, I am grateful to my fiancee, Leena, for her love and inspiration.

ABSTRACT

This dissertation reports an investigation involving a thorough characterization of the microstructural response of cast IN-738 to a variety of pre-weld heat-treatment schemes. The as-received material showed cored dendritic microstructure, containing coarse grains, about 0.5% casting micropores, 0.7% primary carbide particles, and 42% primary γ' particles respectively. The volume-fraction of primary γ' particles decreased continuously from 20.1% to about 5% for solution-treatment temperatures (STT) in the range of 1120^0C-1225^0C. The volume-fraction analysis indicated that the solvus of primary γ' particles was higher than the 1160^0C-1175^0C range suggested by Steven and Flewitt[27]. The brine quenched samples from the STT manifested an extensive intergranular cracking, primarily due to quenching stresses and the aging contraction stresses due to an inherent fast precipitation of the secondary γ' particles. Aging resulted in coarsening of primary and secondary γ' particles, degeneration and dissociation of primary carbide particles to form secondary γ' particles and fine $M_{23}C_6$ carbide particles on the grain-boundaries, which were initially present as discrete particles and changed to a continuos distribution with continued aging. Only long term aging showed the presence of these secondary carbide particles in the grain interiors. Aging at 845^0C, after solution-treating at 1120^0C showed a distinct bimodal distribution of γ' particles, consisting of primary cuboidal γ' particles of about 420nm edge length and spheroidal secondary γ' particles of 90nm diameter. The overaged microstructure for the 1175^0C and 1225^0C consisted of a unimodal distribution of degenerate γ' particles. The activation energy for the coarsening of secondary γ'

particles using the LSEM theory was 241 KJ/molK and is in a reasonable agreement with the value of 259KJ/molK calculated by Henderson etal.[45]. Grain-boundary $M_{23}C_6$ carbide particles have a solvus of about 1025^0C and liquate/dissolve at higher temperatures. The liquation of low melting continuously linked fine carbide particles on the boundaries was another sole cause for intergranular quench cracks in this material. The coherency strains are usually responsible for heat affected zone microfissuring in this material and were found to be always lower for the overaged material as compared to the peak-aged and the underaged material.

TABLE OF CONTENTS

LIST OF TABLES

LIST OF FIGURES

Chapter 1

INTRODUCTION

The mechanical, physical and chemical properties of the multi-component, multi-phase, cast Ni-base superalloy IN-738 used in the critical parts of gas turbines are determined by a precariously balanced composition and microstructure produced by appropriate casting and pre-heat treatment practices. The alloy derives its strength by the precipitates of γ' (Ni_3Al,Ti) phase, but other phases such as MC and $M_{23}C_6$ carbides are also present in the austenitic, γ, matrix. The strength of the alloy is dependent on factors such as volume-fraction, particle size and distribution, coarsening rate, and the lattice misfit of γ' phase. All of these factors can be controlled to varying degrees by heat-treatments; but since the standard heat-treatment practice has evolved empirically, little is known quantitatively about the influence of time and temperature on the γ', MC and $M_{23}C_6$ particles and what is known is not very reliable. It has been suggested that the solvus of γ' is in the range of 1,160°C - 1,175°C but specimens solution-treated at 1,175°C and 1,225°C during the course of this study contained a measurable volume fraction of primary γ' precipitates.

The microstructure of IN-738, even after an optimizing heat-treatment is frequently metastable at elevated temperatures. This is due to the fact that aging heat-treatments are performed in the same temperature range as the operating temperatures for the components made from IN-738. This metastability accounts for changes in

morphology, composition, distribution and mechanical properties of various phases(major and minor) during exposure at elevated temperatures and stressful conditions. In addition, reactions between phases will take place which may result in the occurrence of undesirable phases. These factors lead to an undesirable situation of heat affected zone(HAZ) cracking in cast IN 738 during weld repairs.

Therefore, a project was designed with the aim of developing a suitable microstructure through an appropriate heat-treatment scheme, which would resist HAZ cracking during weld repairs of cast IN738 components. This particular research is a precursor to the larger problem of developing weld repair techniques and it involves a thorough characterization of the microstructural responses of IN 738 to a variety of heat-treatment schemes. Very little information is available on this topic in the open literature.

This research work aims at addressing microstructural aspects of variously heat-treated IN-738 in a systematic manner. Firstly, the microstructural response of IN738 subjected to a spectrum of heat-treatments was established. The next step was the formulation of the coarsening kinetics of secondary γ' particles at a standard aging temperature following the solution-treatments at various temperatures, and the calculation of activation energy for coarsening. This was followed by establishing the role of grain boundary $M_{23}C_6$ carbides in crack initiation and propagation in heat-treated specimens. Finally, the precipitation strengthening contribution was evaluated utilizing established formulations. This contribution led to the back calculation of coherency strains, which result due to the precipitation of secondary γ' particles. These strains can be critical in determining the fracture behavior of the material.

These results have provided a better understanding of microstructural behavior in IN 738 specimens and should help in designing a specific heat-treatment scheme which would result in a more desirable microstructure. Such a microstructure would minimize, if not eliminate, the HAZ microfissuring during weld repairs. In this dissertation the physical metallurgy, especially the microstructural aspect of IN-738 superalloy is first reviewed. The effect of various heat treatments on the microstructures and precipitation of various phases studied by various metallographic techniques are then presented.

Chapter 2

LITERATURE REVIEW

The Inconel-738 is a cast Ni-Cr-Co base superalloy developed at the Paul D. Merica Research Laboratory [1]. The objective of its development was to produce a structurally-stable cast alloy combining the strength of IN-713 with the oxidation and sulfidation resistance of Udimet-500. It is a vacuum-melted, vacuum-cast precipitation-hardenable Ni-base superalloy possessing excellent high temperature creep-rupture strength combined with hot corrosion resistance superior to that of many high-strength superalloys of lower Cr content. It can be used effectively up to a temperature of 980°C. The tensile properties of IN-738 are superior to, and elevated temperature stress-rupture properties are comparable to those of the widely-used alloy IN-713 C along with substantially better sulfidation resistance[2].

The largest use of this alloy is in the industrial gas turbine industry for engine parts that are required to withstand high temperature and stress combined with corrosion resistance[3]. Applications of the alloy are primarily for components, such as blades, vanes, and integral wheels [1,3].

A significant feature of IN-738 superalloy is its thermodynamic metastability which results in changes in morphology, composition, distribution and properties of various phases (major & minor) during exposure at elevated temperatures, with or without superimposed stresses, and varying environments. In addition, reactions between phases

can take place which may result in the occurrence of undesirable phases, which may lead to cracking [5]. Welding is one of the commonly used methods of repairing the gas turbine components made from IN-738. However, cast IN-738 is very sensitive to hot cracking during welding and to the development of cracks in the welded metai and heat-affected zone during post-weld heat-treatments. One of the key factors in determining the susceptibility of an alloy to hot cracking or HAZ cracking is its microstructure. The microstructure of IN 738 is very complex and is influenced by composition, presence of trace elements, heat-treatment, melting and casting route used, as well as service exposure. Therefore, the effect of these factors on microstructure of IN738 is reviewed next.

2.1 Melting and Casting Practices

IN-738 is normally vacuum-melted and vacuum-investment-cast with procedures similar to those used for other cast Ni-base superalloys. Typical casting conditions are: 200-400^{0}F superheat above the liquidus temperature and a mold preheat 1,500-1,800^{0}F [6]. This alloy is prone to the formation of microporosity during solidification. Hot isostatic pressing (HIP), which involves the application of isostatic pressure in argon at a high temperature, can be used to partially eliminate microporosity and its detrimental effects.

2.2 Composition

Two versions of cast IN-738 alloy are produced: a high carbon version (C

~ 0.15-0.20 wt.%) designated as IN-738C and a low carbon version designated IN-738 LC (C ~ 0.09-0.13 wt%). Low carbon is needed in this alloy for improved castability in larger sections. Tensile and stress-rupture properties are not appreciably affected by the lower carbon content [2]. The material used in the present investigation was a low carbon version and its nominal composition is given in Table 1.

Table 1. Alloy IN-738 Nominal Composition

Element	Wt%
Carbon (C)	0.11
Cobalt (Co)	8.50
Chromium (Cr)	16.0
Molybdenum (Mo)	1.75
Tungsten (W)	2.60
Tantalum (Ta) + Niobium (Nb)	2.65
Titanium (Ti)	3.40
Aluminum (Al)	3.40
Iron (Fe)	LAP*
Manganese (Mn)	LAP
Phosphorous (P)	LAP
Sulfur (S)	LAP
Silicon (Si)	LAP

* low as possible, Boron could be present in the material

The composition was designed using the electron vacancy number criteria in order to achieve a reasonably stable microstructure free from the brittle sigma (σ) phase.

The physical and mechanical properties of the cast alloy IN-738 are listed in Table 2.

Table 2 Mechanical, Physical, and Elastic Properties of Cast IN-738[6]

PHYSICAL PROPERTIES		MECHANICAL PROPERTIES				ELASTIC PROPERTIES	
Melting Range	1232-1315°C	Temperature (°C)	Stress ($\sigma_{U.T.S.}$, MPa)	Stress (σ_Y, MPa)	Elongation (%)	Poisson's Ratio	0.29
		21	1100	915	5		
Density	8.11 gm/cm^3	760	965	795	6.5	Young's Modulus	200.2 GPA
		980	455	345	13		
Coefficient of Thermal Expansion	15.36x10^{-6}/°C					Shear Modulus	78 GPA
Electron Vacancy No.	< 2.36*	Fatigue Strength (Service Temperature Range), (R=0), Fully Heat -Treated					
		Cycles	Strength(KSI)				
		10^6	55-60				
		10^7	45-52				
		10^8	35-45				
		Charpy Impact Strength(Unnotched (21°C)			37 Ft-lb		

* Electron vacancy number greater than 2.36 results in the formation of a brittle phase sigma (σ).

2.3 Strengthening mechanisms for IN-738

The high strength of IN-738 is due to the following mechanisms: solid-solution strengthening from chromium, molybdenum, tungsten and cobalt; precipitation hardening from a gamma prime (γ') phase consisting of $Ni_3(Al,Ti)$; and grain boundary strengthening by carbides.

2.3.1 Solid Solution Strengthening

Co, Cr, Mo, W, Ti and Al are all solid-solution hardeners in Nickel. The elements differ with Nickel in atomic diameter and concentration from 1% to 13%. The change in lattice parameter, depending on the atomic diameter of different species, can be related to the hardening observed in the alloy. Solute atoms interact with a moving dislocation and stacking faults during the dislocation glide (short range obstacles). Introduction of a substitutional solute atom into the crystal produces a lattice distortion that typically gives rise to a spherically symmetrical stress field surrounding the solute atom. The stress field of the atom can interact with the stress field of a dislocation, giving rise to solute atom-dislocation interaction. The modulus of a substitutional solute atom relative to that of the solvent also plays a role in solid-solution strengthening.

Both the size and the modulus effects produce a dislocation-solute atom interaction energy that is elastic in nature. It is surprising that a 'soft' atom will harden a crystal to a greater degree than a 'hard' one [8]. The strength of solid solution strengthening can be estimated by taking all the precipitates into solution and measuring the increase in hardness over that of pure nickel.

2.3.2 Precipitation Hardening Mechanisms

The main strength of IN-738 is due to the precipitation hardening by $Ni_3(Al\text{-}Ti)$ gamma prime intermetallic compound. Precipitate particles can impede the motion of dislocations through a variety of interaction mechanisms [9]. Those for which theories have been developed include:

1) chemical strengthening, which results from the additional material-precipitate interface created by a dislocation when it shears through a coherent particle;

2) stacking-fault strengthening, which occurs when the stacking-fault energies of the precipitate and matrix phase are different;

3) modulus hardening, which occurs when the shear moduli of the matrix and precipitate phase are different;

4) coherency strengthening, which arises by the elastic strain within the matrix lattice and a coherent precipitate.

5) order strengthening, which operates when the crystal structure of a coherent precipitate is a superlattice and the material is a disordered solid-solution.

Two or more of these mechanisms can be operative simultaneously. Nevertheless, in IN-738 coherency strengthening and order strengthening appear to be the dominant mechanisms.

In a large number of age hardening alloys, precipitation occurs by non-homogeneous nucleation, followed by particle growth and coarsening. The precipitation of γ' precipitates occurs by homogeneous nucleation and the growth stages normally

transpire very rapidly, i.e., the strength increases with aging time, during the coarsening stage, during which the volume fraction of precipitate remains essentially constant. The precipitate particles with the following characteristics generally provide a good level of strengthening[10] :

a) Volume fraction of at least 30%,

b) Interparticle spacing of the order of 500 Å ,

c) A strength greater than that of the matrix to minimize dislocation cutting through,

d) Relatively small lattice mismatch (within 1%) with matrix to promote stability,

e) Sufficient ductility to prevent formation of easy fracture path.

The different phases present in a cast IN-738 alloy are listed in Table 3.

TABLE 3: Microstructure of cast IN-738 (LC) superalloy

Major Phase	Minor Phase (Carbides)
Gamma Prime (γ') → $Ni_3(Al, Ti)$ based	MC → Tantalum based $M_{23}C_6$ →Chromium based

2.3.2.1 Gamma Prime (γ')

When the solubility of Ti and Al is exceeded, a precipitate is formed which is based on the Ni_3Al phase in the binary Ni-Al system. Ti can substitute extensively in this phase which is generally referred to as $Ni_3(Al, Ti)$ or γ' which is an ordered, $L1_2$ based phase. It has been suggested [12] that the composition of γ' in IN-738 is,

$$(Ni_{.922}Co_{.058}Cr_{.017}Mo_{.002}W_{.002})_3(Al_{.518}Ti_{.352}Ta_{.046}Nb_{.41}W_{.014}Cr_{.027}) \text{------(1)}$$

This intermetallic γ' phase has an ordered face centred cubic crystal structure with a lattice mismatch of about 1% with the gamma(γ) matrix(Ni-Cr-Co based austenite). This close match in the lattice parameters results in a complete accommodation of the small lattice misfit by elastic coherency strains and low surface energy. Also, the similarity in the crystal structure of the precipitate and matrix causes a quick aging response and the growth of the precipitates occurs largely by the growth of large particles at the expense of small ones (Ostwald ripening), thus rendering the precipitate very stable at elevated temperatures.

A pseudo-ternary phase diagram, constructed on the results of the constitutional studies, which illustrates the phase-relationships in the simple Ni-Cr-Al-Ti system, is shown in Figure 1[13]. Depending on the casting conditions large amount of segregation can result in γ-γ' eutectic islands with a coarser γ' structure. The γ-γ' eutectic islands consist of lamellar structure as fine and continuous γ' platelets, or rafts. They promote inhomogeneous deformation as in that region the deformation mechanism comprises of dislocation climb rather than dislocations shearing the precipitate [14].

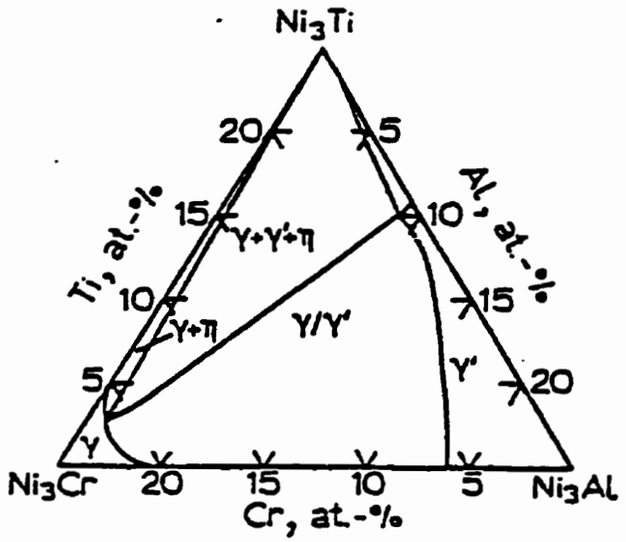

Figure 1. Pseudo Ternary Phase Diagram for Ni-Cr-Ti-Al Alloys.

2.3.2.2 Carbides (MC AND $M_{23}C_6$)

The majority of carbides in the as-cast structure are of MC type with a size ranging from one micron to a hundred microns and has an irregular morphology. This 'Ta' based carbide is generally very stable and is formed during the melting practice. The TaC precipitates are usually difficult to dissolve in the solid γ phase, however, their size and volume fraction distribution along the grain boundaries can be controlled which can restrict the grain growth of the alloy during the solution treatment stage. It has been suggested that these carbides have the following formula [12]:

$$(Ti_{.5},\ Ta_{.2},\ Nb_{.2},\ W_{.04},\ Mo_{.03},\ Cr_{.02})\,C$$

Any free carbon not used in the formation of MC, when the cast ingot cools through the $M_{23}C_6$ solvus range (1,000°C - 1,050°C) will precipitate out as fine $M_{23}C_6$ carbides. Generally their volume fraction is very low but a noticeable amount can form

during subsequent heat treatment, which is usually aging.

2.4 Effect of Alloying Elements on the Microstructure

Table 4 briefly lists the role of various alloying elements present in IN-738.

TABLE 4 : Functions of various Alloying Elements in cast IN 738

ELEMENT	EFFECT
Nickel (Ni)	Phase(s) Stability
Chromium (Cr)	Oxidation and hot corrosion resistance, Carbide former ($M_{23}C_6$)
Molybdenum (Mo)	Solid Solution Strengthener, Carbide Former (MC)
Tungsten (W)	Solid Solution Strengthener, Carbide Former (MC)
Aluminum (Al) + Titanium (Ti)	Formation of γ' ($Ni_3(AlTi)$) hardening precipitate, Ti forms MC type carbide as well
Cobalt (Co)	Raises solvus temperature of γ' and the melting point of nickel rich matrix
Carbon (C)	Formation of various carbides such as MC and $M_{23}C_6$
Niobium (Nb)	MC carbide former
Tantalum (Ta)	Solid Solution Strengthener, Principal element in MC carbide
Impurity Elements. Sulphur (S), Phosphorus (P), and Silicon (Si)	Causes embrittlement by grain boundary segregation

Some other observations that have been made are as follows:

(a) 'W' is more effective than 'Mo' in increasing the resistance to deformation. Thus the newer trend is for a higher concentration of 'W' and a reduction in 'Mo' concentration for increased solid-solution hardening and greater resistance to the ripening of the precipitate particles of γ'.

(b) The trend in the more recent version of the alloy is for somewhat lower amounts of 'Al' but increased concentration of 'Ti', 'Nb' and 'Ta' to produce slightly lower volume fraction of γ' with increased anti-phase boundary, and greater mismatch between precipitate and the matrix.

2.5 Commercial/Standard Heat Treatment

Alloy IN-738 achieves the best combination of mechanical properties after the following heat-treatment:

a) Partial solution heat treat for 2 hours at 1,120°C ± 10°C in vacuum/Ar followed by cooling to room-temperature at the rate equivalent to air cooling.

b) Age for 24 hours at 845°C ± 5°C in Argon/Vacuum followed by air-cooling to room-temperature.

This commercial heat-treatment produces a bimodal distribution of γ' precipitate particles in spherical and cuboidal shapes with approximately 0.45 μm mean edge length for the cuboids and approximately 0.1 μm mean diameter for the secondary spheroidal γ' particles.

2.6 Microstructural Stability of IN 738

The fact that the aging heat-treatments are performed in the same temperature range as the operating temperature of this material, results in a metastable microstructure. The prominent microstructural damage includes γ' coarsening and agglomeration, disintegration of MC carbides ,both along the grain boundary and in the matrix , excessive generation of brittle grain boundary $M_{23}C_6$ carbides, the straightening of serrated grain boundaries and formation of a γ' network along them. Secondly, the standard solution heat-treatment temperature of 1,120°C does not completely homogenize the microstructure, i.e., it takes only 50% of the primary γ' into solution (the volume fraction of γ' in cast IN738 is 40%) and leaves behind most of the eutectic γ' islands. The inhomogeneous microstructure provides for deformation of the matrix when stressed during a deformation process. Therefore, there is still some scope for modifying the heat-treatments for IN-738 in order to produce a more controlled and stable microstructure.

The particle size distribution and the morphology of γ' precipitates play an important role in determining the microstructural stability, including resistance to particle coarsening. From the view point of kinetics, microstructural coarsening can be modified and even impeded by the elastic interaction between misfitting precipitates. During coarsening, changes in the elastic interaction energy between precipitates owing to changes in particle size can be of the same magnitude as the corresponding changes in the interfacial energy. If certain spatial distributions of the precipitates give rise to a negative

interaction energy, then the elastic interaction energy can dominate the interfacial energy and a distribution of similarly sized particles that are resistant to coarsening could give a minimum in the free energy. In addition, the misfit strains can induce changes in precipitate morphology and lead to strong spatial correlation's between precipitates in those crystallographic directions for which the particles have a negative interaction energy. Thus by controlling misfit, it may be possible to stabilize a two phase microstructure against coarsening [3].

2.7 Heat Treatments and Their Effects on Cast IN 738

The response of the γ' precipitate morphology to heat-treatment varies considerably between the interdendritic regions and the dendritic regions. The extent of these regions for a given heat treatment is dependent on the size of the casting and casting conditions. A faster cooling rate in thin castings prevents the formation of secondary γ' particles. During heat-treatment the difference in response results from the much finer grain-size, and consequently the dendrite spacing in the thin castings. The finer dendrite size means that the amount of segregation is reduced so that the ease of solutionizing the γ' in the inter-dendritic regions also gets reduced. Therefore, a higher solution-treatment temperature would be required to achieve an equal degree of homogenization for the same heat treatment time [15].

2.7.1 Standard Heat Treatment Condition

On solution-treating cast IN-738 for two hours at 1,120°C followed by a fast air-cool, only the γ' in the dendritic core regions is taken into solution. The size of these

regions is dependent upon the size of casting and the resultant grain size. These regions occur owing to the effects of segregation during solidification on the concentration of 'Al' and 'Ti' in the various parts of each grain. In the dendritic core regions the concentration of 'Al' and 'Ti' is below their solubility product in the gamma (γ) matrix at the solution-treatment temperature, thus allowing the solutionizing of γ' precipitates. The dendritic core regions are outlined by a ring of very large γ' particles (Figure 2) due to very rapid particle growth immediately before solutionizing[15].

This rapid growth results from the local 'Al' & 'Ti' concentrations being higher than in the dendritic core regions. Therefore, an increase in the solution-treatment temperature is required.

Fine secondary precipitates form uniformly throughout the sample during cooling from the solution-treatment temperature. Further, fine tertiary precipitates form in rings around the primary γ' precipitates. These rings of tertiary precipitates form at the same time as the secondary precipitates but are restricted in size owing to the low concentration of 'Al' and 'Ti' in the matrix in the immediate vicinity of primary γ' particles. During the aging treatment (24/16 hours at 845°C) the rings of tertiary precipitates coalesce onto the primary particles and the fine secondary particles increase in size. Thus, the fully heat-treated alloy has two distinct regions as shown in Figure 3; the interdendritic regions contain two size distribution of γ' particles and the dendritic core regions contain only a single size distribution of γ' particles [15].

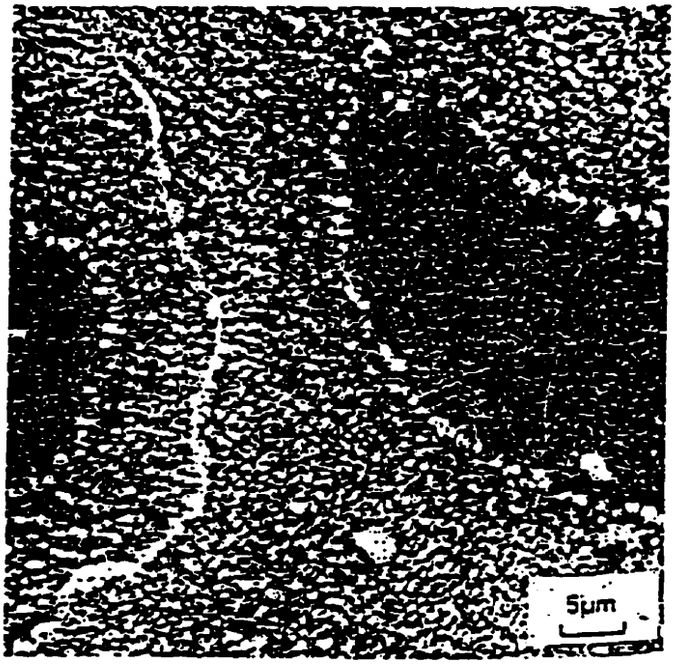

Figure 2. Extent of Primary γ'-Free Zones (dendritic cores) After Standard Heat-Treatment.

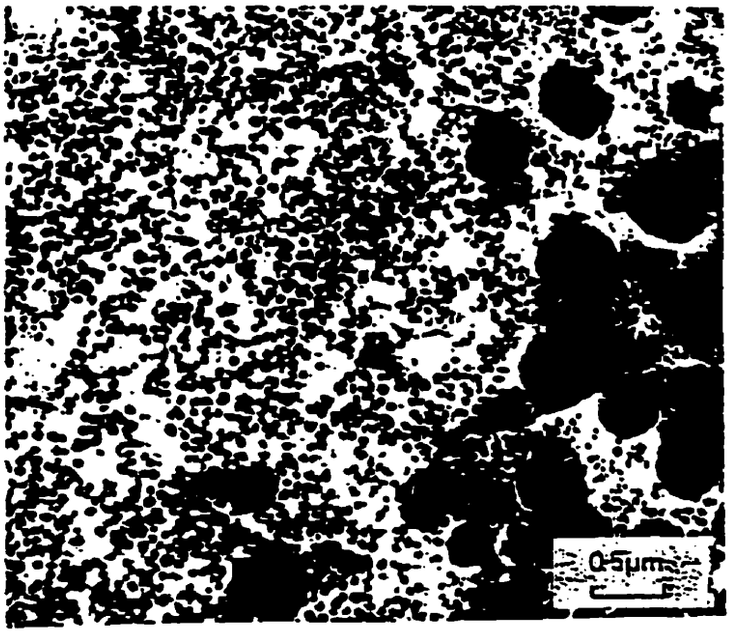

Figure 3. γ' Precipitate Morphology and Distribution in a Fully Heat-Treated Alloy.

2.7.2 Solution-Treated Condition

In most precipitation hardened superalloys, and especially IN-738, it is almost impossible to suppress γ' precipitation upon cooling after solution heat-treatment (even by rapid quenching) because of the high degree of supersaturation of solutes, coupled with the inherently rapid rate of formation of γ' precipitates. Therefore, instead of being soft and ductile, the solution-treated microstructure consists of relatively high strength grain matrix containing a large volume-fraction of γ' particles in combination with relatively weak, precipitate-free grain boundaries [16].

Another suggestion is that the solution-treated material has considerably less tensile ductility than the fully heat-treated material at temperatures up to the γ-γ' solvus. The low-ductility at elevated temperatures is apparently caused by the absence of large grain-boundary particles needed to inhibit grain-boundary sliding. The γ'-strengthened grains resist deformation, while the precipitate-free grain-boundaries (as the secondary γ' particles and fine $M_{23}C_6$ carbides along them dissolve) can slide relatively easily resulting in stress-concentrations and inter-granular crack initiation at low macroscopic plastic strains. In the fully heat-treated alloy, the large inter-granular γ' particles are effective obstacles to grain boundary sliding. Therefore, deformation is more uniformly distributed throughout the grains and the resulting high-temperature ductility of the material is greater [16].

2.7.3 Solution-Treated and Aged Condition

The standard aging temperature for IN 738 is 845°C but it is also possible to age it at temperatures around the $M_{23}C_6$ solvus, i.e., 950°C - 1,025°C. The variation in room temperature vickers hardness, Hv_{30}, with isochronal (16 hrs) aging temperature is shown in Figure 4a.

It is seen that after aging at 773K, the hardness is the same as that of the solution treated material. However, as the aging temperature increases, the hardness rises to a maximum (Hv ≈ 485) at 1,100K (827°C). At higher aging temperatures the hardness first decreases and then reaches another maximum value of Hv ≈ 440 at 1,467K (1,194°C). The second increase in hardness is attributed to an increase in strength due to the dissolution of coarse degenerate γ' cuboids which brings about a redistribution of solid solution hardening elements[27].

Figure 4b shows the weight fraction of electrolytically extracted γ', after correction for the carbide contents, as a function of isochronal aging temperature. A maximum fraction of ~ 0.45 results from aging at 1,100K, which coincides with the maximum hardness. The primary γ' cuboid size remains fairly constant at 450 nm in the material aged in this temperature range of 1,000 - 1,300°K. The combined volume fraction of carbides remained constant over the entire aging temperature range [27].

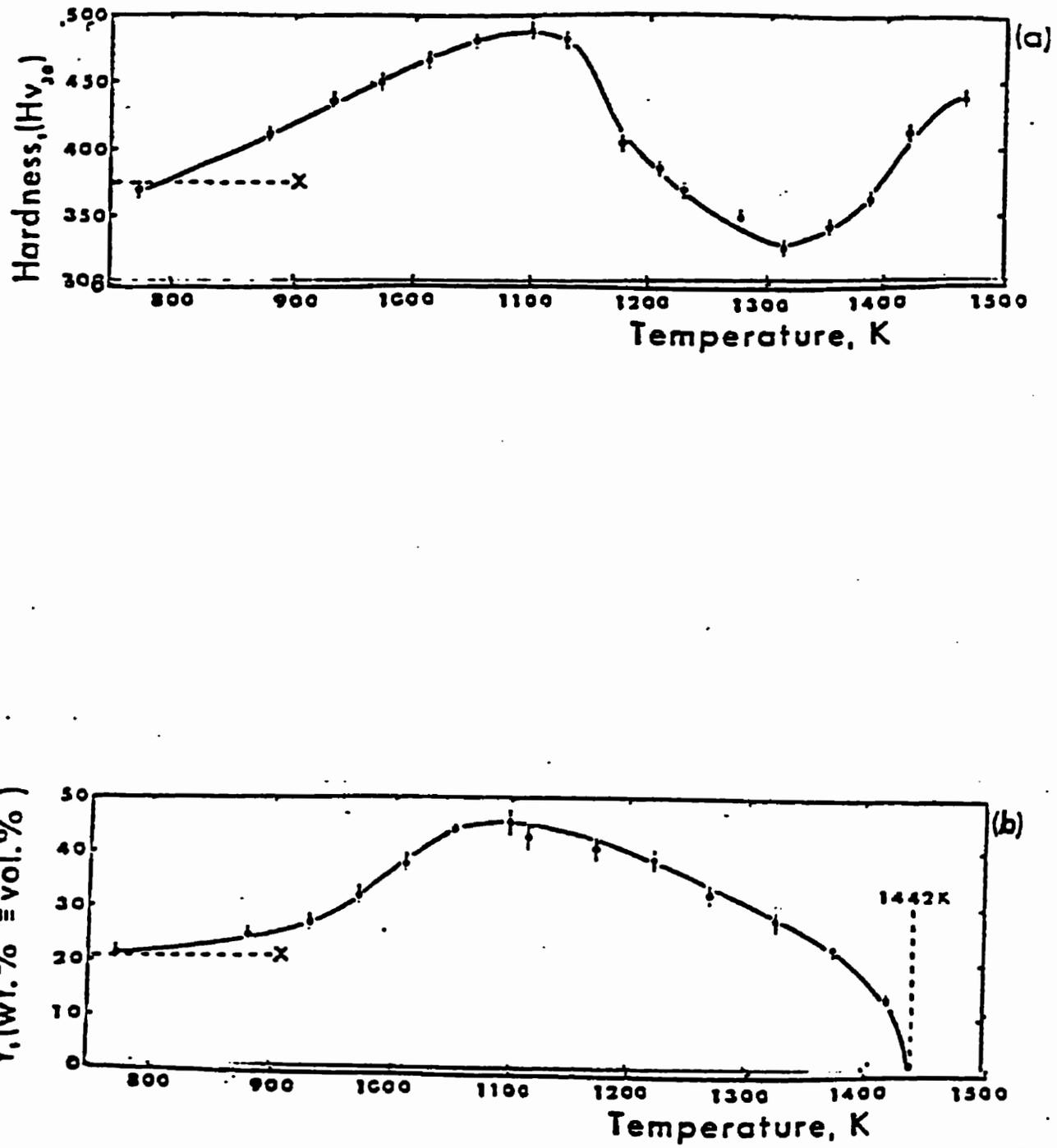

Figure 4. Variation with Isochronal (16 h) Aging Temperature of (a) Hardness (b) total γ' Precipitate Fraction.

The basic microstructure of aged IN-738 comprises γ' precipitates, MC and other carbides distributed within the grains and along the grain boundaries, grain-boundary serrations, precipitate free zones and dislocation substructures. Aging affects various phases and grain structure in the following manner :

2.7.3.1 Gamma Prime (γ') Precipitates

In his review on precipitation hardening, Ardell [9] concluded that for nickel base alloys the γ' precipitation occurs by homogeneous nucleation followed by particle growth and coarsening. The nucleation and growth stage transpires very rapidly in the heavily supersaturated (γ' forming elements) alloys, so that aging occurs very rapidly, i.e., the strength increases with aging time. During the coarsening stage, the volume fraction of precipitates remains constant. Footner and Richards[17] found that the variation of γ' size with exposure time was complex owing to the initial partial solution-treatment and the following aging which resulted in the presence of two distinct γ' populations. In other words, a 'bimodal distribution' of cuboidal and spheroidal γ' particles occurred. On aging, the mean size of the larger population (primary particles) was observed to remain sensibly constant at a value of about 350 nm, whilst that of the smaller size population (secondary particles) increased, the rate of increase dependent on the aging temperature. The subsequent growth of the primary particles occurred only when the overall size distribution appeared to be unimodal and this growth rate again obeyed a 'd-$t^{1/3}$' law. The maximum size attained by the secondary γ' particles was about 140-160 nm and further aging resulted in their rapid coalescence and disappearance. The

initial partial solution-treatment resulted in cuboidal particles which is a consequence of the high degree of mismatch between the matrix and γ' phase, but once the growth of the primary particles has been initiated they transformed to roughly spherical or even 'shapeless' particles[17].

The driving force for the growth of primary particles is the reduction in total mismatch strain, and this process did not become operative until the secondary solute γ' particles had attained a size and a surface concentration comparable with those of the primary particles. Subsequently, the single population of (primary) particles experienced normal growth kinetics. As the growth proceeded, aging changed the matrix composition (e.g., the concentration of Al and Cr, etc.) and hence decreased the mismatch and promoted spherodization[17].

According to Ardell[9], the alignment of γ' particles along the elastically soft [100] directions of the matrix phase gets more pronounced with increasing aging time. The particle alignment is due to the minimization of elastic interaction energy between precipitates. Although the elastic interaction energy between two precipitates generally depend on anisotropy, the difference in elastic constant between phases and both the sign and magnitude of misfit strain, the leading term in the interaction energy is proportional to the square of misfit strain. With aging the misfit is reduced due to compositional adjustments and therefore the elastic energy term is also decreased resulting in enhanced alignment.

2.7.3.2 MC and $M_{23}C_6$ Carbides

In cast IN-738 the primary MC carbides are aligned along the growing dendrites

during solidification as shown in Figure 5.

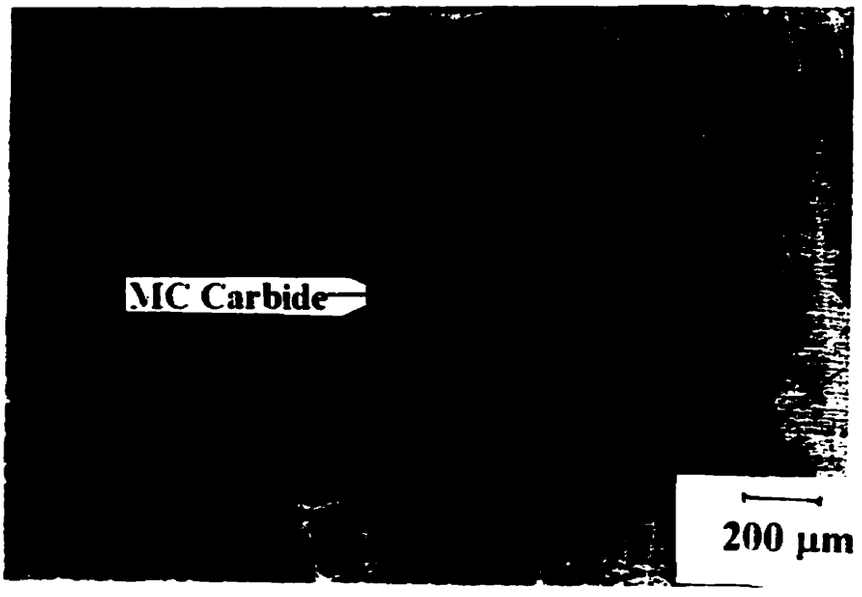

Figure 5. Optical Micrograph showing the alignment of MC carbides along the growing dendritic direction ,50X.

Because of their relative coarseness, they generally do not contribute to the strength of the matrix in the dispersed state.The size of MC carbides is important and a reduced volume and size results in a reduction in the number of pre-cracked carbides which are potential sites for crack initiation. Although there is little documentation, it is frequently assumed that non-carbide forming elements do influence the formation of carbides. Cobalt for example, has been suggested to modify the MC carbide morphology [18]. Although the solvus of MC is well above 1,200°C, the MC particles consistently degenerate at the aging temperatures via the following reactions [19]:

$$\gamma(\text{matrix}) \rightarrow \text{carbides} + \gamma^{*} \text{----------(2)}$$

$$\gamma^{*}(\text{Ni, Cr, Al, Ti}) + \text{MC (Ta, Ti, Nb C)} \rightarrow \gamma'(\text{Ni}_3(\text{Al, Ti})) + \text{M}_{23}\text{C}_6((\text{CrMo})_{23}\text{C}_6) \text{ -----(3)}$$

In accordance with equation (2) it is expected that the nucleation and growth of copious amounts of grain-boundary $M_{23}C_6$ carbides would deplete the adjacent regions of 'Cr' and 'Mo' ($\gamma \rightarrow \gamma^*$), which in turn would relieve solute supersaturation and thus causing the dissolution of primary γ' in this region. Despite the denudation of material around boundaries of primary γ' precipitates, the grain-boundary γ' precipitates remain undissolved in these microstructures as shown in Figure 6. It is suggested that the solvus temperature of primary γ', secondary γ' and the grain-boundary γ' precipitates can be considerably different since the chemical composition and consequently their solubility rates differ markedly [25].

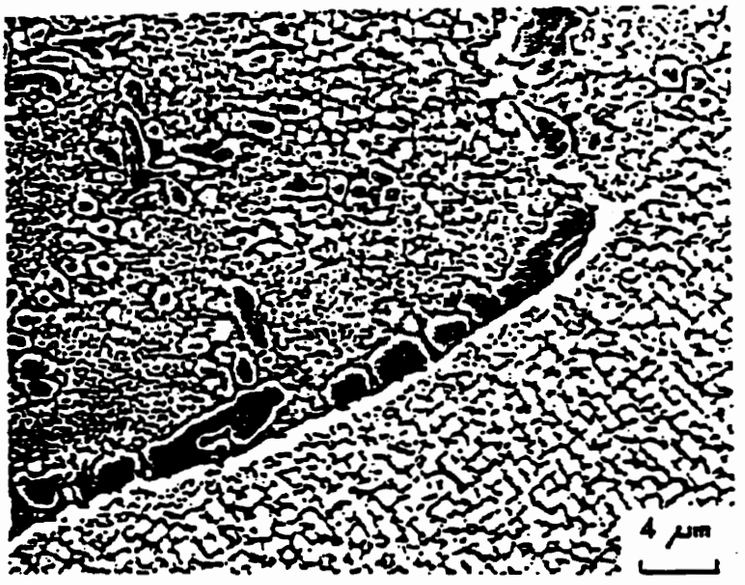

Figure 6. Primary γ' Denudation Adjacent to the Grain Boundaries.

With decreasing MC carbide particle size there is an increased tendency for film like rather than globular $M_{23}C_6$ carbide to form at the grain boundaries, which is related to kinetics. With small and finely dispersed MC particles, the surface area per unit volume is larger and the diffusional distance for carbon to move to the surface of a grain is smaller than for a material containing coarse and widely dispersed MC carbides. Both these factors tend to accelerate the transformation of MC to $M_{23}C_6$ in the material containing finely dispersed MC. Thus, the carbon content in IN-738 is an important parameter in determining the amount of these carbides [20].

$M_{23}C_6$ carbide has a solvus in the range of 1,000°C - 1,050°C. During the solution-treatment of the alloy, $M_{23}C_6$ particles if any, are dissolved. They reprecipitate during heat-treatment or exposure at lower aging temperatures. Aging induced degeneration of primary MC carbides provides a reservoir of free carbon for added precipitation of grain boundary $M_{23}C_6$ and this eventually (with over-aging) leads to the formation of a continuous film of carbide along the grain-boundary. Otherwise if there is a high supersaturation of carbon then there is a tendency for cellular grain-boundary $M_{23}C_6$ to form, which is continuous in nature. At higher temperatures of aging, 950°C - 1,025°C, $M_{23}C_6$ tends to form as globules along the grain-boundaries [21].

Grain-boundary $M_{23}C_6$ carbides are known to have either a beneficial or detrimental effect on mechanical properties such as creep and these effects are largely governed by their morphology, size and distribution. The presence of a heavy and/or continuous network of grain-boundary $M_{23}C_6$ carbide particles can facilitate grain-boundary sliding and crack-propagation by boundary-matrix decohesion. Discrete grain-

boundary $M_{23}C_6$ particles on the other hand are known to improve creep life and ductility by hindering the nucleation and growth of cavities by deactivating the nucleation-sites and increasing the intercavity distance and also by suppressing the grain-boundary-sliding by reducing the diffusion rates along grain-boundaries. Thus grain-boundary $M_{23}C_6$ interparticle spacing plays a very crucial role in determining the optimum mechanical properties of the material [22].

Another important aspect to be noted is that the continuous carbide film along the grain-boundaries provides a serious constraint while attempting to rejuvenate the degraded microstructure. This is because the degenerated primary MC carbide cannot be reprecipitated in the original morphology. Any attempt to reprecipitate the free carbon as MC carbides will lead to a fine MC carbide dispersion within the matrix and these fine carbides will subsequently degenerate to form $M_{23}C_6$ carbides at a much faster rate than the original primary MC carbides present in the unexposed material [23].

A high resolution transmission electron microscopy has revealed $M_{23}C_6$ carbides along grain boundaries to be discontinuous, irregular shaped precipitates[24]. Lattice imaging revealed that each carbide particle was actually composed of several subgrains, formed by separate nucleation of carbides on the same matrix grain and subsequently impinging together to form a particle [24].

2.7.3.3 Grain Boundaries and Serrations

Cast IN-738 in general has a coarse grain size. The grain boundaries indirectly control the extent of $M_{23}C_6$ precipitation along it. The larger the grain size, the smaller is

the grain-boundary area available for the formation of precipitates. A given volume of precipitate of a phase like $M_{23}C_6$ will therefore form a thicker and more continuous film as grain size increases. This film can be deleterious to fatigue, ductility and impact properties. On the other hand if grain size is too fine, the density of $M_{23}C_6$ becomes so small that a loss in rupture life occurs [10].

Serrated grain-boundaries are known to provide a more favourable balance of intragranular strength and grain-boundary strength. The grain-boundary serrations are said to impede the grain-boundary sliding and thus promote intragranular deformation. One direct impact of this is for the welding process to include a suitable pre-weld heat-treatment that produces serrated grain-boundaries in base-metal. Therefore the cracks that initiate in the heat-affected-zone will be inhibited from propagating into the base metal. Cast IN-738 is perhaps the most extensively studied superalloy in terms of serrated grain-boundary formation. In this alloy, serration amplitude and wave length increase with decreasing cooling rate until an optimum cooling rate is reached [26], as shown in Figure7.

Grain-boundary serrations can be produced either through slow cooling from the solution-treatment temperature or during the aging heat-treatment. In the former case it is essential to have a γ' solvus temperature higher than that of $M_{23}C_6$ solvus which is true for IN-738 [26]. During the aging treatment, coarse serrations can also develop due to cellular precipitation of grain-boundary $M_{23}C_6$ and the coarsened grain-boundary γ' precipitates. Figure 8 shows the two mechanisms for cellular precipitation of $M_{23}C_6$ carbides.

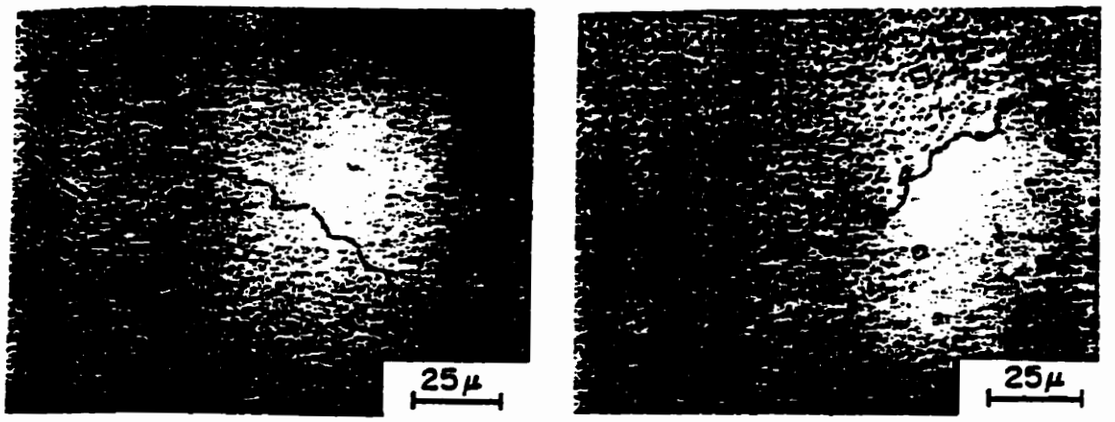

Figure 7. Optical Micrographs Showing Serrated Grain Boundary Formation in IN-738 (a) Cooling Rate of 2-33°C/Minute (b) Cooling rate of 0.5°C/Minute [7].

Figure 8 (continued)

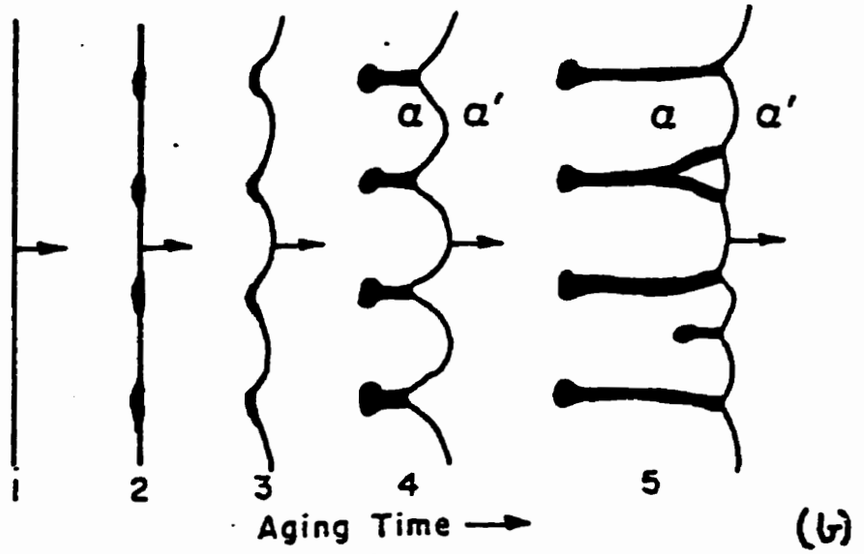

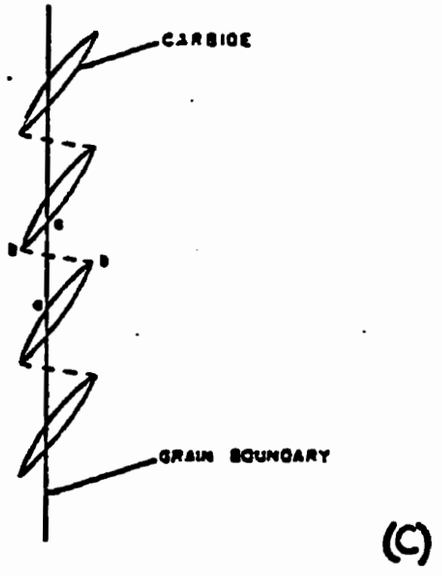

Figure 8: (a) Tu-Turnbull Mechanism of Serrated Grain Boundary Formation Involving Cellular Precipitation, (b) Fournelle-Clark Mechanism for Serrated Grain Boundary Formation by Cellular Precipitation, (c) A General Model for Serrated Grain-Boundary Formation by Cellular Precipitation in Steels where

$M_{23}C_6$ Particles are Assumed to Grow from one Grain into the Matrix of Adjacent Grain [26].

Serrations are basically specific boundary conditions, with regard to grain-boundary γ' particle size 'r_{gb}', its interfacial energy 'γ_{st}', the particle matrix misfit 'δ', and the matrix shear modulus 'μ' for maintaining stability of these serrations. These boundary conditions are related by the expression of the form,

$$r_{gb} = 3\gamma_{st} / 3\mu\delta^2 \text{ ----------(4)}$$

A slow cooling (2-40°C/minute) from the solution-treatment temperature can produce grain boundary γ' particles ($r > r_{gb}$) and will result in serrated grain-boundaries due to cooling. The development of serrations with aging at lower temperatures can be attributed to grain-boundary γ' coarsening, and for a critical grain boundary γ' size, that exceeds theoretical r_{gb} (equation 4), the grain boundary γ' particles can pin the migrating grain-boundary resulting in the development of well rounded peaks and valleys with a large wavelength[26].

A contrasting theory from Koul and Castillo[25] suggests that it is not possible for a grain boundary to migrate between the primary γ' particles considering the time and temperature dependence of the grain size. The grain size is established by the solution treatment temperature, but it is possible for the boundaries to migrate at a lower temperature when sufficient time is available, i.e. of the order of few hours. Koul and Castillo[25] found that for alloy IN 738, the time spent at a given temperature is far too

short to influence the boundary migration in this material. They suggested that γ' nucleates on one side of the grain boundary on cooling through the γ' precipitation temperature range. Due to the presence of a grain boundary with certain width adjacent to the γ' precipitate, the coherency strains on the boundary side of γ' are easily accommodated. A net strain energy differential between the interface provides a driving force to move the γ' particle in the direction of the boundary. The γ' particle movement will however, be opposed and finally stopped by the line tension of the boundary, thus creating serrations in the grain boundary.

These serrations can, however, disappear with prolonged aging or during long service exposure. With over-aging there is a competitive increase in 'γ_{st}' and a decrease in 'δ'. This is due to a partial loss of the coherency of grain-boundary γ' precipitates which would naturally be accompanied by a decrease in 'δ' in the γ'-matrix interfacial plane on the matrix side of the grain-boundary γ' precipitates. So altogether 'r_{gb}', the minimum grain-boundary γ' particle size required to support grain-boundary serrations, will also increase with aging. Therefore with prolonged exposure serrations become metastable as r_{gb} exceeds the size of existing grain-boundary γ' particles and the grain-boundary line tension is expected to straighten the serrated grain-boundaries [25].

2.7.3.4 Precipitate Free Zones (PFZ)

The complex and high γ' volume fraction alloy like IN-738 does not show significant PFZ effects, probably because of its higher saturation with regard to γ'

forming elements [18]. The possibility arises due to the precipitation of Chromium rich $M_{23}C_6$ carbides along the grain-boundaries. This results in a reduction of the amount of 'Cr' in the matrix along the boundaries. As a result, the solubility of 'Al' and 'Ti' increases so that the secondary γ' does not precipitate out in this region and a zone is formed next to the grain boundary containing only coarse primary grain-boundary γ' [33]. Consequently, aging at $M_{23}C_6$ solvus temperature will reduce the extent of this PFZ.

2.7.3.5 Precipitation Within γ' Particles

The presence of fine precipitates within coarse γ' particles has been observed by Merrick [19, 34] in cast IN-738 with aging, as shown in Figure 9. According to him the fine precipitates are clustered near the central region of the coarse γ' particles resulting in a precipitate free zone (PFZ) at the periphery. This observation explained why not all of the coarse primary γ' particles exhibit fine precipitation within them, since some of them will have been sectioned through the PFZ. No evidence of this fine precipitation was found within the small γ' particles. Furthermore, he also found that these fine particles were not a carbide of the MC or $M_{23}C_6$ type, and noted that γ' and $M_{23}C_6$ show the same relationship to the shadowing media but opposite to the fine precipitate within the coarse γ' in an carbon extraction replica. The dark field TEM studies also revealed the presence of particles as dark spots, but were not identified.

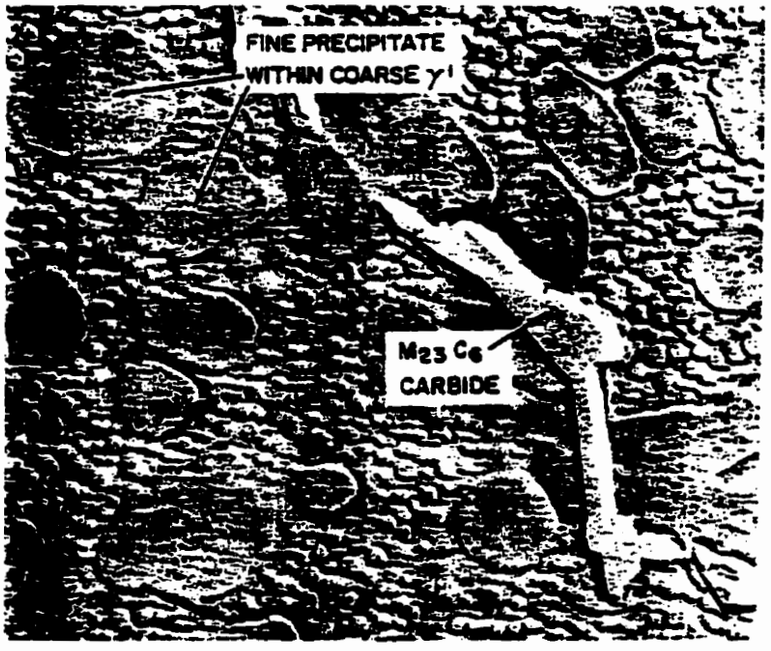

Figure 9: Structure of Fully Heat-Treated IN-738 Showing the Presence of Fine Precipitation with in Coarse γ', 14,000 X.

A likely explanation for the presence of these fine particles was given to be that these fine precipitates are simply the γ phase[34].

2.7.4 Extremely Long Aging at 845°C

After approximately 30,000 hours or more of aging, the microstructure of the alloy comprised of 100% degenerate cuboids where the dissolution of the spheroidal γ' was virtually complete as shown in Figure 10.

In other areas of the same material, the original serrated boundaries had completely disappeared as shown in Figure 6 and on one side of these straight grain boundaries extremely large γ' precipitates, approximately 3,000-4,000 nm in size, had also formed. On either sides of these straight grain-boundaries a much reduced density of primary cuboidal γ' within the matrix was also noted. The volume fraction of MC carbides had

dropped significantly. A degenerated primary MC had a lot of debris surrounding it which was extremely rich in Chromium. The majority of the grain boundaries contained copious amounts of $M_{23}C_6$ precipitates [22].

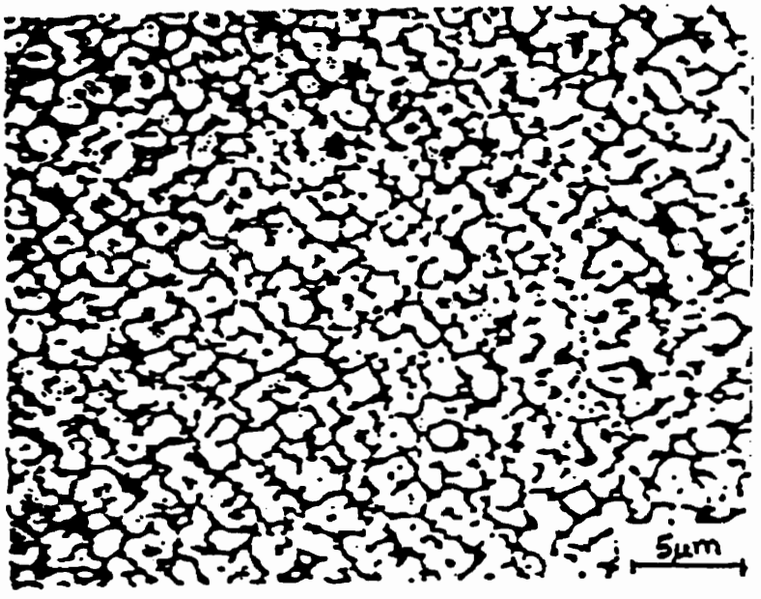

Figure 10: SEM Micrograph Showing the Microstructure of Service Exposed IN-738 for 30000 hrs.

2.8 Analysis of Precipitation Reactions in Heat-Treated Cast IN-738

The mechanical properties of IN-738 strengthened by γ' precipitates primarily depends on the following factors:

a) volume-fraction of γ',

b) the precipitate-particle spacing, shape, size, and distribution,

c) the coherency strains due to lattice misfit between γ and γ' phase,

d) the $M_{23}C_6$ carbides at grain-boundaries,

e) formation and disappearance of the grain boundary serrations,

f) grain-size.

Grain size usually doesn't contribute significantly to the overall strength since it is generally too large (in mm's). The beneficial and deleterious effect of grain-boundary carbides and serrations have been discussed earlier, in this review section.

2.8.1 γ' Volume Fraction Features and Estimation

For phase characterization in high temperature 'Ni' base superalloys, electrochemical extraction of the precipitate by anodic dissolution has been successfully used to determine the composition, structure, lattice constants and volume fraction of γ' and various carbides. Techniques were developed by Kriege and Sullivan[35] for the extraction and analysis of γ' from Udimet 700. The extraction of carbides is relatively simpler because carbides are chemically dissimilar from γ and γ'. The traditional approach for the extraction of γ' precipitates has been to use an electrolyte consisting of phosphoric acid in water, methanol or ethanol. However, in this technique, a significant portion of the γ' is dissolved by the electrolyte. When separating γ' by anodic dissolution it is desirable to work in a region of high current density so that a reasonably large amount of sample can be collected for analysis in a comparatively short period of time. In the study by Kriege and Sullivan[35], a high current density near the potential of

oxygen evolution was used. 1% solution of citric acid and 1% ammonium sulfate in water was found to be the best electrolyte under these experimental conditions. Carbides always accompany the extracted γ', therefore in order to make a correction for their presence a separate anodic dissolution using a 10% HCl-Methanol electrolyte was carried out. The second dissolution preferentially removed carbides only [35].

The above experiment is usually conducted to precisely evaluate the volume-fraction of γ' in Nickel base superalloys. The numerical value is then used to evaluate the mean γ' particle spacing and subsequently the strengthening due to its presence.

2.8.2 Lattice Mismatch

If a_γ and $a_{\gamma'}$ are the unconstrained lattice constants of the respective phases, and $a_{\gamma'}$ can be measured by using powders of γ'-phase extracted electrolytically, then unconstrained lattice misfit parameter δ is defined as[14]:

$$\delta = (a_\gamma - a_{\gamma'}) / a_\gamma$$

----------(6a,b)

$$or \quad \delta = \frac{a_{\gamma'} - a_\gamma}{[(a_{\gamma'} + a_\gamma)/2]}$$

Nembach and Neite[42] in their review on precipitation hardening of superalloys described γ'-precipitates as fine coherent particles embedded in a γ-matrix that are normally constrained. These particles are forced to adjust their lattice constants somewhat to that of the matrix. The relative difference in lattice constant of such constrained particles is

called the constrained lattice misfit ε, or the coherency strain. Motto and Nabarro, in a review[36], related ε to δ, the bulk modulus κ of the precipitate and the shear modulus G_R of the matrix by the following expression:

$$\varepsilon = \delta / \{(1 + 4\ G_R) / (3\kappa)\} \text{ ----------(7)}$$

A good approximation for ε is 2/3 δ[36]. Coherency strains or mismatch between crystal lattices of the austenite matrix (γ) and the γ' precipitates have been consistently used to explain the hardening of γ' strengthened superalloys. At higher working temperatures (≥ 0.6 Tm), low coherency strain would be desirable to minimize γ-γ' surface energy and, thus, to maximize phase stability. Therefore IN-738 is designed with elements like Mo and Cr to raise the lattice constant of γ and thus reducing the misfit. Space morphology of the γ' particles depends on the value of misfit δ and their radius r. In case of cuboidal precipitates, r is half the cube length. As δ and/or r increases, the morphology changes from spheres to cuboids, to cuboidal arrays, and finally to dendrites [36].

2.8.3 Ostwald Ripening of γ' Particles

Principally one can distinguish three stages in a continuous precipitation process:

1) nucleation,

2) growth of the nuclei until the matrix reaches its equilibrium concentration of solute,

3) Ostwald ripening.

In practice generally, at least two processes occur concurrently: 1 and 2, or 2 and 3.

In stage 3, the surface energy of the precipitates is reduced by coarsening: small ones dissolve and large ones grow at the expense of the former.

In the early stages, deformation of the alloy occurs by shearing of the fine precipitates and the τ_p (respective contributions of secondary γ' particles to the total shear stress) increases with time. After long annealing treatments, when the precipitate particles are large, the particles are bypassed by dislocations during deformation and τ_p decreases with further annealing. These two aged conditions are formally known as underaged and overaged conditions. The optimum state yielding the maximum value for τ_p, is called the peak aged condition and material usually deforms by a combination of shearing and bypassing mechanisms.

2.8.3.1 LSW Theory of Ostwald Ripening

The most widely recognized theory that deals with Ostwald ripening is the one developed independently by Lifshitz and Slyozov, and Wagner, or the LSW theory. However, the original LSW theory dealt with the case where precipitate particles were assumed to be spherical, dispersed with separations much larger than the average particle diameter in a liquid matrix with a constant equilibrium concentration. The particles were thus essentially assumed to have very small volume fraction in the matrix. In this situation, the mean particle radius was shown to vary with time as follows:

$$\bar{r}^3 - \bar{r}_0^3 = kt \qquad (8)$$

where $\bar{r}_o$ is the mean particle radius at the onset of coarsening

and k is a constant given by:

$$k = \frac{8DC_e\gamma V}{g\kappa T} \text{ ---------- -(9)}$$

where D is the composite diffusion constant,

Ce is the solute equilibrium concentration,

γ is the particle/matrix interfacial energy,

V is the atomic volume of the precipitate,

κ is the numerical constant depending on particle distribution and

T is the temperature and g is the acceleration due to gravity [37].

2.8.3.2 MLSW Theory of Ostwald Ripening

A very important assumption in the LSW theory of lattice diffusion controlled particle coarsening is that the volume fraction (V_F) of γ' precipitates is very small, i.e., the interparticle spacing is very large compared to the particle size. This implies that there is no interaction between neighbouring particles during the coarsening process. However, in most Ni base superalloys and especially in IN-738, the volume fraction of γ' precipitates is not very small (up to 0.5), which does not satisfy this assumption. Intuitively, it is expected that as the volume fraction increases the coarsening rate should increase as the diffusion paths get shorter for a given particle size system. According to a thesis[38], Ardell first modified the LSW theory (MLSW) by considering the effect of volume fraction on the coarsening behaviour. The central idea behind the theory was that

when V_F is not negligibly small the interparticle spacing R cannot be considered as infinity compared with the particle size. The coarsening kinetics by Ardell's MLSW theory was, thus, given by,:

$$\bar{r} - \bar{r}_o = \kappa_m \frac{8}{9} \frac{\gamma D C_e V}{RT} t^n \text{ ----------(10)}$$

the constants being the same as in the previous theory except for κ_m which is a function of V_F only;

$$\kappa_m = \frac{\kappa(V_F)}{\kappa(0)} \text{ ----------(11)}$$

when VF $\rightarrow$ O, $\kappa_m \rightarrow$ 1, 'n' is the growth constant and can be calculated by plotting $\ln(\bar{r} - \bar{r}_o)$ verses ln(t). The variation of κ_m with V_F is shown in Figure 11.

In Ardell's model κ_m is a strong function of V_F whereas later models, however, yielded weaker dependences. Mclean, in a review by Neite and Nembach[36], has compared various results. For V_F = 0.2 ,the following values exist for κ_m : 7.90 (according to Ardell, 1972), 2.19 (Brailsford and Wynblatt, 1979), 1.30 (Davies et al., 1980). The other models allowed for the effects of stress and strain, which cause the precipitates to align and influence the shape of the particles (cubes instead of spheres). They also considered the non-linearity of the Gibbs-Thompson equation and the time

dependence of V_F [36, 38].

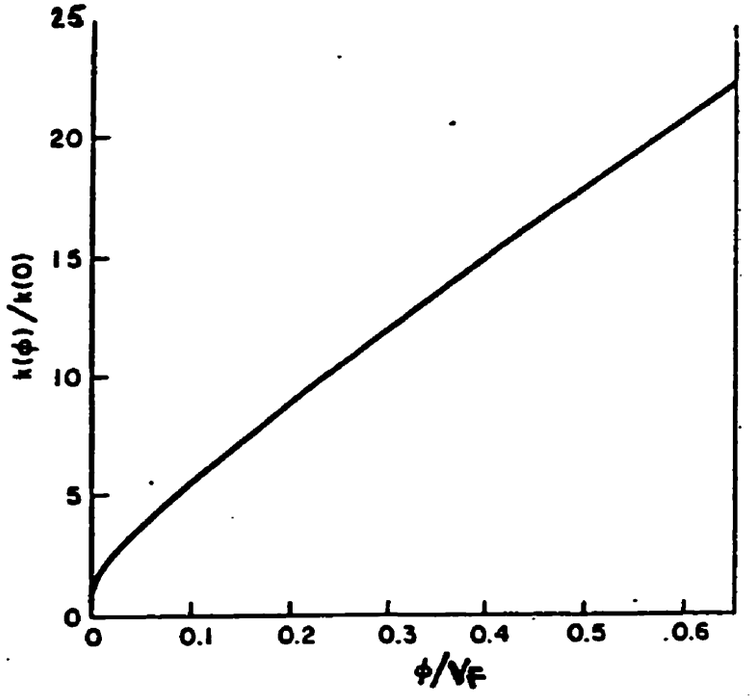

Figure 11. Variation of κ_m (V_F) with V_F in a Diffusion Controlled Coarsening Process.

2.8.3.3 Interface Controlled Coarsening

Coarsening rate equations have also been derived assuming that the most difficult step in the process is for the atoms to go into solution across the precipitate/matrix interface; the growth is then termed interface-controlled. The appropriate rate equation is[39],

$$\bar{r}^2 - \bar{r}_0^2 = \frac{64CC_e\gamma Vt}{8\ell\kappa T} \qquad (12)$$

where C is an interface constant. Thus the particle coarsens in this case obeying a $t^{1/2}$ law[39].

2.8.3.4 LSEM Theory of Ostwald Ripening

The Lifshitz-Slyozov encounter modified theory (LSEM) has been developed by Davies et al[38]. They treated the lattice diffusion controlled coarsening process in the following manner. In the case of appreciably large volume fraction, when a particle is growing its boundary expands outwards and may approach or even touch another one. Therefore, very rapid diffusion will occur, which causes the two particles to coalesce into one. It has been observed that this effect will increase the growth rate and also broaden the particle size distribution. The coarsening rate by the LSEM theory is given by:

$$\bar{r}^{-3} - r_0^{-3} = \kappa_e \frac{8}{9} \frac{D\gamma V C_e}{RT} t \text{ ----------(13)}$$

where,
$$\kappa_e = \frac{\kappa(V_F)}{\kappa(0)} = \frac{27}{4} \frac{\bar{R}_c^3}{\gamma} \text{ ----------(14),}$$

and R_c is a function of V_F. Usually $R_c = 1$. When $Q = 0$, $\gamma=27/4$ and $\kappa_e = 1$, which then becomes the LSW theory [38].

D is the composite coefficient of diffusion of several atom species and is given by $D=D_0 \exp(-Q/RT)$; D_0 is the frequency factor and Q is the activation energy, which is dependent primarily upon the activation energy for diffusion of Al and Ti in the matrix, but is also influenced by the inter-related diffusion of Co, Cr, and Mo away from a growing

γ' particle, C_e is the concentration of solute (γ' forming elements) in equilibrium with a particle of infinite radius, V is the molar volume of the precipitate, and R is the gas constant. By rearranging the above equation one can arrive at,

$$\ell n \left(\frac{\kappa^3 T}{C_e} \right) = \text{Constant} + \frac{-Q}{RT} \quad \text{----------(15)}$$

The activation energy can therefore be determined from the slope of a plot of $\ell n \left[\frac{\kappa^3 T}{C_e} \right]$ against 1/T where κ is the slope of the plot of 'r^3-r_0^3' and t[36].

Both the MLSW theory and LSEM theories still follow $t^{1/3}$ law of the LSW theory, the only difference being they give the effect of volume fraction on the growth rate constant and particle size distribution. The effect of encounters in the later theory is to increase the growth rate although effect is not significant; the rate constant varies by a factor approximately three over the entire volume-fraction range. It has been found that the LSEM gives the best fit to the experimental data.

2.9 Modelling of Hardening Mechanisms as a Result of γ-γ' Interaction in IN-738

The γ'-precipitating materials are chiefly strengthened by two mechanisms: particle hardening by the γ'-precipitates and solid-solution hardening of the matrix. The respective contribution to the total critical resolved shear stress τ_t (index t for total) are τ_p

(p for particle) and τ_s (s for solid-solution). If there are no precipitates, τ_t equals τ_s. It is not possible to produce specimens for which τ_p is finite and τ_s vanishes. Models of particle hardening relate τ_p to the properties of the particles.

In precipitation hardened alloys, the matrix dislocations are known to overcome the precipitate barriers by one of the following mechanisms:

(a) bypassing the precipitates by Orowan mechanism

(b) shearing of precipitates

(c) climbing over the precipitates

2.9.1 Bypassing the Precipitates by Orowan Mechanism

Here it is envisaged that dislocations remain in their glide planes and can penetrate an array of particles by an Orowan bowing mechanism when a critical shear stress τ_c is exceeded where[8]

$$\tau_c = A(\theta)\frac{Gb}{2\pi L_{min}}\ln(\frac{L_{min}}{r_0}) \text{----------(18)}$$

and,

$A(\theta)$ is the geometrical factor ~ 1, r_0 is the dislocation core radius, b is the Burgers vector, μ is the shear modulus and L_{min} is the inter-particle spacing in the glide plane if the particles form a sequential array, and is given by:

$$L_{min} = 0.82r[\{\frac{\pi}{V_F}\}^{1/2} - 2] \text{----------(19)}$$

2.9.2. Cutting of Particles

According to Henderson and Mclean, when particle and matrix have similar crystal

structures and orientations, as in IN-738, the matrix dislocations can shear the particles when the stress is sufficiently high to generate anti-phase boundaries (APB's) in particles. The minimum threshold for particle cutting τ_{pc} occurs when pairs of dislocations are propagated, the second destroying the APB created by the first. Depending on the dislocation shape,

$$\tau_{pc} = (\frac{\gamma}{2b})[(\frac{4f}{\pi})^{1/2}] \text{----------(20)}$$

where γ is the APB energy and f is the volume fraction of particles[48].

2.9.3 Climb Around Particles

Henderson et.al.[48] have argued that when a gliding dislocation is arrested at an array of particles, its delay is only temporary if it can by-pass these obstacles by extending a part , or all of the dislocation by climbing out of the glide plane to avoid the particles during creep. The corresponding climb can be of two types, the first being the localised climb where most of the dislocation remains in the glide plane and a small segment profiles the particle. The other mode is termed as general climb where all of the dislocation moves out of the glide plane. These two processes lead to two different threshold stresses[48], viz.,

$\sigma_{lc} = \frac{\tau_b}{\sqrt{2}}$ for localized climb

$\sigma_{gc} = \frac{f^{3/2}}{2^{5/4}} \tau_b$ for general climb

where the subscripts '*lc*' stands for local climb and '*gc*' for general climb, '*f*' is the volume fraction of gamma prime particles and τ_b is the Orowan bowing stress. It is argued that the localized climb can occur more rapidly because it involves less mass transport and will be the dominant climb mechanism when activated[48].

If the precipitates are incoherent and large, dislocations circumvent them by Orowan looping. The same holds true for coherent particles, if they are widely spaced. Fine, closely spaced, coherent secondary γ' precipitates in IN-738, which are a dominant barrier to dislocation bowing are sheared during the room temperature deformation[46]. Dislocation climb is a thermally activated process, and therefore would not contribute significantly to the precipitation hardening during room temperature deformation in this material. Dislocations in IN-738 also interact with the γ' precipitate strain field due to the misfit between the precipitate particles and the matrix[32].

2.9.4. Evaluation of Increment in Flow Stress Resulting From Dislocation-γ' Precipitates Interaction During Room Temperature Deformation

A coherent, shearable γ' precipitate may interact with a dislocation via more than one interaction mechanism. Two types of elementary interactions have been distinguished[36],

i) energy storing interactions,

ii) elastic interactions.

Energy is stored in the particle during the shearing process if the particle surface area is increased or if an anti-phase boundary (APB) is created. Elastic interactions are due to

difference in lattice constant, the modulus or the stacking fault energy between the particle and matrix. In Ni base superalloys containing coherent shearable γ' precipitates, the surface energy hardening or the chemical hardening and modulus mismatch hardening are weak and therefore, the energy storing interaction is mainly by the creation of APB in the precipitates[36]. The Burgers vectors of perfect dislocations in ordered precipitates of γ' phase with $L1_2$ crystal structure are twice the length of (or the magnitude of) those in the corresponding fcc matrix (γ matrix). Therefore shearing of γ' precipitates by matrix dislocations lead to planar defects in γ' phase e.g. APB and stacking faults[46]. The shearing mechanism by pairs of a/2<110> type matrix dislocation , coupled by APB is relatively well understood[47]. Mukherji et.al. have observed stacking fault formation in γ' phase during monotonic deformation at elevated temperatures[32]. None of the existing models are sufficiently accurate to calculate the contribution of stacking fault hardening to the critical resolved shear stress(CRSS). This contribution, is likely to be small at room temperature deformation of Ni base superalloys[36].

It is worth noting that the numerical factors appearing in the formulae relating the contribution of particle hardening to the flow-stress(τ_p) to the characteristic parameters of the particle dispersion are not reliable unless these factors have been verified experimentally. Even slight inaccuracies of the averaging procedures may introduce appreciable errors. Thus, the two major contributions to the CRSS of γ' hardening of IN-738 are misfit hardening and order hardening(shearing of γ' and the associated APB formation). A critical strain ε_c has been defined as[36],

$$\varepsilon_c = \frac{\gamma}{\sqrt{8}G_F b} \text{----------(21)}$$

where γ is the APB energy and is equal to 170×10^{-3} J/m^2, G_F is the shear modulus of the γ matrix and b is he Burgers vector. If $|\varepsilon|$, coherency strain exceeds ε_c, misfit hardening outweighs order hardening[36].

It has been recognized that the γ'/γ lattice mismatch is one of the main factors affecting the mechanical strength of Ni-base superalloys[5]. A coherent particle, whose lattice constant differs from that of the matrix, produces a strain field which interacts with dislocations. Since it yields a vanishing interaction force between a screw dislocation and a misfitting particle, only edge dislocation interactions are significant. As discussed in section 2.8.2, the unconstrained lattice misfit parameter is represented by δ. Fine coherent γ' -precipitates embedded in a γ matrix are normally constrained. The relative difference in lattice constant of such constrained particles is called the constrained lattice misfit strain(ε). A good approximation for ε is $(2/3)\delta$[36], and is also termed as the coherency strain. The morphology of γ' precipitates depends on ε and the radius r of the particles. As ε increases the morphology changes from spheres to cuboids, to cuboidal arrays, and finally to dendrites.

Gerold and Haberkorn[28], and Janson and Melandar, in a review[36],found the dependence of τ_p (particle hardening contribution) on the coherency strain in the following way,

$$\tau_p = \alpha\{G_F|\varepsilon|\}^{3/2}\left[\frac{V_F r b}{2S}\right]^{1/2} \text{----------(22)}$$

$$\text{using } S = \frac{G_F b^2}{2}$$

$$\tau_p = \alpha G_F |\varepsilon|^{3/2} [\frac{r}{b}]^{1/2}$$

The three groups applied slightly different averaging techniques, i.e., the flow-stress could be the square root of the sum of the squares of its components, or the method of mixtures, in which the flow-stress is a weighted average of its components. Therefore the three values derived from 'α', the averaging constant, differ by ±16%: 3.0, 3.7 and 4.1 respectively for the three groups.

2.10 Scope and Nature of Present Investigation

Cast IN-738 superalloy has long been considered to be difficult-to-weld, due to the occurrence of heat-affected zone microfissuring during the welding cycle or after the post-weld heat-treatments. The heat-treatment schemes proposed in the open literature consist of a solution heat-treatment at 1120^0 C, which is now known to provide a partial solution treatment only. The metastability of various phases in this material is a known fact but no comprehensive study has been undertaken to characterize the microstructural response of this material to a variety of heat-treatment (pre-weld) schemes. The objective of the present study was to gain a comprehensive understanding of the microstructural behavior and the strengthening response of cast Incoloy 738. Hence the primary focus of the present investigation was a thorough microstructural characterization of the various specimens using optical microscopy, X-ray diffraction, scanning X-ray microanalysis and

analytical electron microscopy. This was performed to give an understanding of the following aspects:

(i) the grain-structure, morphology of various phases in the as-received material;

(ii) the composition and the lattice parameter of major and minor phases;

(iii) microstructure as a function of solution-treatment temperatures;

(iv) microstructure of solution-treated and aged specimens;

(v) lattice constant, volume-fraction, morphology, and distribution of precipitate phases;

(vi) coarsening rate of secondary γ' particles and activation energy for coarsening;

(viii) estimation of coherency strains in the heat-treated specimens;

(ix) nature of grain boundaries in the heat-treated specimens;

(x) microstructural inhomogeneity in the form of eutectic islands using carbon extraction replicas;

(xi) quench cracks in solution-treated samples.

Since primary focus of the present investigation was to understand the microstructural response of IN-738 to heat-treatments, no welding was carried out in this first phase. This investigation characterizes the metastability of the various phases in this material thereby giving an insight in the metallurgical mechanisms responsible for the liquation and cracking of the grain boundaries and the minor phases. These results would be used in the next phase to form a basis for the design of suitable pre-weld heat-treatments. It is expected that the resulting microstructure would resist heat-affected zone micro fissuring during the welding.

Chapter 3

EXPERIMENTAL TECHNIQUES

3.1 Material

The material used in this investigation was a commercial IN-738 superalloy provided by Special Metals Corporation. The material was provided in the form of a cast cylindrical billet, 8.5 cm in diameter and its chemical composition is given in Table 5.

Table 5. Alloy IN-738 Composition

Element	wt%
Carbon (C)	0.13
Cobalt (Co)	8.48
Chromium (Cr)	14.8
Molybdenum (Mo)	1.81
Tungsten (W)	1.95
Tantalum (Ta) + Niobium (Nb)	4.70
Titanium (Ti)	3.18
Aluminum (Al)	2.77
Iron (Fe)	0.09
Manganese (Mn)	0.01
Phosphorous (P)	0.013
Sulfur (S)	0.004
Silicon (Si)	0.10

* Analysed at Arrow Laboratories, U.S.A., not analyzed for Boron

3.2 Sample Preparation & Heat-Treatments

Cuboidal samples were cut out of a circular slice at a constant distance from the

periphery. The surface perpendicular to the dendritic growth was used to characterize the grain-structure. These samples were then solution-treated at various temperatures ranging from 1,120°C to 1,225°C. These samples were further aged at 845°C for various lengths of time in order to produce conditions of under-aging, peak-aging and over-aging. Heat-treatment samples were sealed in vycor capsules, partially filled with argon to prevent oxidation.

3.3 Hardness Measurements

The hardness of the sample was measured using a 30 kg load on a standard Vickers hardness tester. Six to ten measurements were taken per sample and hardness-aging curves for various solution-treatment temperatures were plotted.

3.4 Optical and Scanning Electron Microscopy

Samples were observed in an optical microscope for its grain structure after polishing and etching using standard metallographic techniques. The etchant was a solution containing 7.5 gms. each of ferric and cupric chloride, 100 ml of hydrocholoric acid, and 17 ml of nitric acid. The distribution and morphology of MC and $M_{23}C_6$ carbides were observed in a JEOL-840 scanning electron microscope using the secondary electron image, back-scattered electron image, and the combined image. The composition analysis of particles was carried out using Noran 5500 EDS system equipped with light element analysis detector. The quantification was done using Noran micro-Q analytical software and the standard semi-quantitative analytical software.

3.5 Preparation of Thin Foils and Transmission Electron Microscopy

One mm thick strips were cut out from the heat-treated samples using the electric discharge machine and were reduced to 100μm thickness using a 600 grit abrasive paper. 3mm diameter disks were punched from the strips . Six samples were prepared per heat-treatment for electropolishing. These discs were thinned with a jet electropolishing unit using a solution of 8% perchloric acid in ethanol at -20°C. The electric current used was in the range of 1.4-1.6 amperes which resulted in well polished thin foils. The foils were observed in a JEOL-2000FX transmission electron microscope for the general microstructure, especially, the distribution of γ' precipitates, and carbides.

3.6 Volume Fraction Determination

The volume fraction of γ' precipitates was determined using electrochemical extraction technique by performing anodic dissolution of the precipitates in a solution of one percent citric-acid and one percent ammonium sulfate in water.

The samples (anode) were suspended by a fine platinum wire passed through a hole drilled in each sample, and 4 cm^2 of platinum foil served as the cathode. The electrolysis was carried out using 200 ml of electrolyte, 100-200 mA current (current density ~ 0.01-0.08 amp/cm^2), at a potential difference of 20 volts and above. The electrolysis was continued for three hours at ambient temperature and the electrolyte was stirred slowly using a magnetic stirrer. Most of the γ' particles retained on the surface of

the sample and the rest were recovered from the solution by centrifuging.

Following dissolution, the solid sample to which virtually all the γ' particle adhered was removed to a stirred beaker and leached for five minutes to remove the adsorbed electrolyte. As established by Kriege and Sullivan[35], it was assumed that minimal γ' was lost during washing. The specimen plus adhering γ' was then dried under a heat lamp for thirty minutes and weighed. Any coarse γ' which did not adhere to the sample was removed from the electrolyte by centrifuging. Following this, the γ' was first washed with water, then with methanol, and then dried in a centrifuge tube under a heat lamp. The dried γ' was then removed from the sample disc by scrapping with a scalpel. The total γ' dust was then weighed with a precision electronic balance.

Carbides always accompany the extracted γ' and a correction for this contamination was made by performing a second anodic dissolution on similar samples using 200 ml of 10% HCl-methanol solution containing 1% tartaric acid as the electrolyte. The anode and cathode material and configuration was identical to that used in the γ' extraction. About 200 ml of electrolyte was carefully decanted and allowed to settle overnight. The remaining electrolyte, which contained the bulk of the separated material, was centrifuged and the insoluble particles were washed successively with 10% HCl-methanol, methanol and finally with water. The fines which settled out of a decanted portion of the electrolyte overnight were treated in the same manner and added to the major fraction of the separated phases. The residue was dried and the weight percent of carbide particles (MC + $M_{23}C_6$) was calculated. This value was then subtracted from the

amount of γ' + carbides to obtain the net amount of γ' recovered.

3.7 X-ray Diffractometer and Lattice Parameter

Phase identification of the electrolytically extracted particles and the lattice parameter analysis was carried out using a Rigaku X-ray diffractometer in a continuous scanning mode using Cu-Kα radiation. The extracted particles were placed as a thick paste on the concave side of a glass slide using a few drops of acetone. The lattice parameter was evaluated using a cell-refinement software.

Chapter 4

RESULTS & DISCUSSIONS

4.1 Macrostructure of the IN-738 Casting

Figure 12 shows the macrostructure of the cast IN-738 billet. As can be seen, many grains form at or near to the surface of the chill zone. It has been observed by Gandin and co-workers that from this outer "equiaxed region", a few columnar grains grow preferentially in <100> crystallographic directions[4]. The columnar grains give way to a zone of equiaxed grains when the constitutional supercooling in front of the columnar grains becomes large enough, thus providing plenty of independently growing nuclei ahead of the columnar grains.

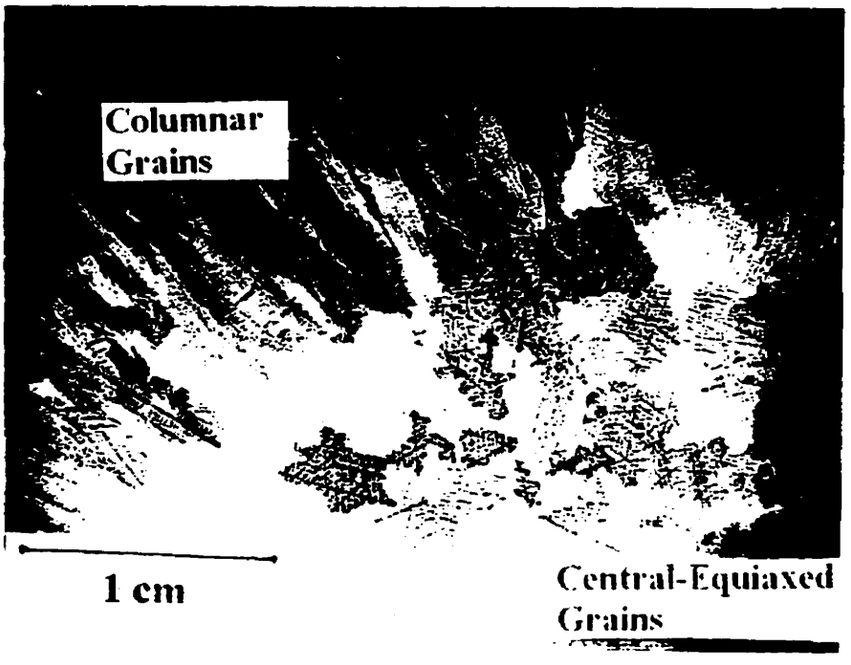

Figure 12 Cross-sectional microstructure of cast IN-738 billet, 3.4X

The optical microstructure in a direction perpendicular to the growing columnar grains is shown in Figure 13. It was found that the grain size increased from 110 μm (Figure 13a) to 700 μm (Figure 13c), which in turn depended on the distance from the outer periphery at which the samples were sectioned. Therefore it was necessary to cut heat-treatment specimens out of the billet at a fixed distance from the periphery in order to have an identical starting microstructure.

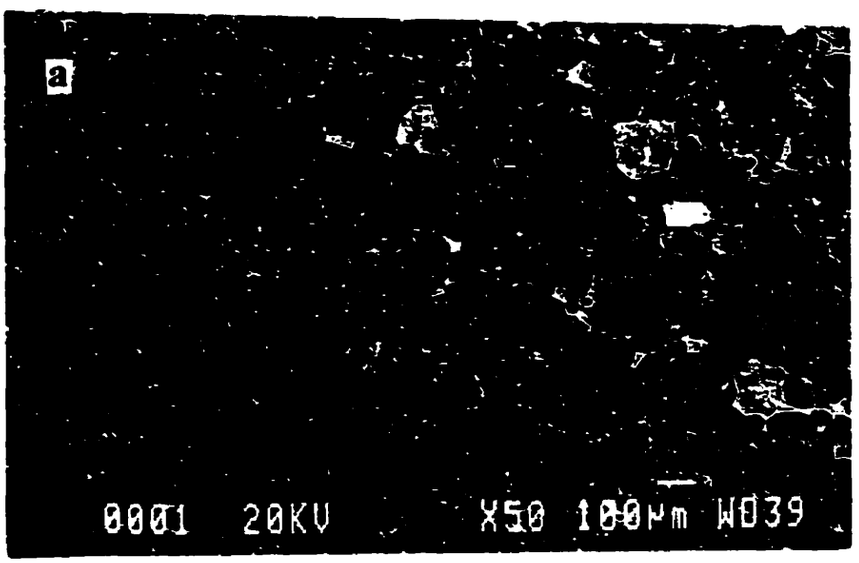

Figure 13 (continued)

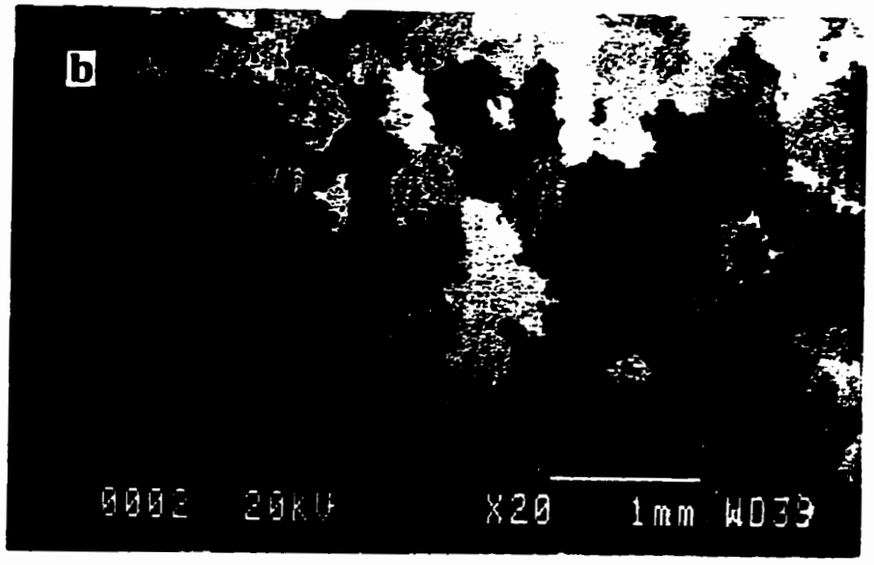

Figure 13: Transverse microstructure of the billet cross-section with a (a) grain size of 110µm, at a distance of 0.1cm from outer periphery, (b) grain size of 400µm, at a distance of 0.5cm from outer periphery, (c) grain size of 700µm, at a distance of

1.0cm from outer periphery.

4.2 Transverse Microstructure

Figure 14(a) shows the cellular dendritic segregation and the alignment of the primary MC carbide particles, that appear as black dots in the micrograph, also confirmed by EDS-SEM analysis. The secondary dendritic arms can be observed in the optical micrograph in Figure 14(b). The EDS (SQ analysis) for the dendritic and interdendritic regions is presented in Figures 14 (c) and (d).The interdendritic region in 14(b) has less Tungsten and more Aluminum and Titanium. Even though the analysis is semi-quantitative it provides a relative compositional difference between the two regions.

Figure 14 (continued)

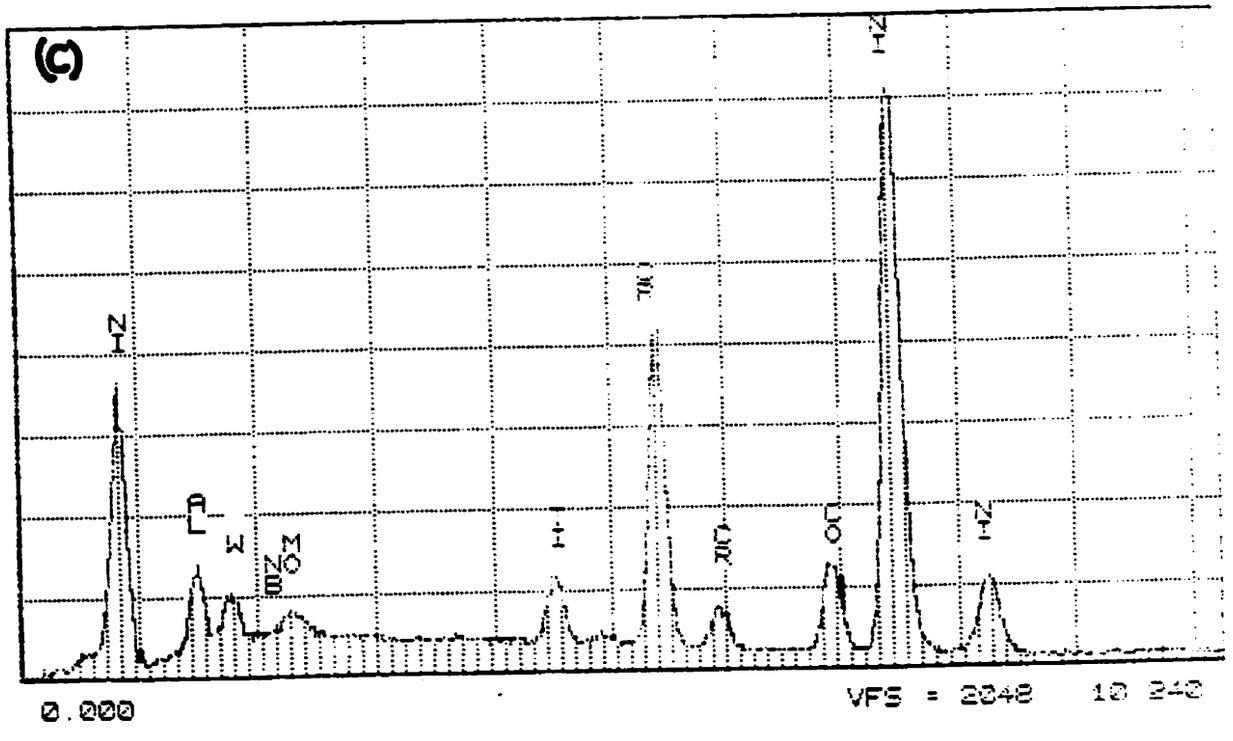

Figure 14 (continued)

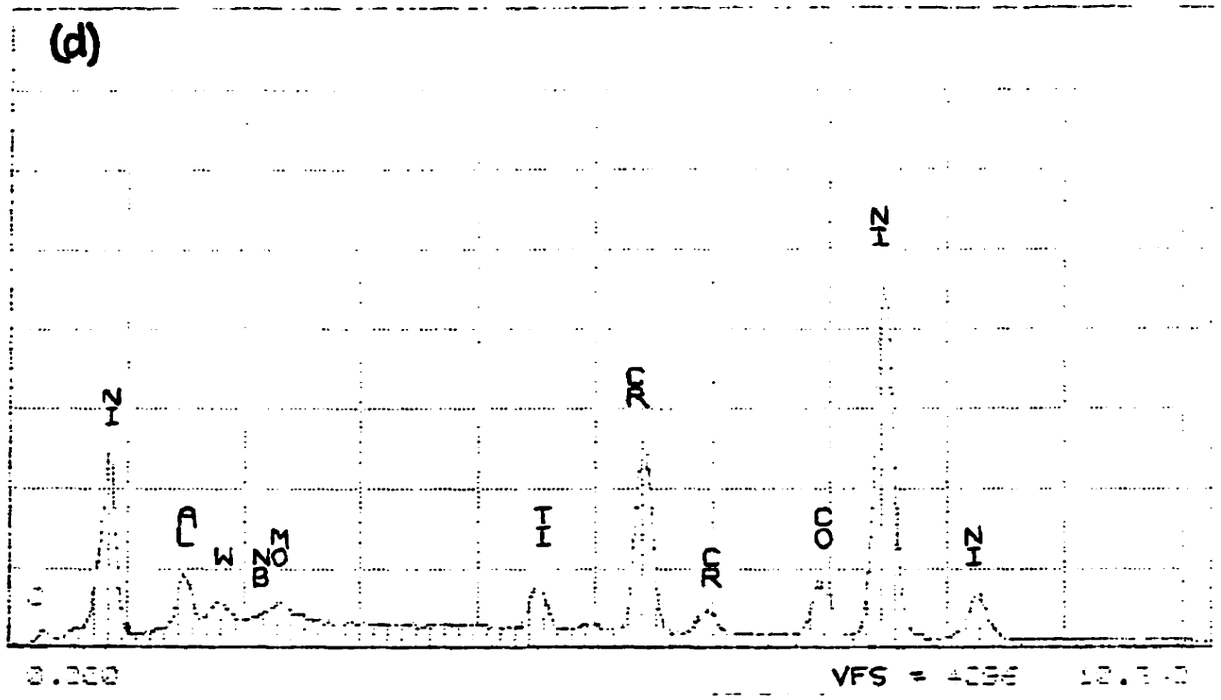

Figure 14:(a) Optical image showing solidification macrostructure and the alignment of MC carbides in IN-738, 50X, (b) microstructure showing secondary dendritic arms and the interdendritic regions, 200X, (c) EDS spectrum (SQ analysis) for the dendritic regions, (d) EDS spectrum (SQ analysis) for the interdendritic regions.

4.3 Casting Micropores

Micropores were observed in the material. An example is shown in Figure 15. However, these micropores do not adversely affect mechanical properties of IN-738 owing to their small volume fraction and large grain size of the material. The usual fracture mode of this material is intergranular and large grain sizes imply minimum grain boundary area, and since these micropores rarely occur at the boundaries hence they can

not become site for crack initiation.

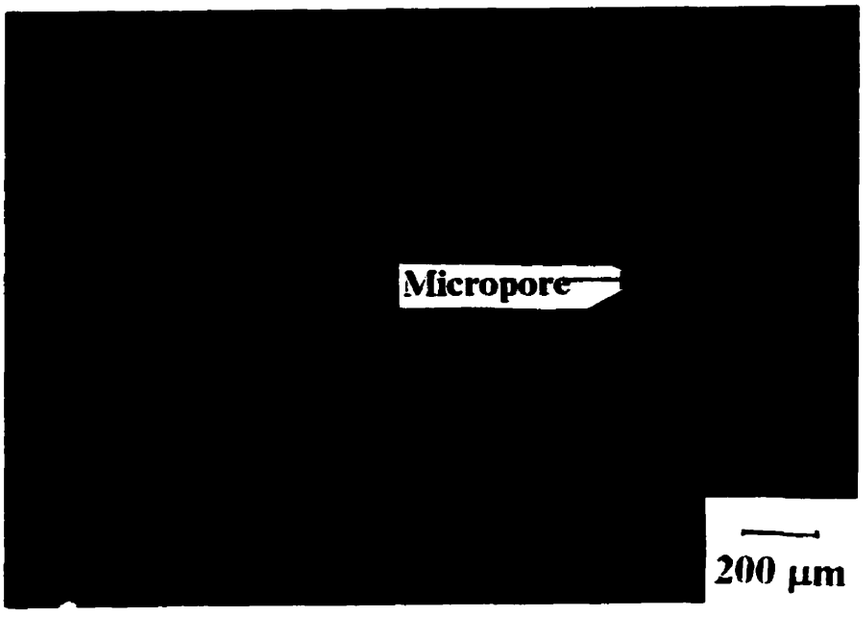

Figure 15 Optical micrograph from as polished sample showing casting micropores, 50X.

4.4 Microstructure of As-Received Material

The as received cast IN-738 microstructure is shown in Figure 16. The optical micrograph (Fig.16a) reveals a cellular dendritic structure with a coring at the cell boundaries due to elemental segregation. The grain boundaries in the SEM micrograph are free of any $M_{23}C_6$ carbide precipitation as shown in figure 16 (b). The TEM dark field micrograph in figure16(c) shows a unimodal distribution of cuboidal shaped particles, which was found to be primary γ' particles by the selected area diffraction pattern analysis discussed later.

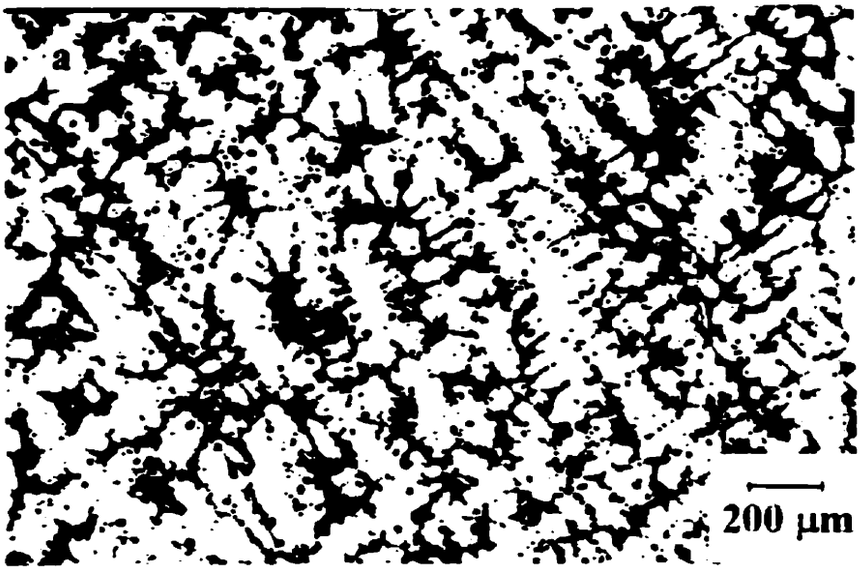

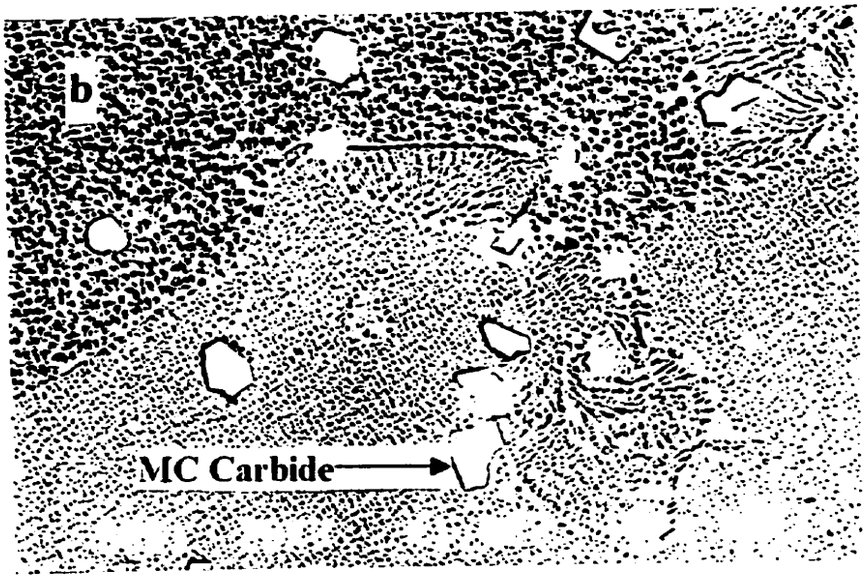

Figure 16 (continued)

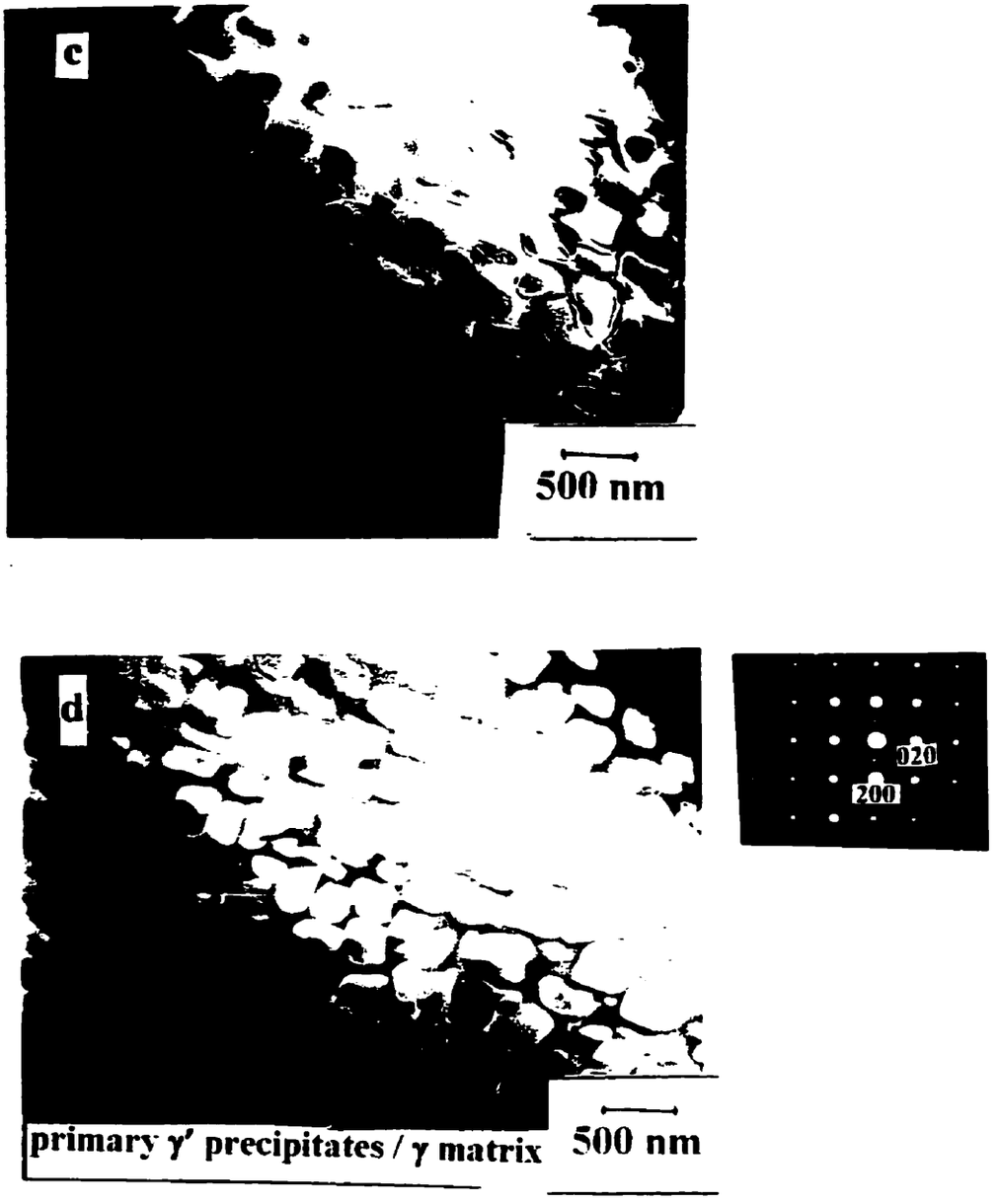

Figure 16:(a) Optical micrograph from the as received sample revealing cellular dendritic structure, 50X (b) SEM micrograph showing primary MC carbides and a grain boundary free from the presence of $M_{23}C_6$ carbides, (c) and (d) TEM, centered bright field and dark field respectively from a superlattice spot along [001] beam direction from as received sample.

4.5.Heat Treatments and Resulting Microstructures

The standard solution heat-treatment of IN738 consists of 2 hours at 1,120°C. This solution treatment temperature results only in a partial dissolution of second phase precipitates[27]. It has been suggested that the γ' solvus is in the range of 1,160°C-1,175°C[27] but experiments showed that the specimens solution treated for two hours at 1,175°C and 1,225°C had primary γ' (measurable volume fraction for the 1,175°C sample) in them. Therefore for all practical purposes three different solution treatment temperatures were used to determine the heat treatment response of cast IN738, namely, 1,120°C, 1,175°C and 1,225°C following which the samples were cooled to room temperature and then aged at 845°C for various lengths of time as indicated in Table 6.

Table 6 Schedule for Heat Treatments

Solution Treatment Temperature	**Aging Hours at 845°C**
1,120°C/2 hrs.	0*, 0**, 8, 12, 16, 24, 72, 120
1,150°C and Brine Quenched	--
1,175°C/2 hrs.	0**, 2, 12, 24, 72
1,225°C/2 hrs.	0**, 2, 12, 24, 72
* - Brine Quenched, ** - Air Cooled	

4.5.1 Solution Treated Microstructure

The solution-treated samples were brine quenched or air cooled. These were then observed optically, through SEM and TEM following the hardness measurements. The micrographs are shown in Figure 17. Figure 17(a) shows an optical micrograph for a sample solution treated and brine-quenched from 1120^{0}C. Figure 17b is a SEM micrograph of the same sample showing linear grain-boundaries free from secondary precipitation. The TEM dark field image (Fig. 17c) from a superlattice spot along the [001] beam direction shows the undissolved primary γ' particles. The optical micrograph of the air cooled sample was similar. Figure 17d is another TEM dark field image using same operating conditions from an air-cooled sample from the same solution-treatment temperature. The slower cooling rate resulted in the precipitation of fine secondary precipitates. Figure 17e is a TEM dark field image from a sample solution-treated at 1175^{0}C and brine-quenched, using a [001] superlattice spot, showing the existence of partially dissolved primary γ' particles.

The samples were brine quenched to avoid the precipitation of secondary γ' precipitates during cooling. The high quenching stresses resulted in the tearing along the grain boundaries, both on the surface as well as in the bulk, for the samples solution treated at 1150^{0}C and above. This aspect will be discussed later. Thus the only sample that could withstand the quenching stresses was the one solution treated at 1120^{0}C. Due to the quench cracks, another set of samples were air cooled from various solution treatment temperatures and were found to be free from cracking. For accuracy and ease of measurements, thin foils obtained from the brine quenched samples were used to measure the γ' size. The shrinkage stresses due to fast cooling resulted in generation of interfacial

dislocation around the primary γ' particles, which are the γ' particles that form on solidification and did not dissolve during solution heat treatment, as seen in the bright field image, figure 17(f).

A higher solution-treatment temperature (STT) of 1175^{0}C dissolved more of primary γ' than at 1,120°C STT. The size of the primary γ' particles was also reduced due to dissolution and resulted in an unimodal distribution of what is known as degenerate γ' particles, i.e., particles which are somewhere in between a cuboid and a spheroid. A further increase in the STT to 1225^0 C enhanced the dissolution process. The TEM examination suggested that the volume fraction of primary γ' phase got reduced significantly.

Figure 17 (continued)

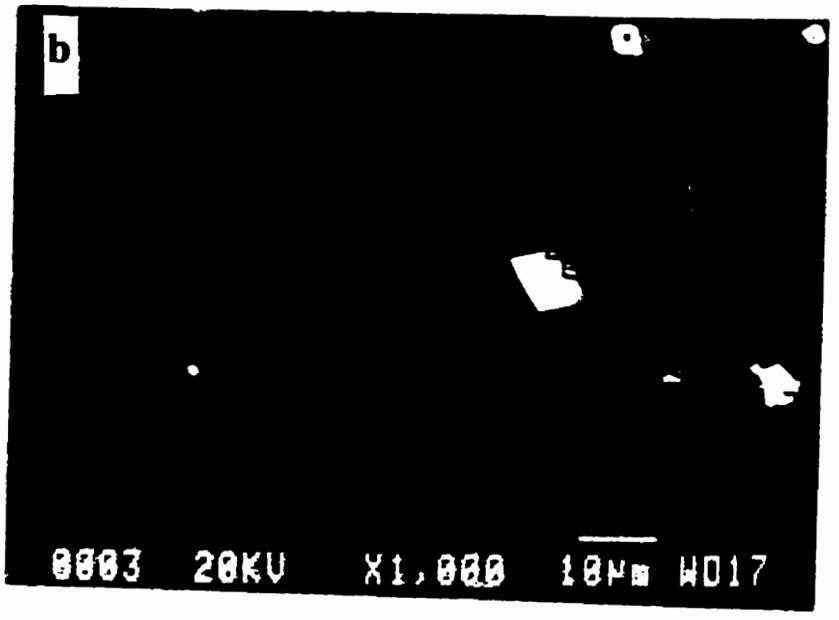

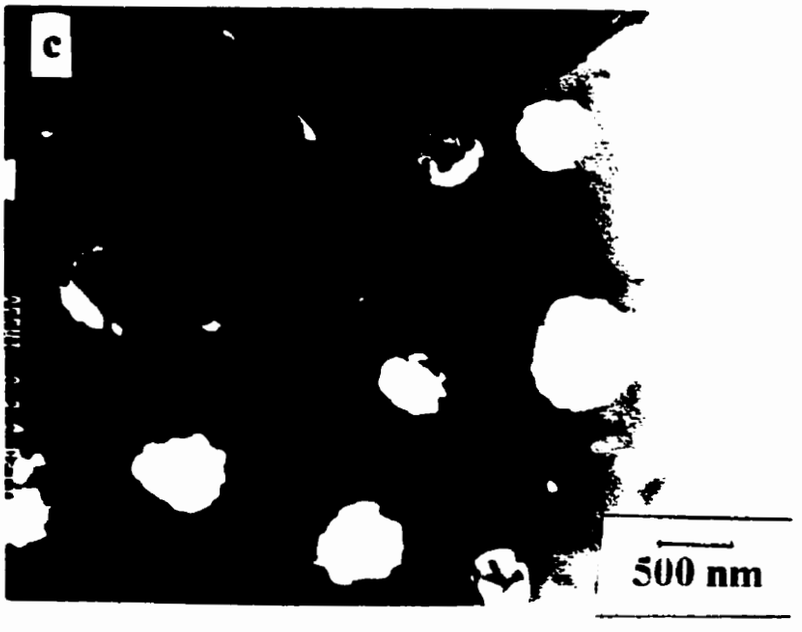

Figure 17 (continued)

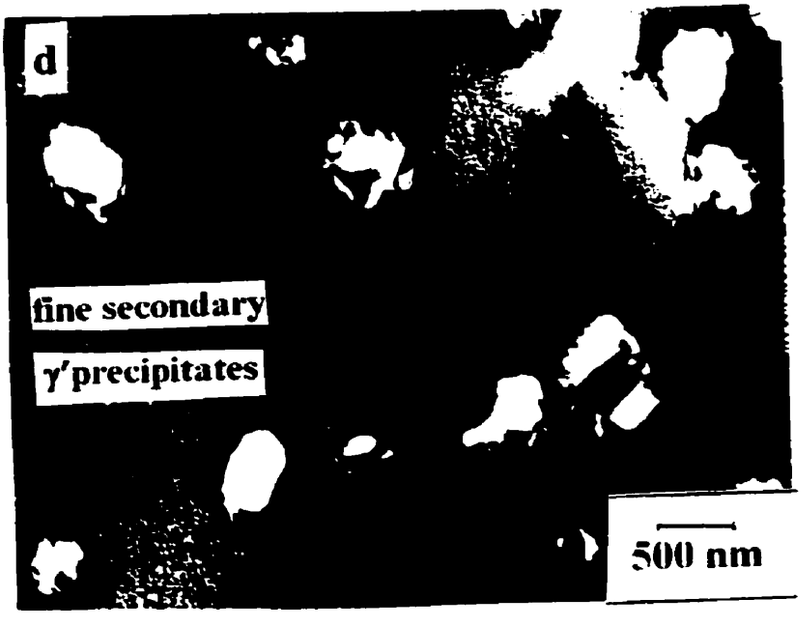

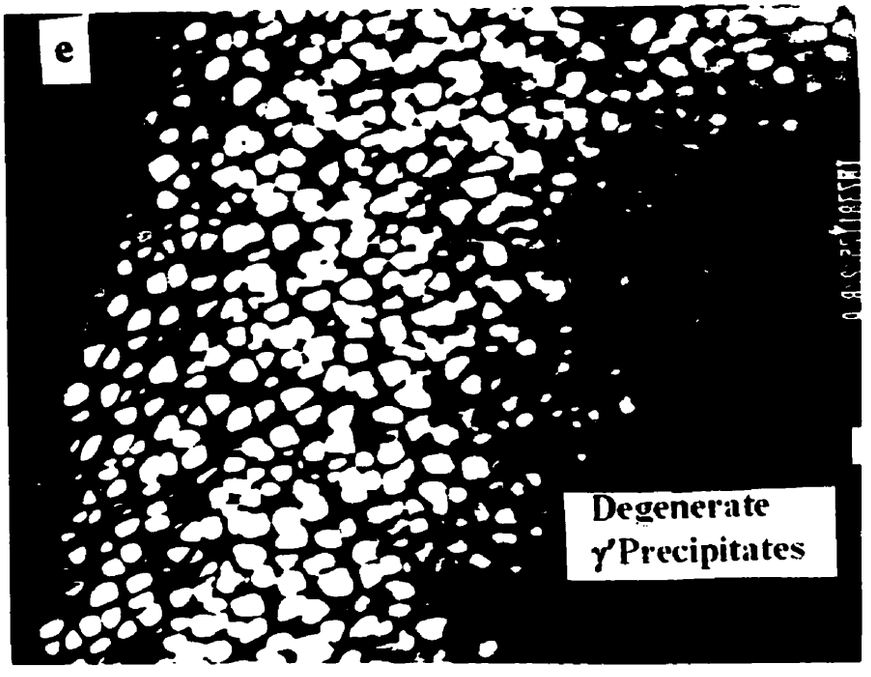

Figure 17 (continued)

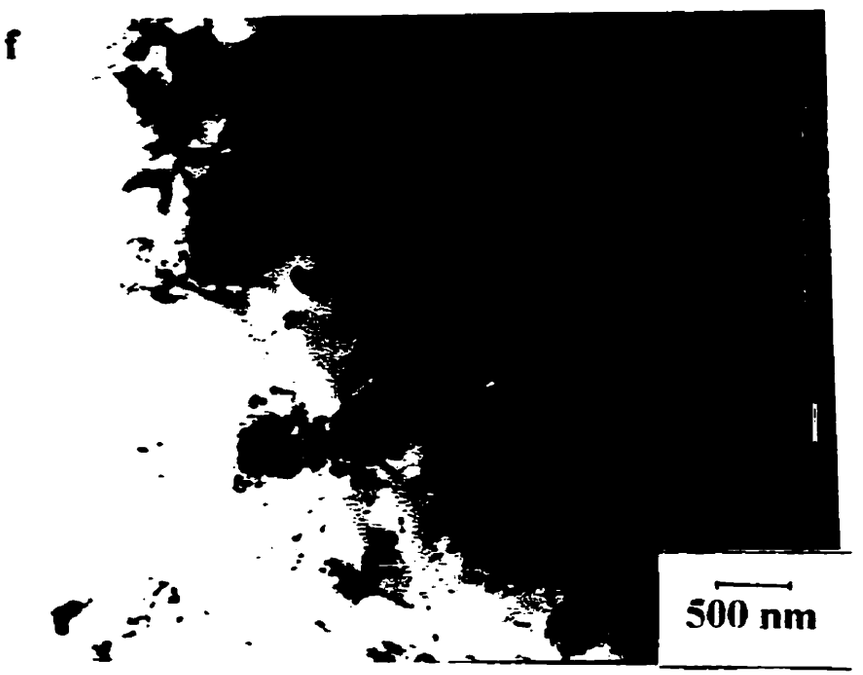

Figure 17: (a) Optical micrograph of a sample solution treated at 1120^{0}C/2 hrs. brine-quenched,50X, (b) SEM micrograph of a sample solution treated at 1120^{0}C/2 hrs, brine-quenched, (c) TEM micrograph, centered dark field along [001] superlattice spots of a sample ST at 1120^{0}C/2 hrs.(brine quenched), (d) TEM micrograph, centered dark field along [001] superlattice spots of a sample ST at 1120^{0}C/2 hrs. (air cooled), (e)TEM micrograph, centered dark field along [001] superlattice spot of a sample ST at 1175^{0}C/2 hrs.(brine quenched), (f) TEM micrograph, centered bright field along [001] superlattice spots of a sample ST at 1120^{0}C/2 hrs.(brine quenched).

4.5.2 Solution-Treatment and Aging

As reported in the previous section the standard heat-treatment of IN-738 consists of a solution-treatment at 1,120°C for two hours that results only in a partial solution treatment of the sample. Samples were therefore, solution treated at three different solution treatment temperatures, namely, 1,120°C, 1,175°C and 1,225°C, following which

the samples were aged at 845°C for various lengths of time and their hardness was measured.

4.5.2.1 Hardness Aging Curves

Hardness-Aging curves after the solution-treatment at 1,120°C, 1,175°C and 1,225°C are shown in Figures 18(a-d). It appears that for 1,120°C solution treatment the peak-aging time is in the range of 16-24 hours. For 1,175°C and 1,225°C solution-treatment the peak hardness was achieved after 60-90 minutes of aging at 845°C. The peak hardness values are although higher for 1,225°C solution treatment than 1,175°C solution treatment and aging. The peak-hardness value for the 1,120°C and 1,225°C solution treated and aged (STA) samples were in the range of 480-485 Hv. 1,225°C STA samples overaged to a greater extent than 1,175°C STA in the same length of time. Thus one observes hardness values of 455 and 425 respectively after 72 hours of aging for these two ST material.

Inspite of the fact that the γ' precipitation occurs extremely rapidly, it is possible to suppress the γ' formation to a significant extent by brine-quenching from the solution treatment (ST) temperature. This is shown in Figure 18(d) where it is seen that hardness value of the solution treated and brine quenched specimens are lower than those of the solution treated and air cooled specimens. Also noticeable is the fact that hardness drops with increasing solution-treatment temperature. This feature is more pronounced for the brine quenched samples due to the much reduced precipitation of secondary γ' particles

during cooling, thus revealing the softening effect due to the dissolution of primary γ' only. Therefore for the ST and brine-quenched samples the amount of primary γ' particles together with its size determines the strength of the material.

If the three aging curves are compared, it is seen that the peak hardness in the material ST at 1,120°C occurred after 24 hour as compared to 60-90 minutes of aging for 1,175°C and 1,225°C specimens. Thus it appears that the precipitation and coarsening rate of secondary γ' particles in 1,120°C STA samples is significantly influenced by a reduced solution treatment temperature and the presence of a large volume fraction of primary γ' particles i.e. the amount of solute that form γ' are in considerably smaller quantity.

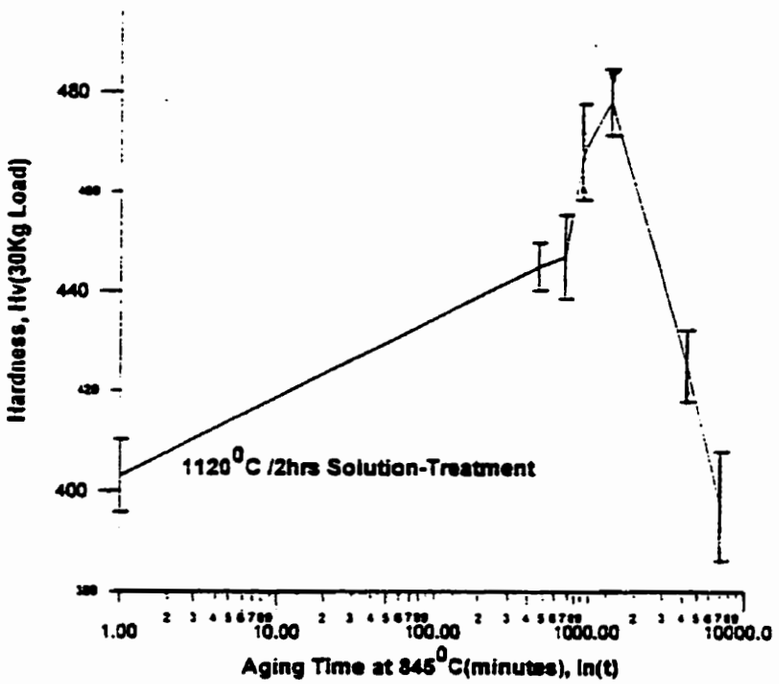

Figure 18 (continued)

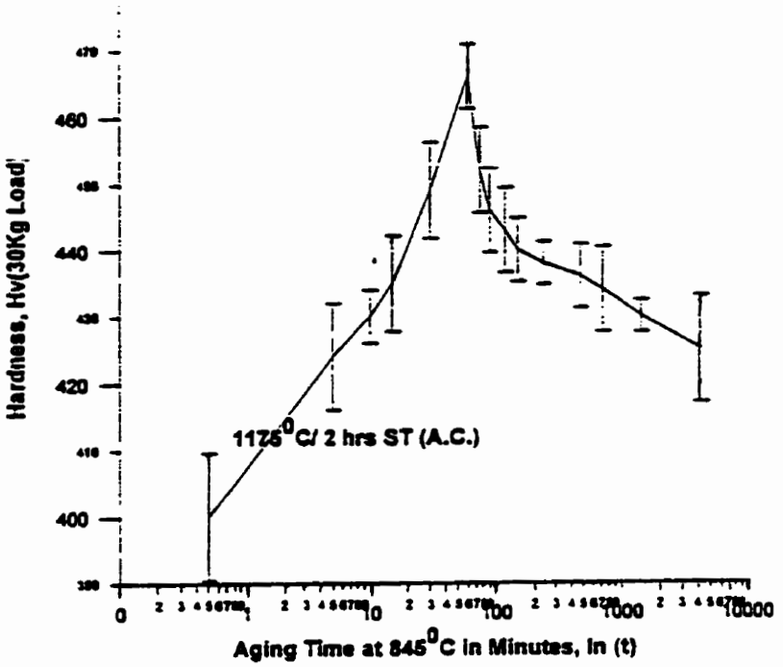

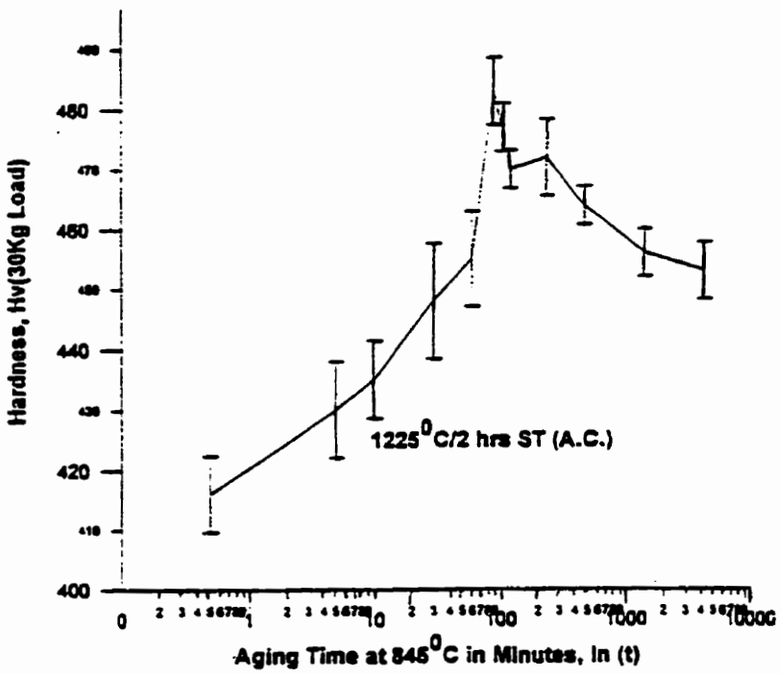

Figure 18 (continued)

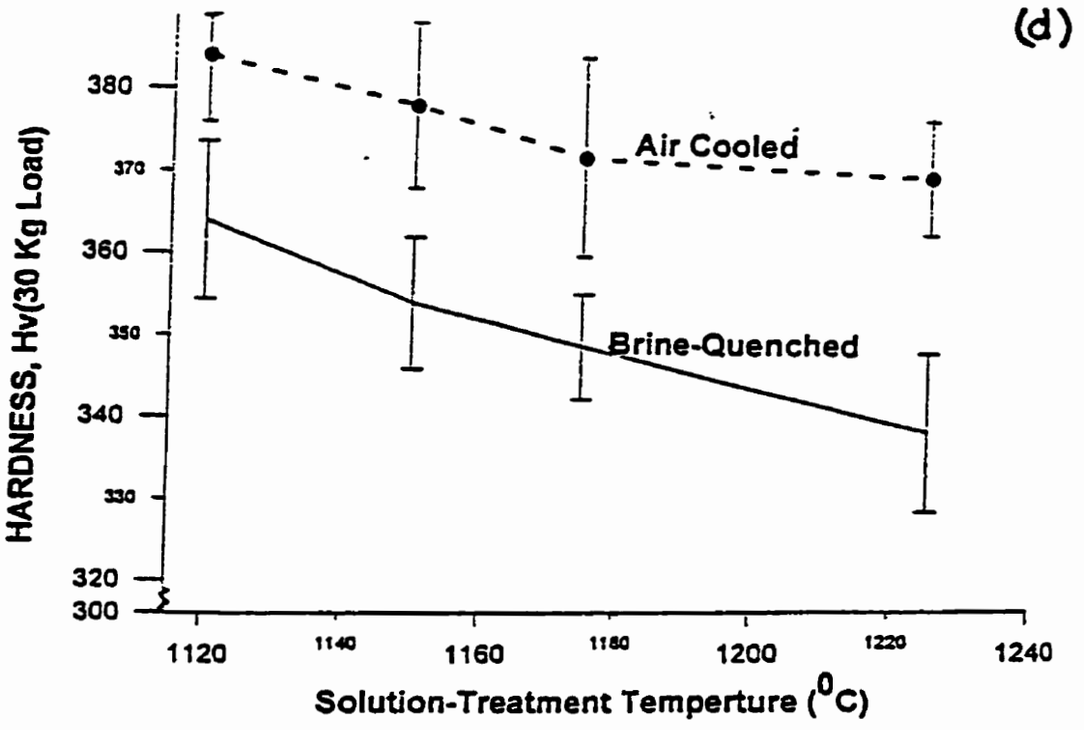

Figure18: Hardness-aging plots at 845^{0}C for solution treatment (a) at 1120^{0}C, (b) at 1175^{0}C, (c) at 1225^{0}C, (d) Hardness as a function of solution-treatment temperature(no aging) for two different cooling rates.

4.5.2.2 1,120°C Solution-Treated and Aged Microstructure

The heat-treated samples were observed optically, and by SEM and TEM following the hardness measurements. The micrographs are shown in Figures 19 and 20. Figure 19(a) is an optical micrograph of an underaged sample(8 hrs. aging) with a grain size of approximately 700μms. Figure19(b) is the SEM micrograph of the same sample showing discrete grain boundary $M_{23}C_6$ carbides and matrix MC carbides, as established by the phase analysis section presented in section 4.7. Figure 19(c) is the dark field TEM image of the same sample showing a bimodal distribution of cuboidal primary and spheroidal secondary γ' precipitates, also established by the phase analysis presented in

section 4.7. The optical, SEM and TEM dark field micrographs of the samples in the peak aged condition (aged for 24 hrs.) showed similar features as compared to the underaged sample. The SEM micrograph examination, however, revealed the presence of a greater amount of discrete grain boundary $M_{23}C_6$ carbides.

Figure 20(a) illustrates the SEM microstructure of an overaged sample (72 hrs. aging). The microstructure comprises of a few primary MC carbides, $M_{23}C_6$ carbide particles along the grain boundaries, and local γ'-γ eutectic islands, as marked on the figure. These microstructural features were identified using SEM EDX-ray analysis and TEM analysis detailed in the phase analysis section, 4.7. The distribution of grain boundary $M_{23}C_6$ carbides changes from a discrete network for an underaged sample (Figure 19b) to a continuous one as observed in figure 20a. Also noticeable is the reduced size of primary MC carbides due to their dissociation, as explained in a later section, and the presence of eutectic islands. Figure 20(b) shows the microstructure of highly overaged sample (168 hrs.). The grain-boundaries contain well linked secondary carbide precipitates. The grain interior shows a complete disintegration of primary carbides into smaller MC carbide particles (confirmed by SEM analysis, and discussed later). These finer MC carbides then followed the usual dissociation reaction to generate fine $M_{23}C_6$ carbide particles in the grain interior. A TEM dark field image of the overaged sample containing coarser γ' precipitates is shown in Figure 25(a) in the phase analysis section. The bimodal distribution of γ' precipitates continued to exist with increased sizes of cuboidal primary and spheroidal secondary γ' precipitates.

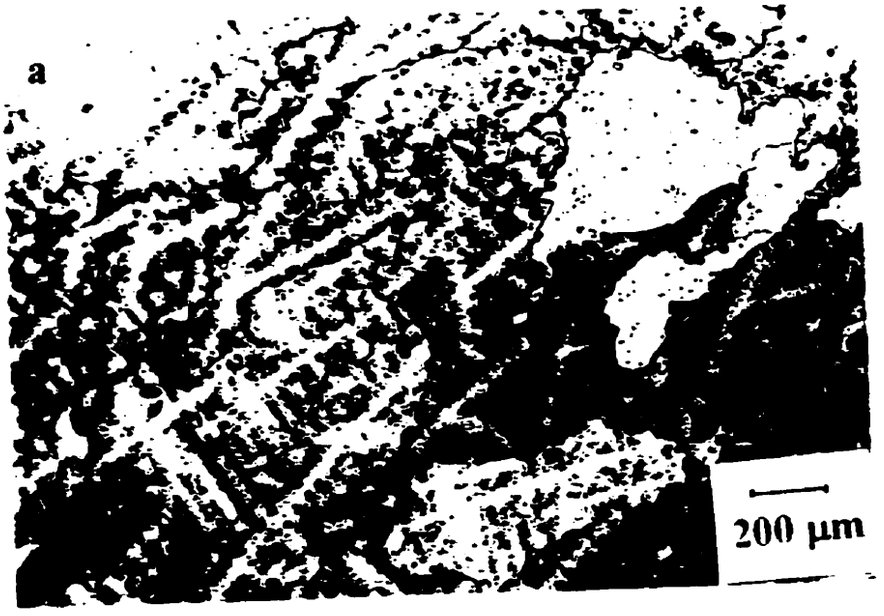

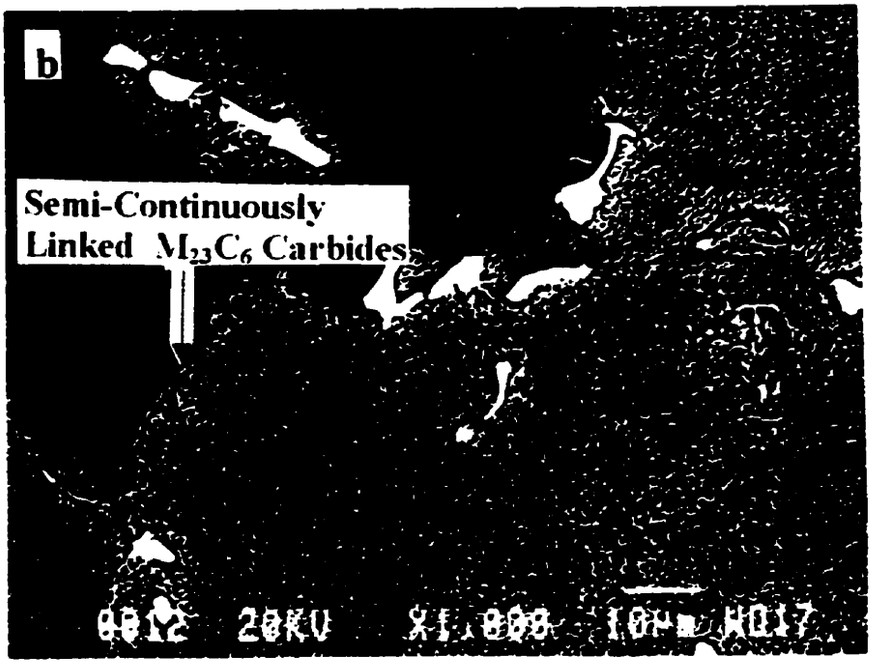

Figure 19 (continued)

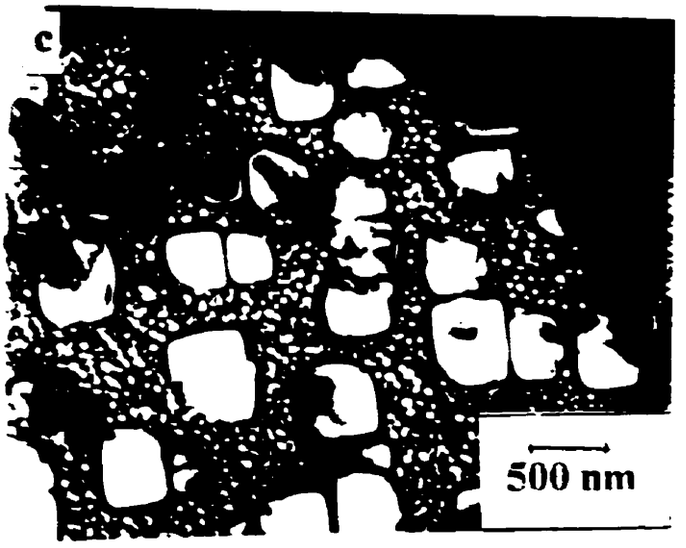

Figure 19: (a) an optical micrograph of an underaged sample with a grain size of approximately 700μms following a solution treatment of 1120^{0}C,50X(b) SEM micrograph of an underaged sample showing discrete grain boundary $M_{23}C_6$ carbides,50X, (c) TEM dark field image from an underaged sample showing a bimodal distribution of cuboidal primary and spheroidal secondary γ' precipitates.

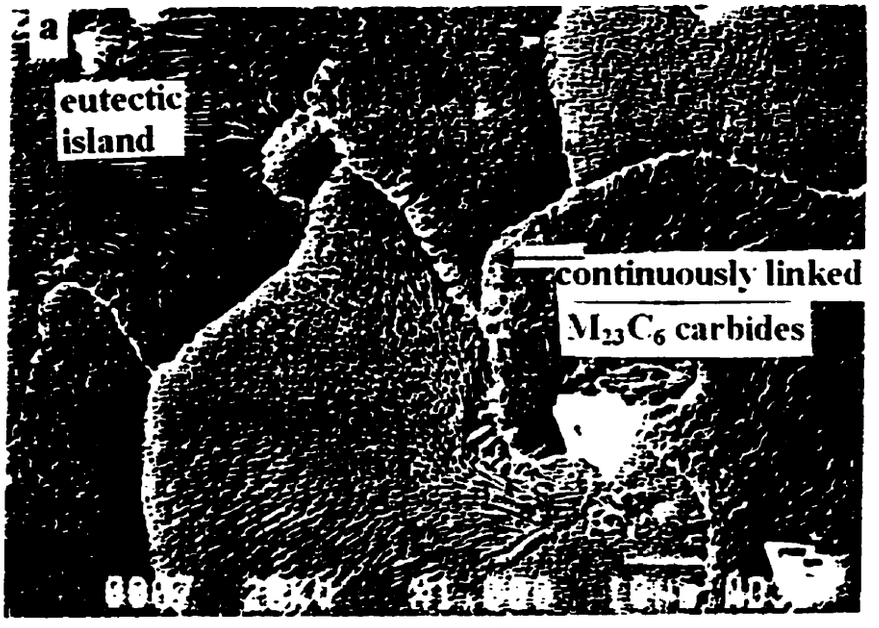

Figure 20 (Continued)

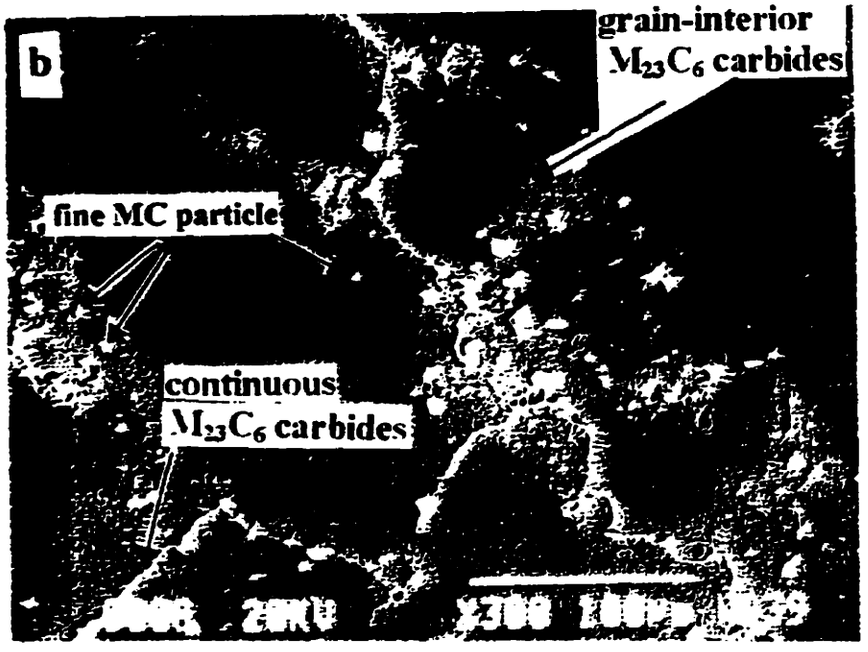

Figure 20 :(a) SEM micrograph of an overaged sample showing continuous grain boundary $M_{23}C_6$ carbides, (b) SEM micrograph of an highly overaged sample (168hrs.) showing $M_{23}C_6$ carbide particles on the boundaries and the grain-interior.

4.5.2.3. 1175^{0}C Solution-Treatment and Aging

A higher solution-treatment temperature(STT) of 1175^{0}C took more of primary γ' into solution than the 1,120°C STT (the results are presented in the volume fraction measurement section 4.9). The size of the primary γ' particles also got reduced due to their dissolution (Table 9), and resulted in a shape change of primary cuboidal γ' particles to degenerate γ' particles as seen in figure 21c. Figure 21(a) is a micrograph of an underaged sample(10 minutes aging) showing reduced coring due to compositional

homogenization , when compared to figure 19(a). The SEM. micrograph in figure 21(b) shows the presence of very few grain boundary $M_{23}C_6$ carbide particles and some coarse matrix MC carbides. Figure 21(c) is a TEM dark field image showing a bimodal distribution of degenerate primary γ' and very fine spheroidal secondary γ' precipitates. These precipitates were systematically characterized and identified. The phase analysis is presented in section 4.7.

The peak aged sample(2 hrs. aging) showed a similar microstructure except for the increased size of γ' precipitates. In the overaged sample(72 hrs. aging), the grain boundaries delineated linking of $M_{23}C_6$ carbide particles to produce a continuous network, similar to that observed in figure 20. The γ' precipitate distribution appeared to be degenerate and coarse, as shown in the TEM dark field image of the sample shown in figure 22.

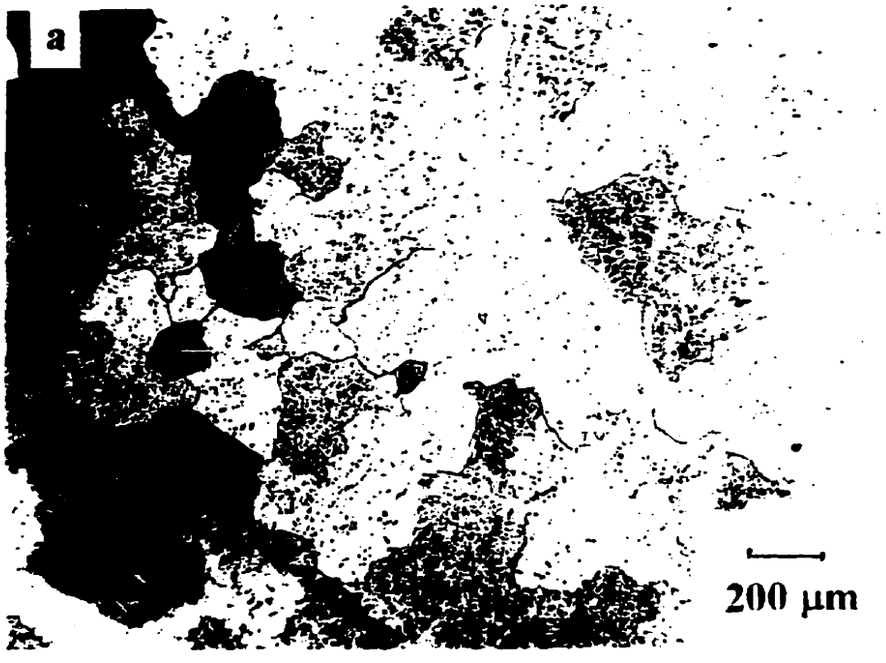

Figure 21 (continued)

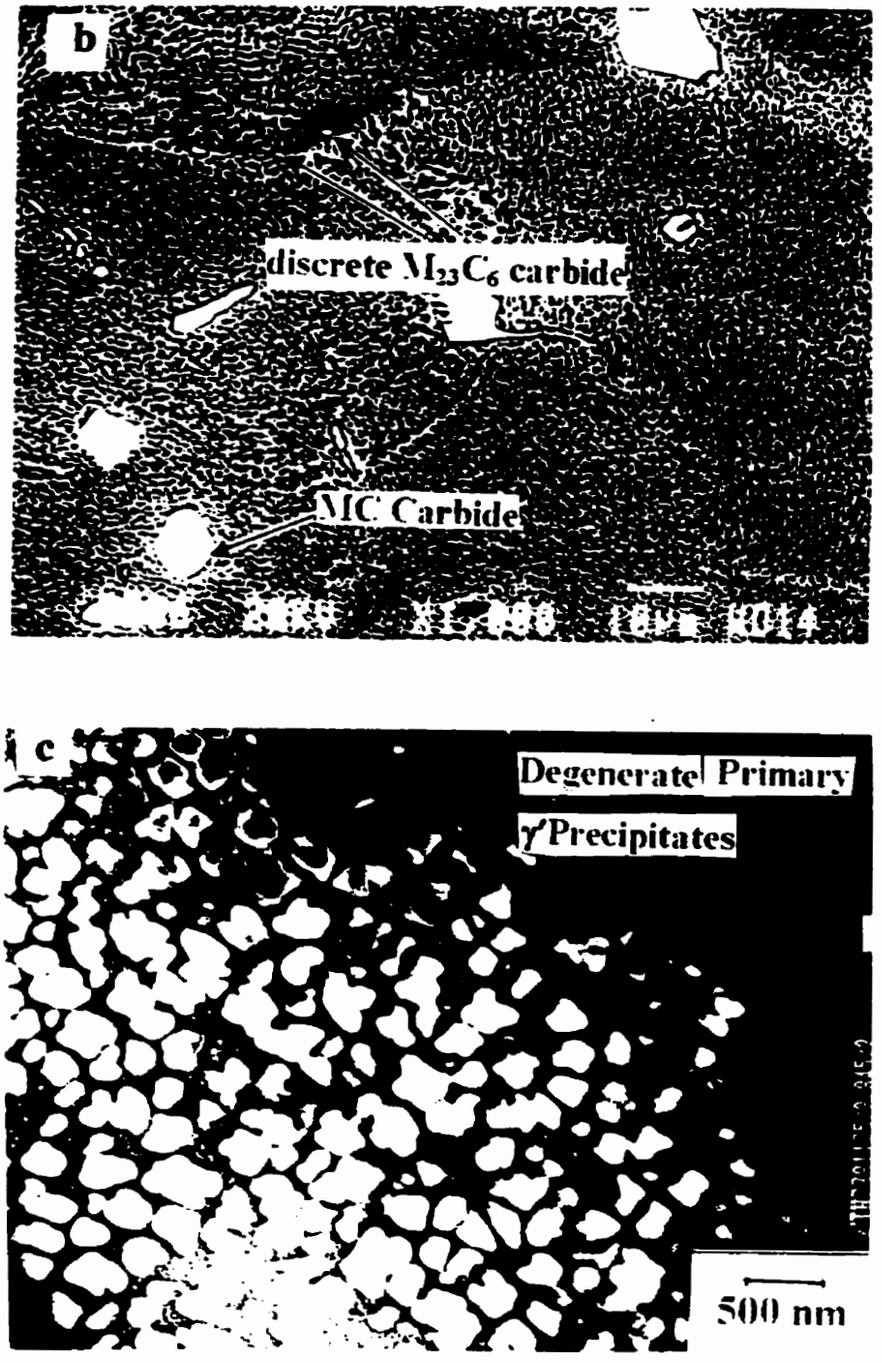

Figure 21: (a) Optical micrograph of an underaged sample following 1175^{0}C solution treatment(10 minutes aging) showing reduced coring,50X, (b) SEM micrograph showing the presence of very few grain boundary $M_{23}C_6$ carbides and some coarse matrix MC carbides, (c) TEM dark field image showing a bimodal

distribution of degenerate primary γ' and very fine spheroidal secondary γ' precipitates.

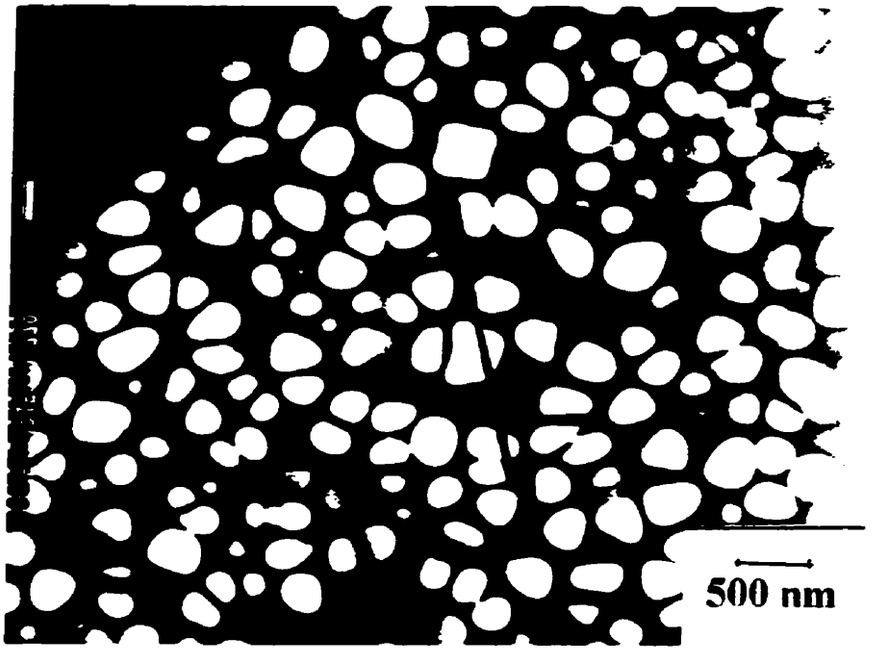

Figure 22 TEM dark field image showing a unimodal distribution of coarse, degenerate γ' particles of an overaged sample solution-treated at 1175^{0}C.

4.5.2.4 1225^{0}C Solution-Treatment and Aging

As reported in the previous section, the 1225^{0}C solution-treatment (2 hours)also did not completely dissolve the primary γ' precipitates. The grain size increased from 700μm to about 900μm. The γ' precipitate distribution appeared to be unimodal, degenerated, and finer (Table 9) in the underaged sample as seen in the TEM dark field image of figure 23. Overaging, following a 1225^{0}C solution treatment, resulted in modifying the γ' precipitate morphology which changed from a degenerate distribution to near spherical as observed in Figure 24.

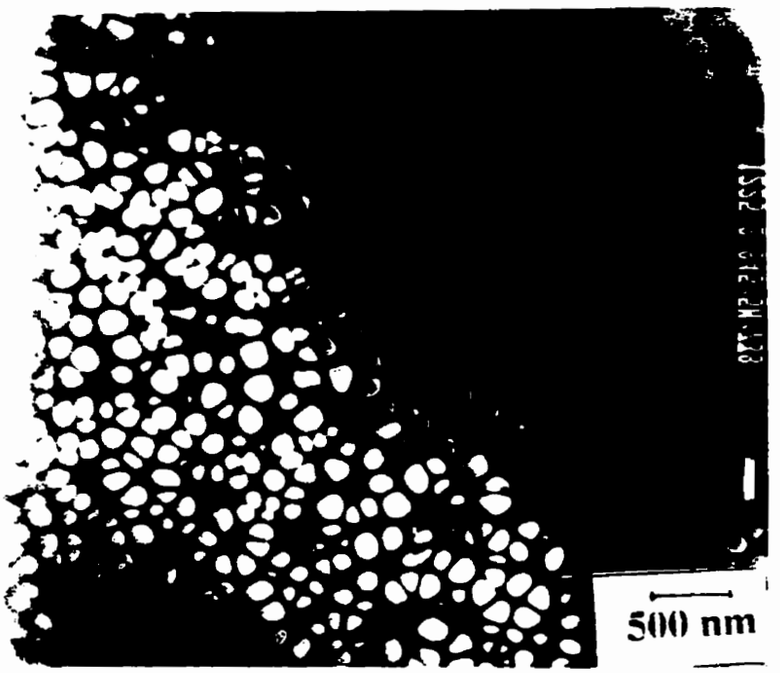

Figure 23 TEM dark field image showing finer unimodal degenerate γ' distribution in an underaged sample solution-treated at 1225°C.

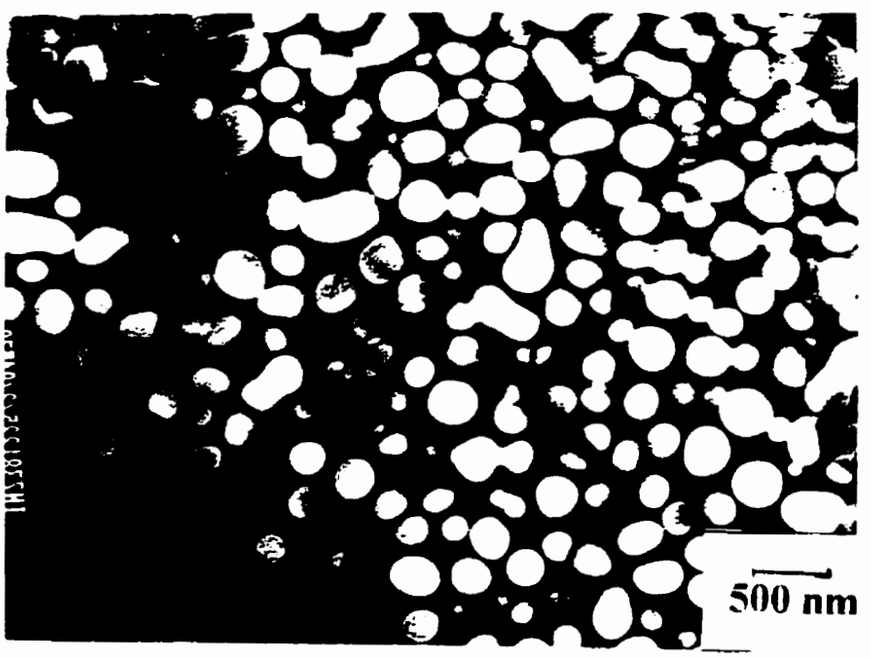

Figure 24 TEM dark field image showing coarse, unimodal, and near spherical γ' distribution in an overaged sample solution-treated at 1225°C.

4.6 Phase Analysis of Precipitates and Microstructures

4.6.1 γ' Particles

Figure 25(a) is a dark field electron micrograph taken with the aid of (001) γ' superlattice reflection to eliminate contrast effects due to coherency strains in the matrix, and is superimposed with the selected area diffraction pattern from the same region. The figure shows a bimodal distribution of γ' precipitates in a sample aged for 72 hours at 845°C after solution-treating at 1,120°C for two hours. The SADP, along the [001] beam direction, shows the primary matrix spots and the secondary γ' superlattice reflections. The lattice constant of γ' precipitates calculated from the diffraction pattern was about 3.59Å, and is close to lattice constant of γ' precipitates[19]. Figure 25(b) show the convergent beam electron diffraction (CBED) pattern from γ' particles along [001] beam direction. A four fold symmetry represents a face-centered-cubic structure for the γ' particles. Figure 25(c) shows the TEM image of an extraction replica from a region containing purely secondary spheroidal γ' particles from a sample aged for seventy two hours following the same solution-treatment. This figure shows the spherical morphology of secondary γ' particles.

The size of the primary cuboidal γ' was in the range 350-500 nm (mean cubic edge length) and that of the secondary spheroidal γ' (diameter) was in the range of 50-

120 nm. That is, the γ' particles had a bimodal distribution. The volume fraction of γ' phase in a fully heat-treated sample was measured to be in the range of 40-45%.

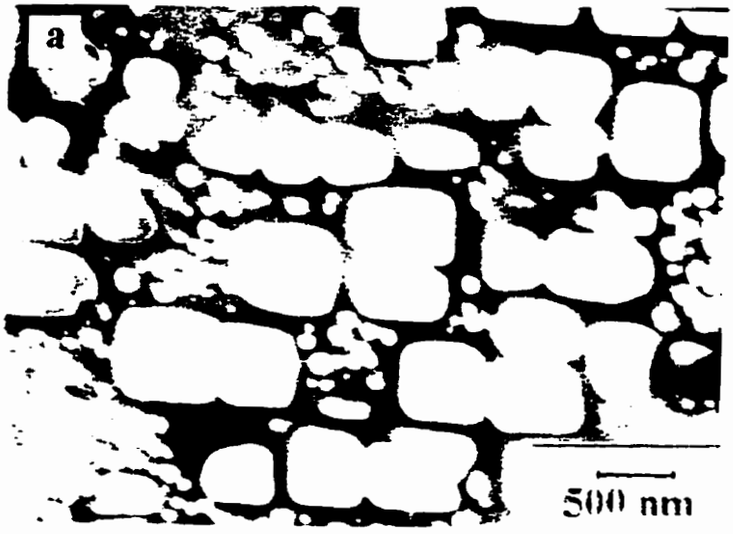

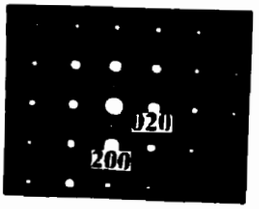

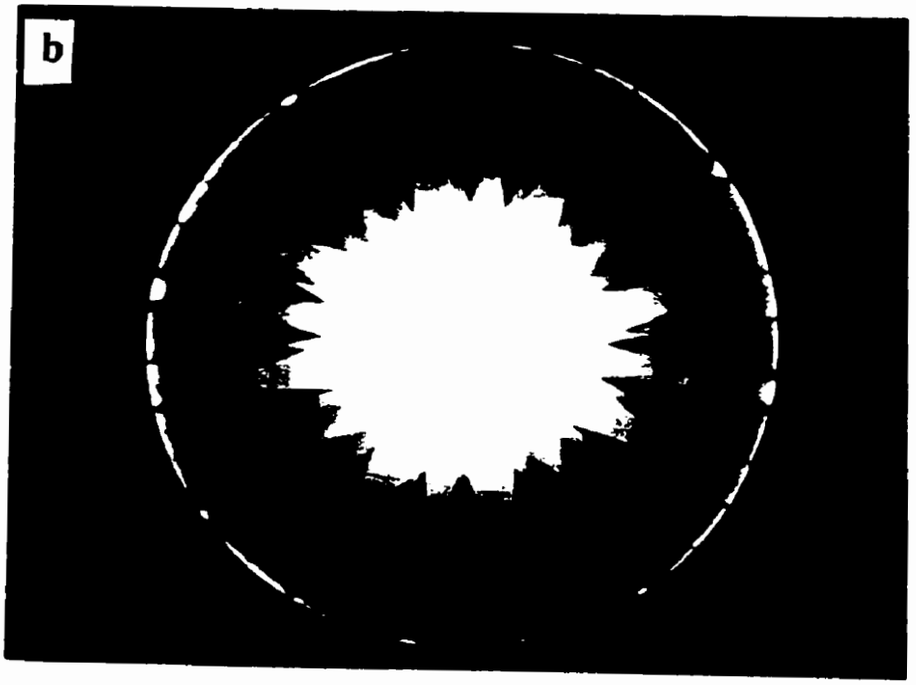

Figure 25 (continued)

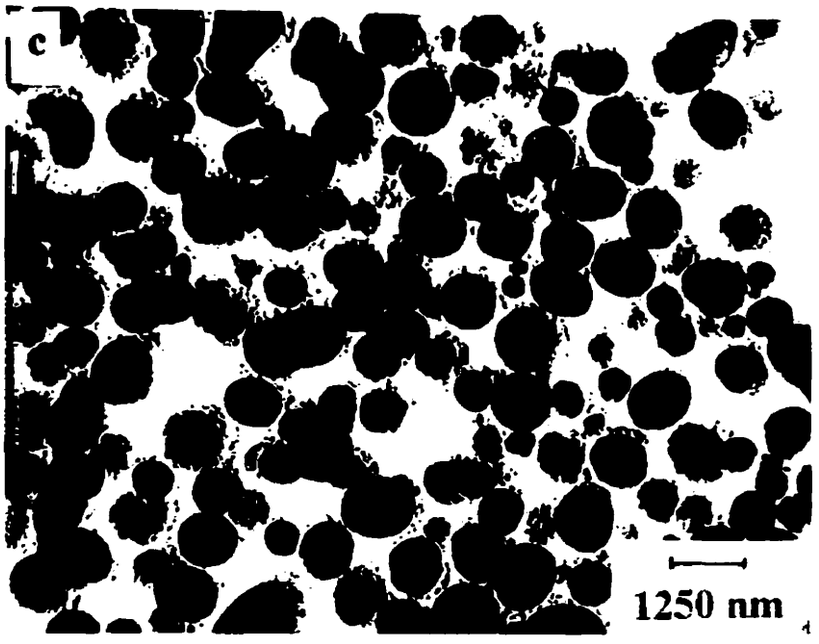

Figure 25: (a) TEM bright field micrograph showing primary γ' from an overaged sample following 1120^{0}C solution treatment, (b) CBED from γ' precipitates along the [001] zone axis, (c) TEM bright field replica image showing secondary γ' from an overaged sample following 1120^{0}C solution treatment.

4.6.2 MC Carbides

The primary MC carbides occur in various morphologies and sizes which depend on the melting and casting practice, as shown in Figure 26(a). Figures 26(b) and (c) show a TEM bright field image along a [001] zone axis of a primary carbide on a grain boundary and the SADP from the carbide particle respectively. The analysis of the SADP (Figure 26c) suggests it to be MC type carbide with an FCC structure. The CBED of the precipitate was similar to one obtained in figure 25(b) confirming that this is an FCC

phase. The composition of this primary carbide phase as determined by EDS spectrum is given in Table 7. The EDS spectrum is shown in Figure 27(b).

Figure 27(a) shows a primary MC carbide in the back scattered image. The comparative EDS spectra for the carbide bulk and center is shown in figure 27 (b) and (c). MC appears to be a tantalum, niobium, and titanium based carbide. The center of the carbide has a different composition than the bulk, and is extremely rich in titanium and aluminum and relatively poor in heavy elements like niobium, tantalum and tungsten, as compared to the average bulk composition of the carbide. The composition of carbide center is given in Table 7.

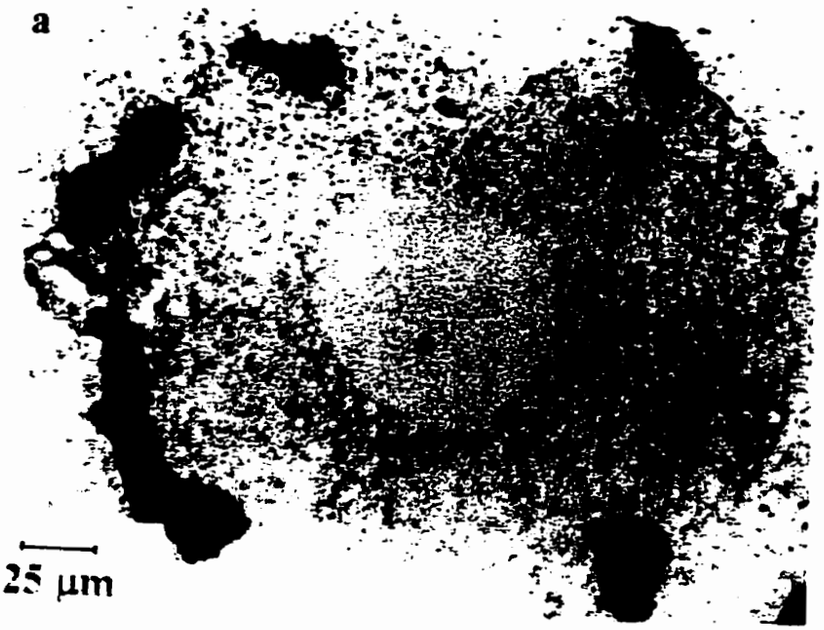

Figure26 (continued)

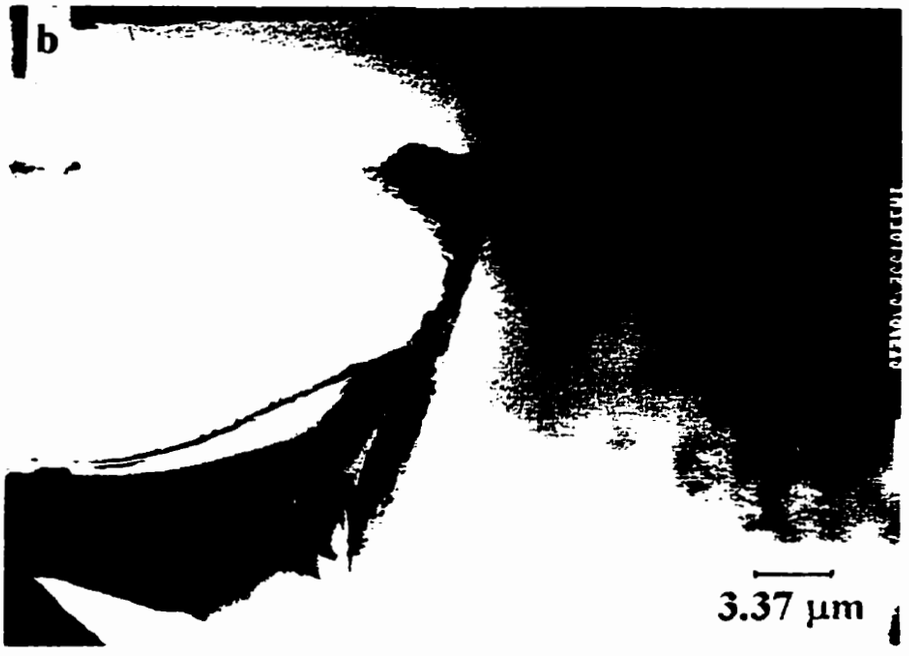

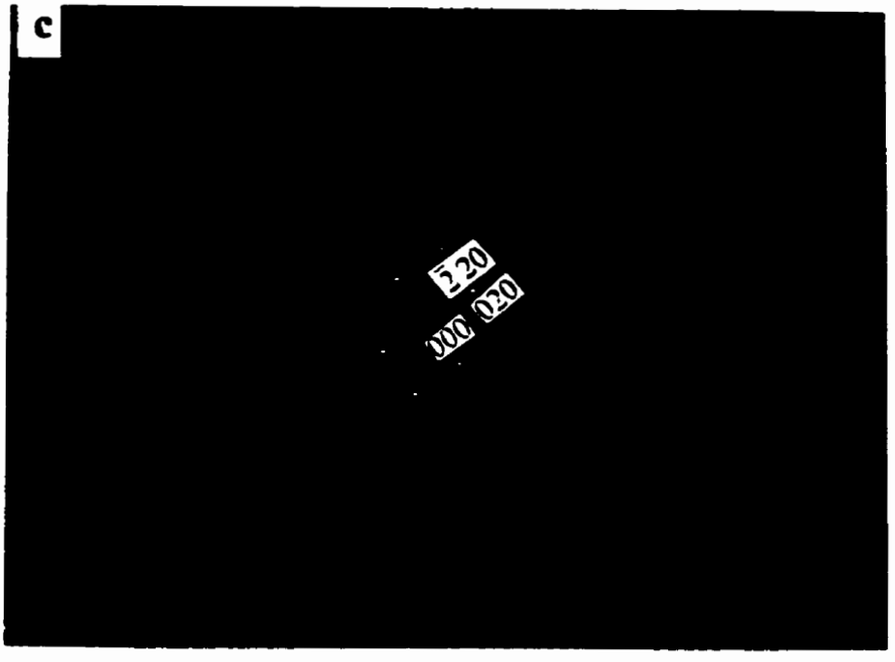

Figure 26: (a) Optical micrograph from as received cast IN738 showing primary MC carbides in various morphologies, 400X (b)TEM bright field image of grain boundary MC carbide, (c) SADP from a primary MC carbide along [001] beam

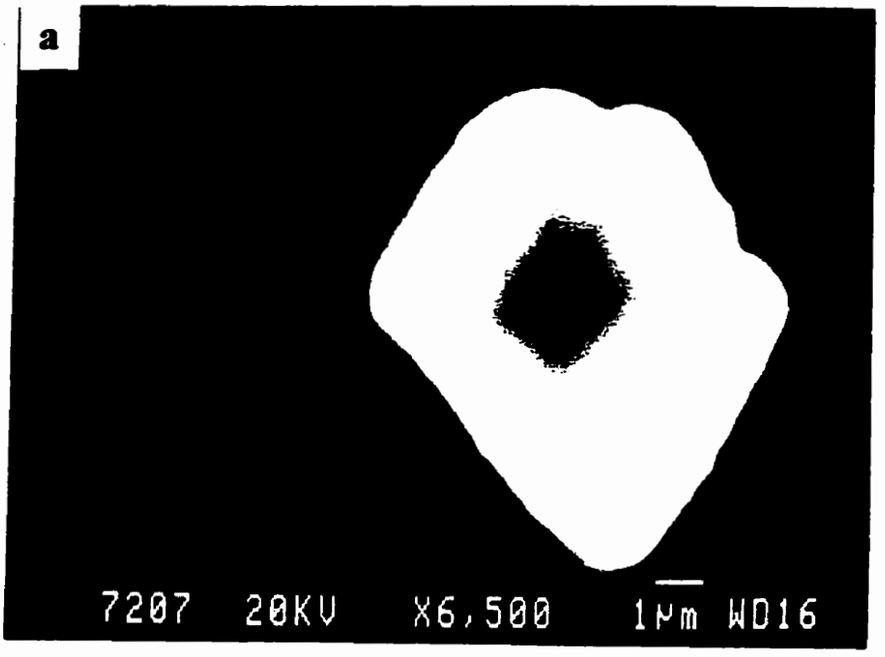

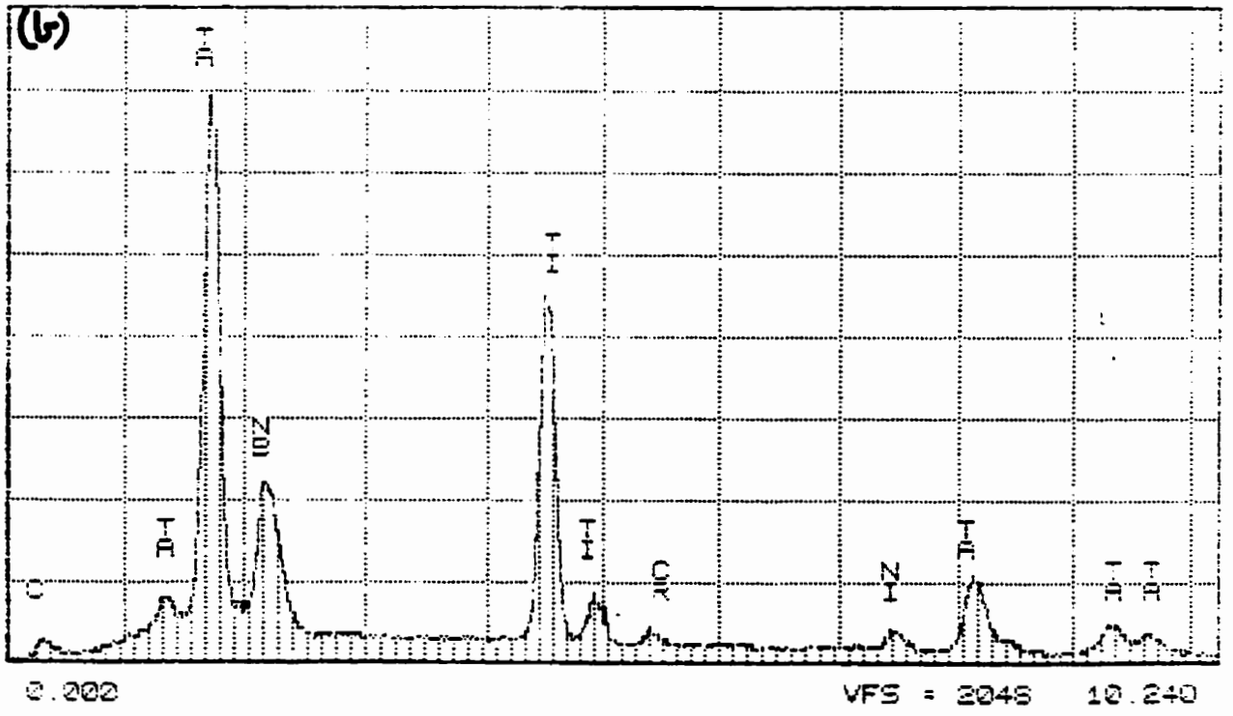

direction.

Figure 27 (continued)

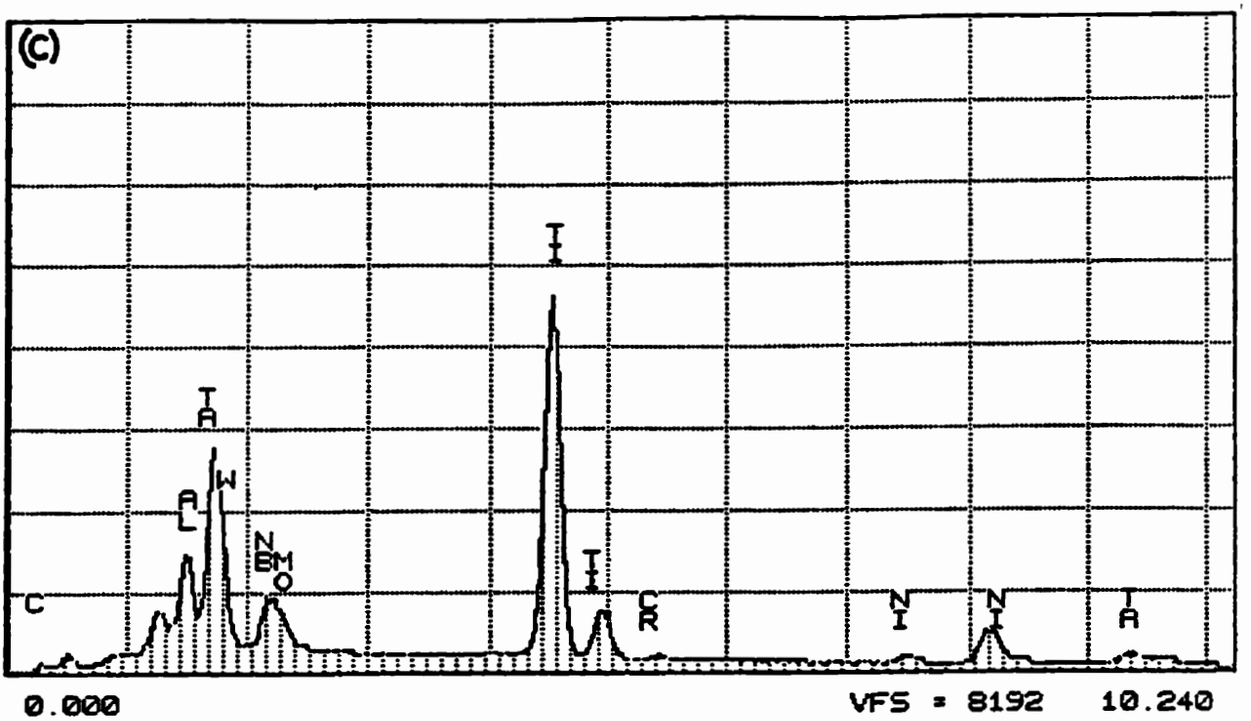

Figure 27: (a) SEM micrograph showing a back scattered image of a primary MC carbide, (b) EDS spectrum from an MC carbide particle bulk, (c) EDS spectrum from an MC carbide particle center.

Table 7:Composition of MC Carbides determined by Micro-Q EDX-Ray analysis

Composition (wt%)	Ti	Cr	Co	Ni	Al	Mo	W	Ta	Nb
MC (average)	25.11	0.87	0.21	2.49	0.12	2.27	7.50	44.22	17.21
MC (center, Figure 27(a))	42.14	1.10	0.22	2.26	6.83	1.87	5.99	31.21	8.39

4.6.3 $M_{23}C_6$ Carbides

MC carbide is not a very stable phase in IN-738 and it dissociates with time at the aging temperature of 845°C to form fine $M_{23}C_6$ debris around it[12,42]. This process occurs within the grains and along the grain boundaries as shown in Figure 28(a) and (b). The following mechanism has been proposed[42]:

$$MC + \gamma \rightarrow M_{23}C_6 + \gamma' \text{ (fine)}$$

Figure 28(a) shows MC carbide particle that has transformed into $M_{23}C_6$, with the $M_{23}C_6$ precipitates all along the periphery of the special grain. The analysis of the particles observed in the figure 28a is described later in this section. The original MC carbide particle was located at the center of the grain. Carbon from the primary carbides could have diffused out in all directions and picked up suitable elements to form $M_{23}C_6$, with a fine tertiary γ' on its outer side. Figure 28(b) shows a couple of partially dissociated grain boundary MC carbides in a peak aged sample . The carbide particles in the grain interior appeared to have remained unchanged. Figure 29 is a carbon extraction replica showing a completely dissociated primary carbide particle. This micrograph demonstrates that the above mentioned reaction scheme for the dissociation of MC carbide is operative in this alloy. A dense precipitation of secondary γ' spherical particles and an impression of a continuous $M_{23}C_6$ carbide film along the periphery of the already dissociated MC carbide particle can be observed.

The composition of MC and $M_{23}C_6$ carbides computed by EDS using the micro-Q

program is given in Table 8 and the EDS spectrum obtained from the fine grain boundary particles is shown in Figure 30(a). The particles are chromium, molybdenum, and tungsten rich carbides. Figure 30(b) is a carbon extraction replica showing $M_{23}C_6$ carbide particles present in the grain interior. The carbon extraction replica image of figure 30(c & d) shows $M_{23}C_6$ carbide particles along the grain boundary as discrete particles and as linked particles, respectively. The SADP from these particles, along the [001], [011], and [$\bar{1}$11] beam direction are shown in figures 31(a, b, and c). The analysis suggested these particles to be $M_{23}C_6$ carbides.

Figure 28 (Continued)

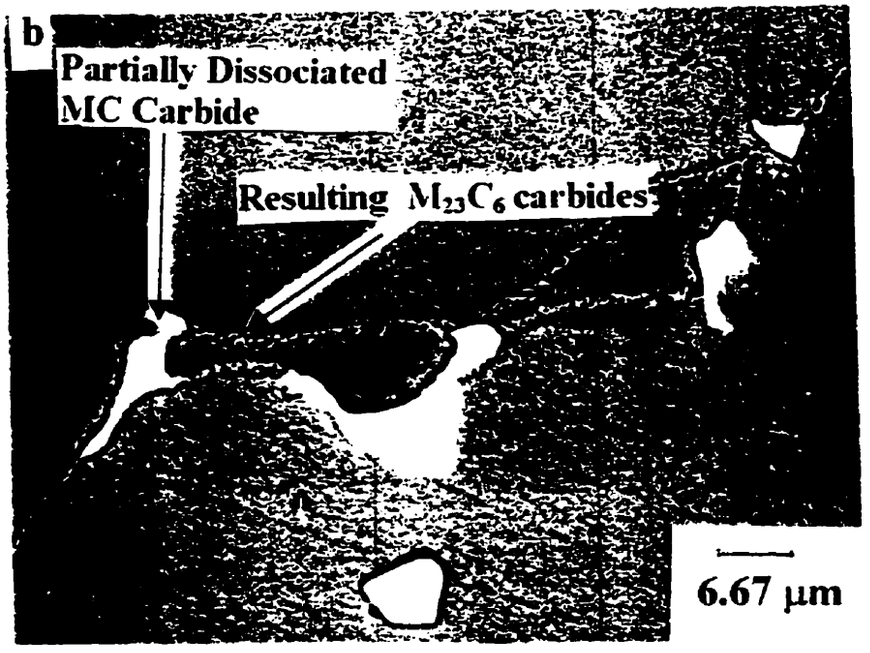

Figure 28:(a) Optical micrograph of an overaged sample 1) showing partially dissociated matrix primary carbide, 2)completely dissociated primary MC carbide, into $M_{23}C_6$ carbide particles along its periphery, as identified in the figure, 200X, (b) SEM micrograph of a peak aged sample showing partial dissociation of grain boundary primary MC carbides into $M_{23}C_6$ carbide particles along the grain boundary, 1500X.

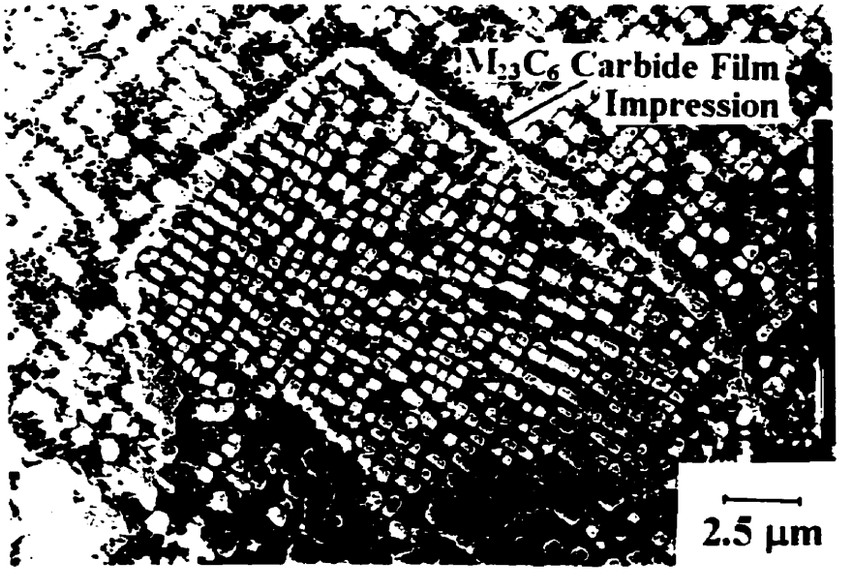

Figure 29 Carbon extraction replica of an overaged sample after solution treatment at 1120°C showing a fully dissociated primary MC carbide.

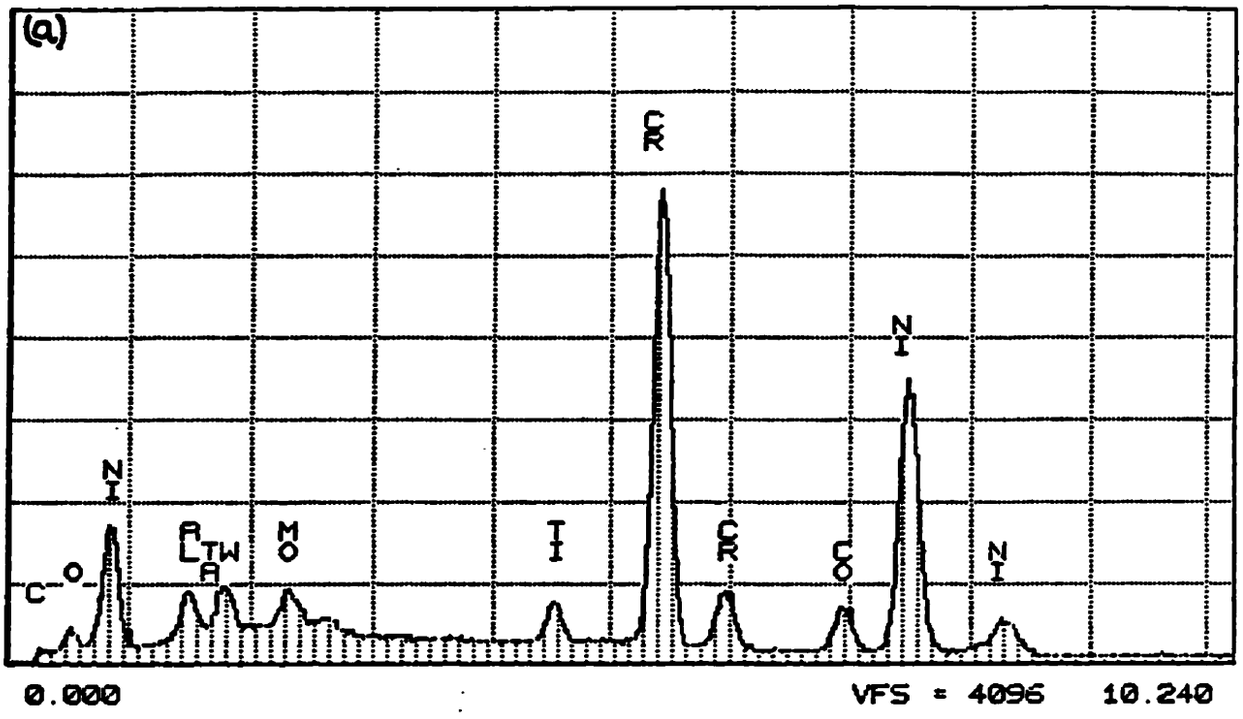

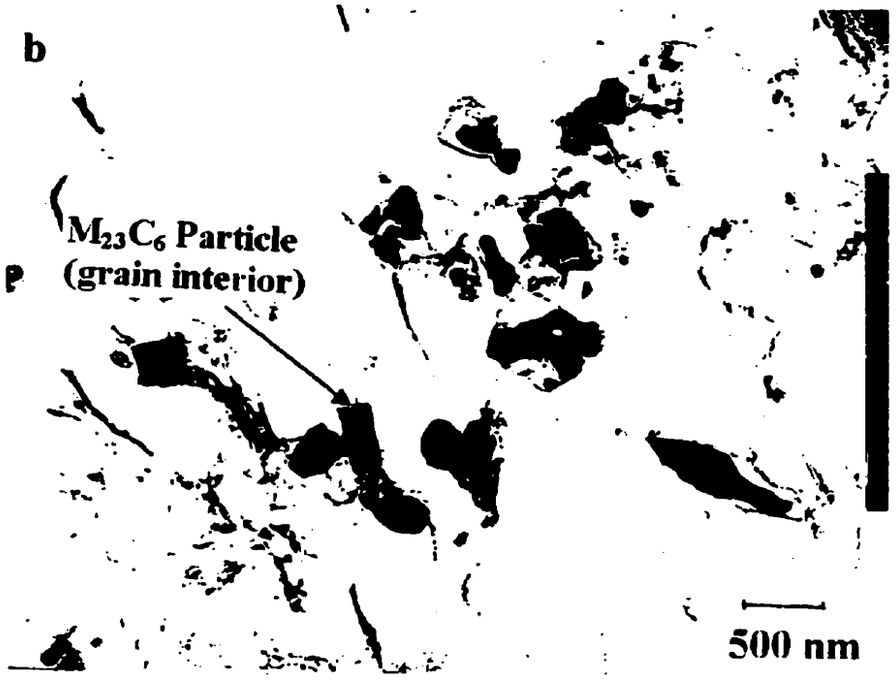

Figure 30 (continued)

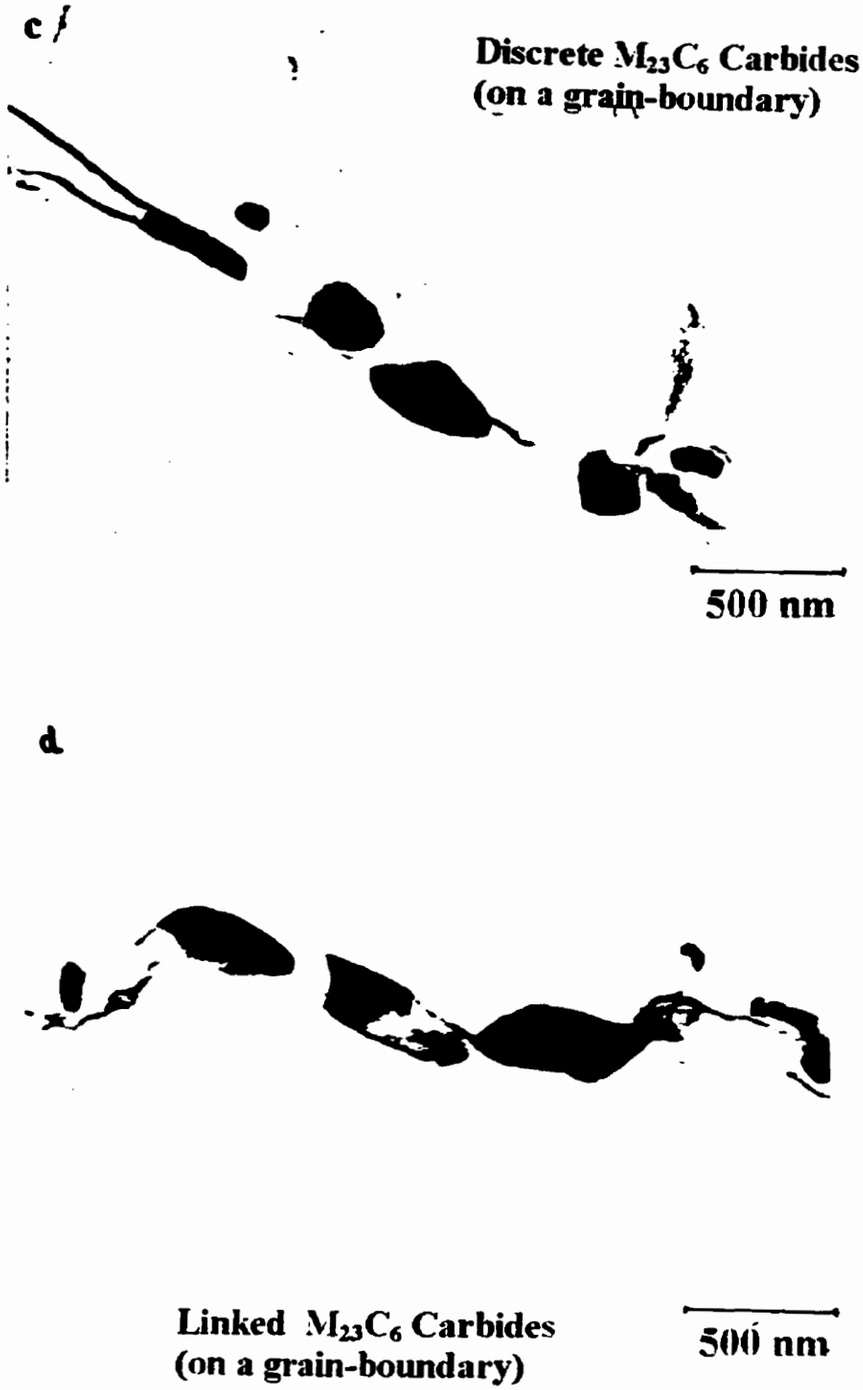

Figure 30: (a) EDS spectrum from fine grain boundary particles; carbon extraction replica showing $M_{23}C_6$ carbide particles (b) present in the grain interior, (c) along the grain boundary as discrete particles, and(d) along the grain boundary as linked particles.

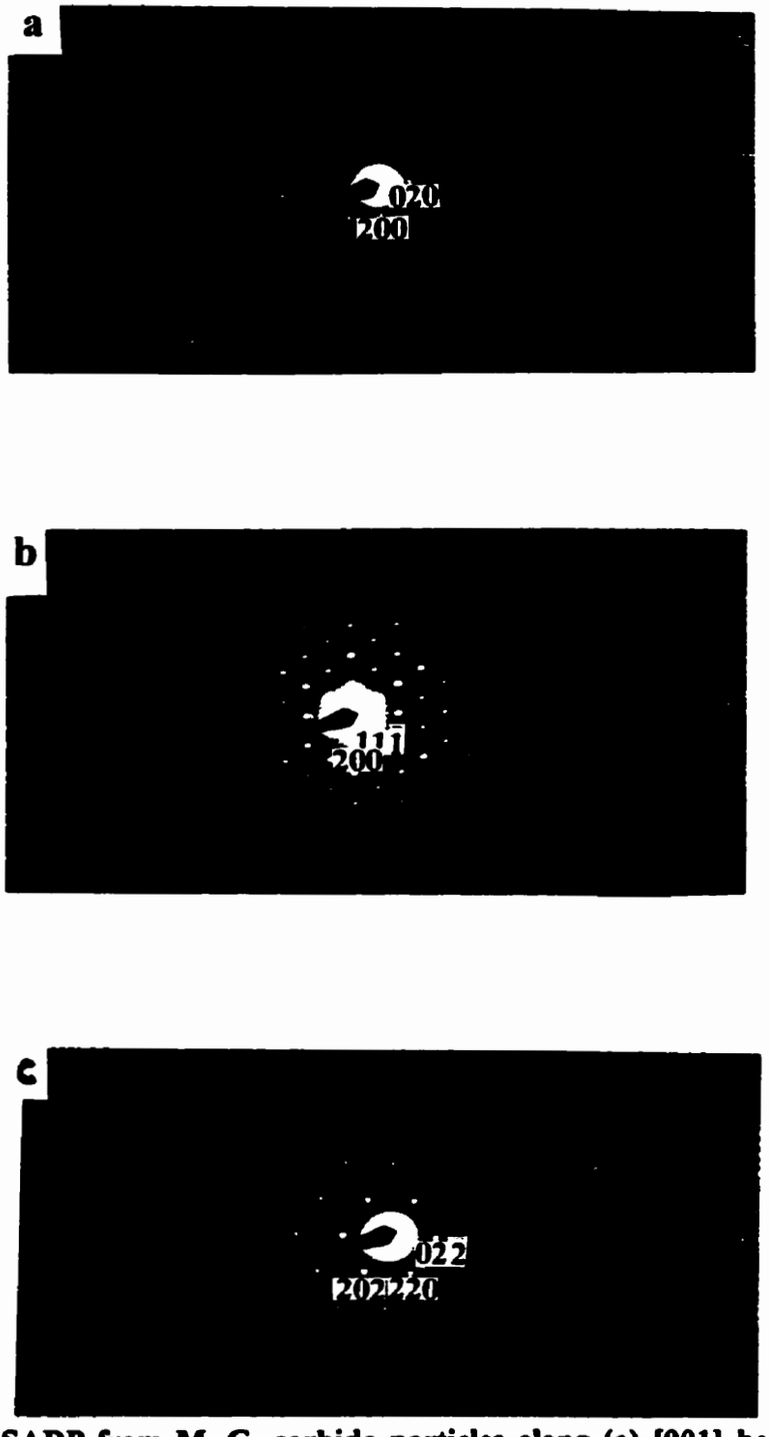

Figure 31 SADP from $M_{23}C_6$ carbide particles along (a) [001] beam direction, (b) [011] beam direction, (c) $[\bar{1}11]$ beam direction.

Table8 :Composition of $M_{23}C_6$ carbide particles using micro-Q EDX analysis.

Composition (wt%)	Ti	Cr	Fe	Co	Ni	Mo	W	Nb
$M_{23}C_6$	1.60	57.93	2.10	6.99	0.33	17.95	10.61	0.78	1.69

4.6.4 Heterogeneous Eutectic Islands

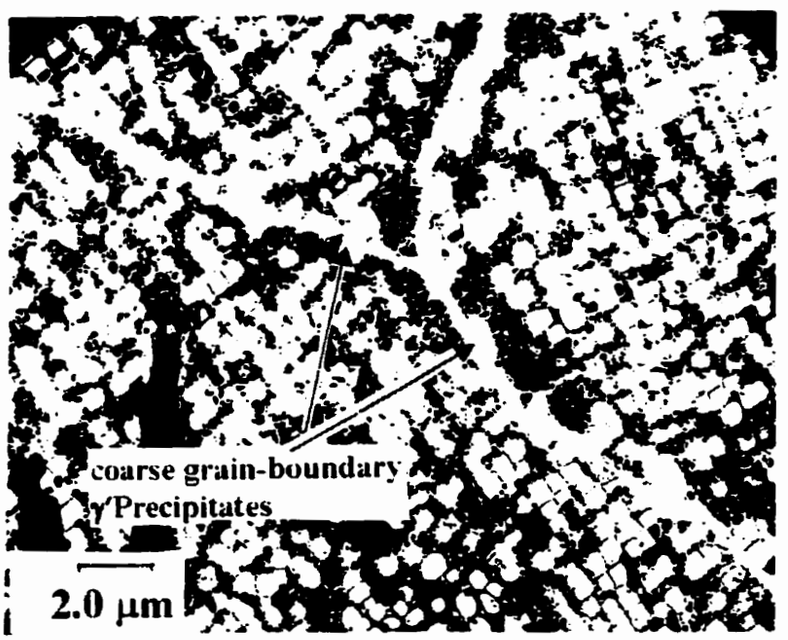

Figure 32 TEM extraction Replica showing a general heterogeneous microstructure of an overaged sample.

Figure 32 reveals the microstructural inhomogeneity that persisted in an overaged sample after solution treatment at 1120^0C. The extraction replica contained secondary γ' precipitates, and some scattered primary and grain boundary γ' particles, which were identified by carrying out a phase analysis. The replica contained impressions from the near-square primary γ' precipitates and grain boundary $M_{23}C_6$ carbide film. The secondary γ' precipitates are seen to be concentrated all along the grain boundaries. The impressions of coarse grain boundary γ' particles and a continuous grain boundary $M_{23}C_6$ carbide film should also be noted. Figure 33(a-d) shows the presence of heterogeneous eutectic islands containing randomly oriented γ' precipitates in various morphologies even after over-aging (1120^0C/2 hrs.(A.C.)/845^0C/72 hrs. A.C.). These microstructures are likely to deform heterogeneously as compared to the matrix when subjected to service stress.

Figure 33(a) shows an eutectic island boundary containing elongated primary γ' particles. The island contains an uneven distribution of spheroidal secondary γ' particles. Figure 33(b) shows another eutectic island boundary pinning elongated primary γ' particles on the outside. The interior of the eutectic island consists of alternate layers of primary and secondary γ' particles. Figure 33(c) shows tear drop shaped primary γ' particles contained within the eutectic island. Figure 33(d) shows eutectic islands containing stair shaped primary γ' particles.

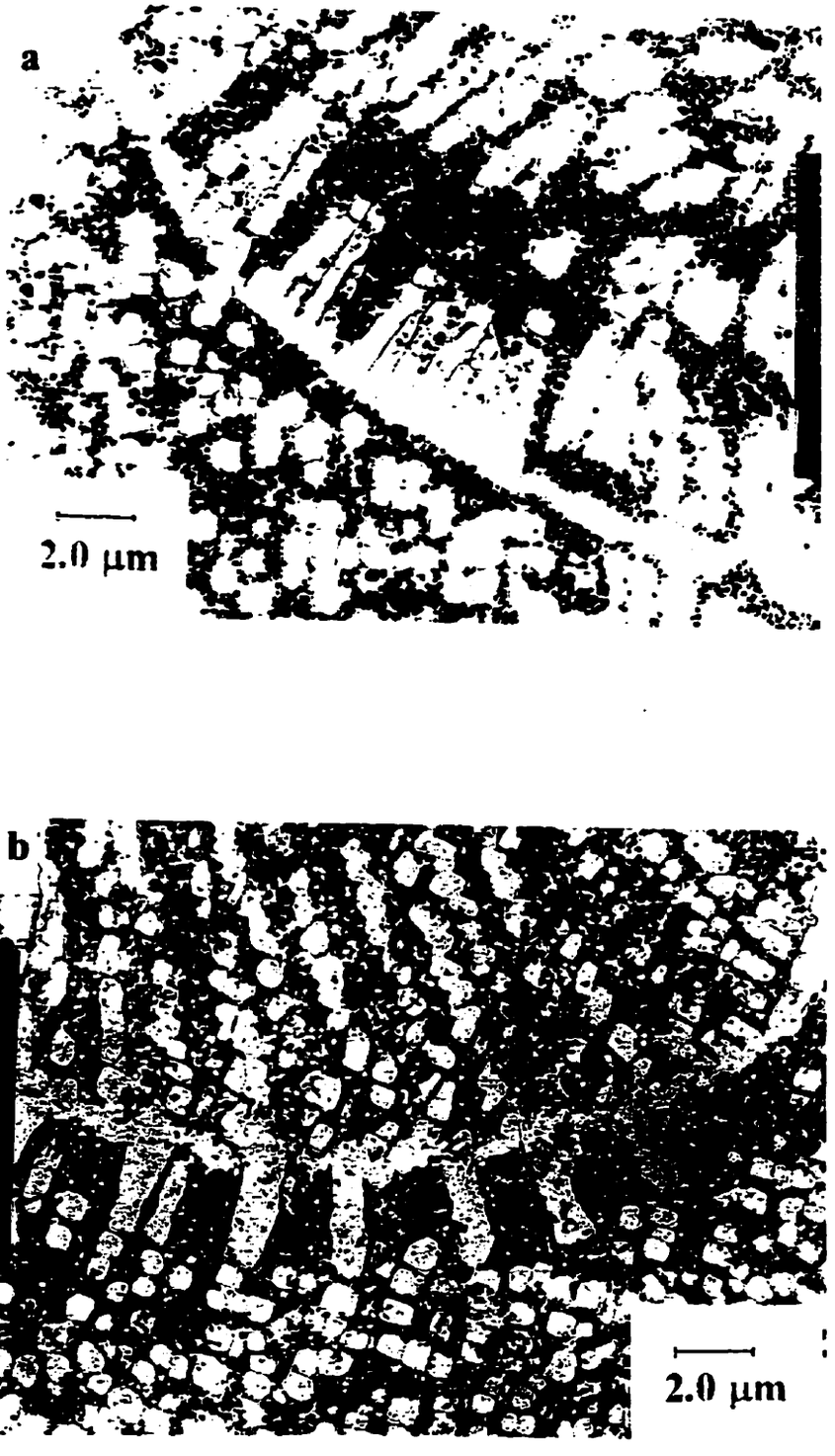

Figure 33 (continued)

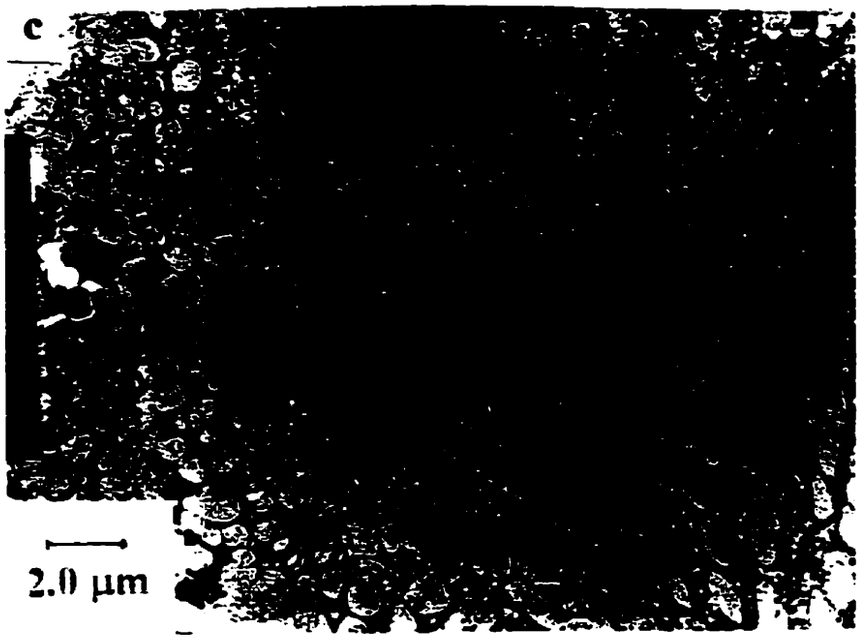

Figure 33:(a) TEM replica showing eutectic island boundary containing elongated primary γ' particles, (b) TEM replica showing eutectic island boundary pinning elongated primary γ' particles that are on the outside, (c) TEM replica showing

showing eutectic island containing stair shaped primary γ' particles.

4.6.5 Grain Boundaries

In cast IN-738, the grain boundary area per unit volume is small owing to its large grain size (running from hundreds of microns to mm's). The boundaries still play a crucial role in the deformation process because the fracture mode in IN738 is intergranular. Fracture in service at high temperature is via nucleation, growth and coalescence of grain-boundary cavities forming intergranular cracks that ultimately lead to fracture [22]. The standard heat-treatment produces straight grain boundaries, whereas it should be possible to produce serrated grain boundary structures which would be able to accommodate more strains(deform to a greater extent), such as welding strains. To evaluate this a sample was heated to 1,200°C and then cooled to 1,090°C at a rate of 1°C/minute and then water-quenched. Water-quenching restricted the precipitation of $M_{23}C_6$ carbides along the grain-boundaries. Figure 34(a) shows grain boundary serrations formed due to either migration of grain boundary segments between the coarse grain-boundary γ' particles or due to the movement of these coarse γ' particles, in order to accommodate coherency strains, against a stationary linear grain boundary locally generating serrations[26,40]. Another sample was prepared using a similar heat treatment procedure, the only difference was that the sample was cooled at 1°C/minute to 950°C instead and then water-quenched. The precipitation of continuous fine $M_{23}C_6$ particles (solvus of 1025^0C) is seen to have enhanced the serrated nature of the grain boundary as shown in Figure 34(b).

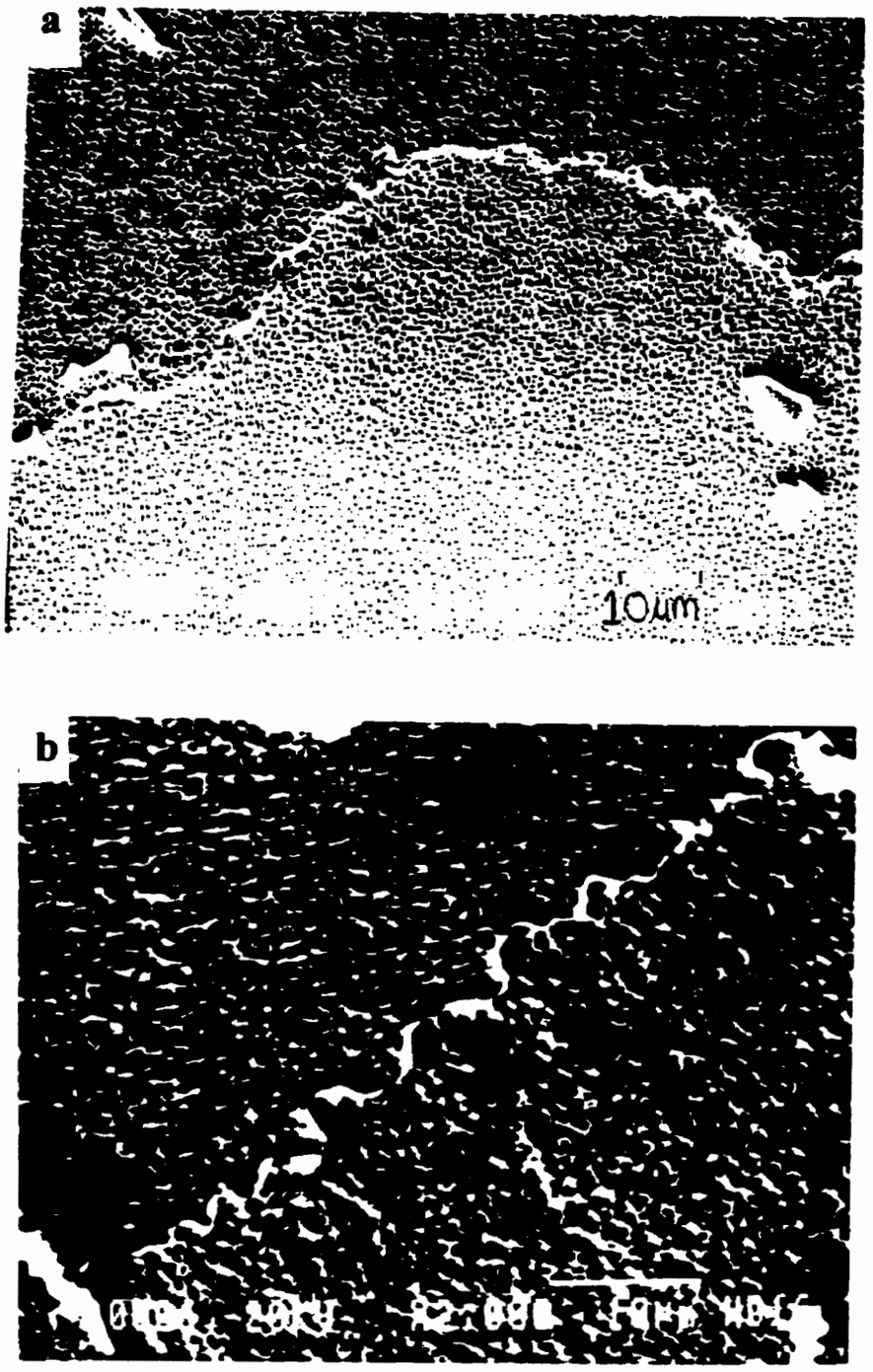

Figure 34: SEM Micrographs showing serrated grain boundaries in a sample furnace cooled (a) to 1090^{0}C and water quenched, (b) to 950^{0}C and water quenched.

4.7 γ' Particle Size Distribution as a Function of Heat-Treatment

Table 9 lists variation in the size of primary and secondary γ' particles in all the heat-treatments attempted. These particle sizes have been measured from the dark field TEM negatives by an optical image analyzer using two micrographs from 2 different regions per sample. It is observed that a distinct bimodal distribution of γ' particles prevailed for 1120^{0}C STA only. The size of primary γ' increased by only 35% after 72 hours of aging as compared to at least 100% increase for the secondary γ' particles. The average size of primary and secondary γ' particles for the standard heat treated sample was about 425nm and 96nm respectively. The 1175^{0}C STA samples mainly consisted of degenerated γ' particles with a very fine dispersion of secondary γ' particles. It was not possible to get accurate size measurements for these secondary γ' precipitates. The average γ' particle size increased from 184nm to 267nm over a 72 hour aging period. Solution treatment at the higher temperature of 1225^{0}C resulted in an increased dissolution of primary γ' particles and the average size after solution treatment was 102nmAgain, it was not possible to measure the secondary γ' precipitates size in this case.

The underaged and peak aged samples showed a small area fraction of secondary γ' particles suggesting a possible highly competitive growth between the secondary γ' particles. The successful precipitates eventually joined the primary γ' particles and grew together. Therefore the overaged specimens contained only unimodal distribution of γ' particles.

Table 9: Variation in γ' size with heat treatments

HEAT-TREATMENTS		γ' Primary Cuboids		γ' Secondary Spheroids	
No.	Heat-Treatment Schedule, time in hrs.	Range(nm)	Average Size(nm)	Range(nm)	Average Size(nm)
1	1120^0C/2/S.T.	300-419	347	---	---
2	1120^0C/2/845^0C/08	371-420	392	25-65	65
3	1120^0C/2/845^0C/12	375-456	412.5	52-115	87.5
4	1120^0C/2/845^0C/16	404-457	425	46-147	90
5	1120^0C/2/845^0C/24	381-500	425	32-162	96
6	1120^0C/2/845^0C/72	403-520	450	92-120	102
7	1120^0/2/845^0/120	404-620	482	82-145	112
8	1150^0C/2/S.T.	357-480	432	---	---
9	1175^0C/2/S.T.	184-236	184	---	---
10	1175^0C/2/845^0C/2	179-213	190	---	---
11	1175^0C/2/845^0C/12	130-229	210	---	---
12	1175^0C/2/845^0C/24	175-267	226	---	---
13	1175^0C/2/845^0C/72	222-318	267	---	---
14	1225^0C/2/S.T.	60-150	102	---	---
15	1225^0C/2/845^0C/2	76-145	110		
16	1225^0C/2/845^0C/12	104-129	135	---	---
17	1225^0C/2/845^0C/24	128-184	140	---	---
18	1225^0C/2/845^0C/72	133-248	178	---	---
19	AS RECD.	209-328	248	---	---
20	1200^0C/3-OQ/845C/24	81-132	108	---	---

S.T. = Solution Treated and Air Cooled, O.Q.= Oil -Quenched

It was difficult to measure secondary γ' size which was usually less than 50nm with any accuracy for 1175^0C and 1225^0C solution treated and aged samples. and is therefore not reported here.

4.8 Determination of Volume Fraction of γ' in the Matrix and the Lattice Constants of Various Phases.

The volume fraction of γ' precipitates was observed to remain virtually the same in the as received and in the standard heat-treated sample. The only difference was in the morphology and distribution of γ' particles. As received material contained degenerate cuboids with no secondary γ' spheroids whereas the standard heat-treated sample had 20-25% of its volume occupied by secondary γ' precipitates. This implied that 1,120°C solution-treatment dissolved only half of the primary γ' precipitates. With increasing solution-treatment temperatures, the volume fraction of γ' in the matrix continued to decrease as shown in Figure 35. It was difficult to measure the γ' volume fraction in the 1,225°C ST sample but the TEM micrograph showed the presence of a few primary particles. Thus it can be concluded that the solvus of γ' particles is well above 1,175°C, and not in the range of 1,160°C and 1,175°C as cited in the literature[25].

It was not possible to separate MC from $M_{23}C_6$ carbides during electrochemical extraction of precipitates but the combined volume fraction of these two carbides in the matrix of the standard heat-treated sample was about 1%. There was a slight increase in volume fraction of these carbides from the as received state. This could be due to the precipitation of $M_{23}C_6$ carbides which are non existent in the as received material.

The lattice constant of extracted γ' particles in the as received material as determined by X-ray diffractometer was 3.591Å and was slightly smaller in the fully heat-treated material (a_0 =3.589 Å) due to accompanying compositional adjustments. Solution-treating resulted in

partial dissolution of primary γ' precipitates and due to compositional adjustments the lattice constant of the primary γ' increased with increasing ST temperature as listed in Table 10. The expansion of the lattice could be due to diffusion of larger atoms like, Al, Ti, etc. into the precipitate. The carbide particles extracted from the as-received sample were found to be of the MC type (Ta & Ti based) by X-ray diffractometer. Another sample was aged at 950°C for 1,000 hours and the extracted carbides were found to be mostly $M_{23}C_6$ carbides (Cr based) by X-ray diffractometer. These particles were analyzed in an X-ray diffractometer and their lattice constant was measured and is reported in Table 10.

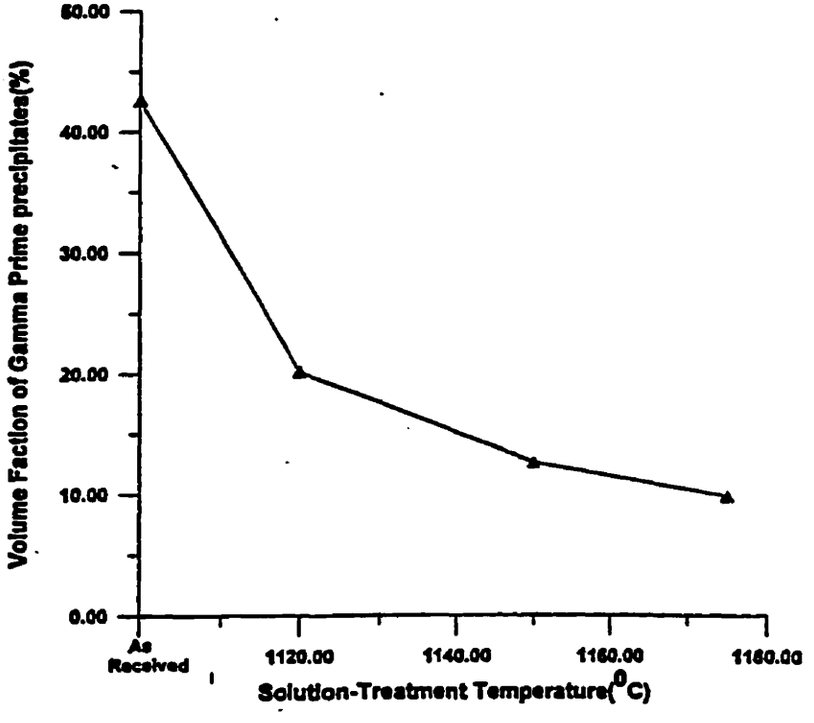

Figure 35 Plot of Volume Fraction as a Function of Solution-Treatment Temperature.

Table 10: Lattice constant of electrochemically extracted precipitates and the volume fraction data

No	Heat-Treatment	γ'+Carbides (% V.F.)	Carbides (% V.F.)	a_0 of γ'(Å)	a_0 of carbides (Å)
1	As Received	42.6	0.72	3.5907	MC→4.379 $M_{23}C_6$→ 10.69
2	1120^{0}C/2hrs(AC) /845^{0}C/24 hrs	42.8	0.91	3.58925	
3	1120^{0}C/2hrs/BQ	20.1	--	3.60001	
4	1150^{0}C/2hrs/BQ	12.6	--	3.60004	
5	1175^{0}C/2hrs/BQ	9.8	--	3.6025	
6	1120^{0}C/2hrs(AC)/845^{0}C/72 hrs	42.8	--	γ' → 3.588 γ → 3.5804	

BQ = brine quenched
AC =air cooled
V.F. = volume fraction

4.9 Coarsening Behavior of γ' Precipitates

4.9.1 Modified Lifshitz-Slyozov Wagner (MLSW) Theory of Coarsening Kinetics

According to the modified LSW Theory of precipitate coarsening, the coarsening rate is given by the following expression,

$$r - r_o = Km \frac{8}{9} \frac{D C_e V}{R T} t^n$$

Therefore, a plot of ln ($r-r_o$) vs ln t should result in a straight line if this theory is appiicable to the coarsening of γ' observed in the present study. The secondary γ' particles span from 20 nm to 145 nm in size whereas the primary γ' can be as large as 485 nm as their mean cubic edge length. The slope of the straight line would then give the coarsening rate constant 'n'. Figure 36 shows the logarithmic relationship between the primary and secondary γ' precipitate size and aging time at 845°C, following a solution treatment at 1,120°C. By regression analysis the best fitting straight lines were plotted and are shown in figure 36. It is seen that the value of n for the primary γ' cuboids was 0.042 as compared to 0.185 for the secondary γ' cuboids, which suggests two different coarsening rates for the two types of γ' particles. Although long term aging after 1120°C solution-treatment was not a part of this study, Footner et.al.[17] found that the size of primary γ' particles does not change significantly upto 1000 hours of aging time. Instead the secondary spheroidal γ' particles coarsened rapidly upto about 1000 hours of aging and attained a size of 160-190nm, before they dissolved abruptly. This was followed by the growth of unimodal primary γ' particles.

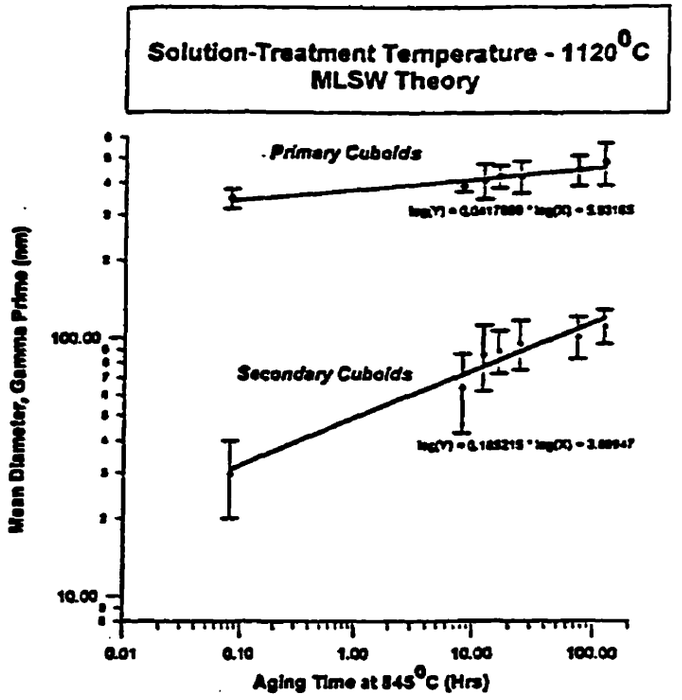

Figure 36 Mean Diameter (cubic edge length for the primary γ' and diameter for the secondary γ') γ' as a Function of Aging time at 845°C for 1120°C ST./2 hrs.

Figures 37 and 38 show the γ' coarsening kinetics (MLSW Theory) for samples that were aged at 845°C after a solution heat treatment at 1,175°C and 1,225°C ST respectively. The degenerate cuboids in these samples lie in the range of 90 to 320 nm. Figure 39 shows the variation in the size of primary γ' particles with ST temperature. The samples were brine-quenched to minimize the precipitation of secondary γ' particles. The mean γ' size first increased (coarsened) and then decreased with increasing temperature. Beyond 1,150°C, even most stable of the primary γ' particles began to dissolve and their size kept getting reduced. The primary γ' size for 1,225°C ST sample was only in the range of 80 to 120 nm. Thus it is concluded that the γ' solvus is definitely higher than the 1,160°C-1,175°C range, unlike the conclusion arrived by Steven and Flewitt[27].

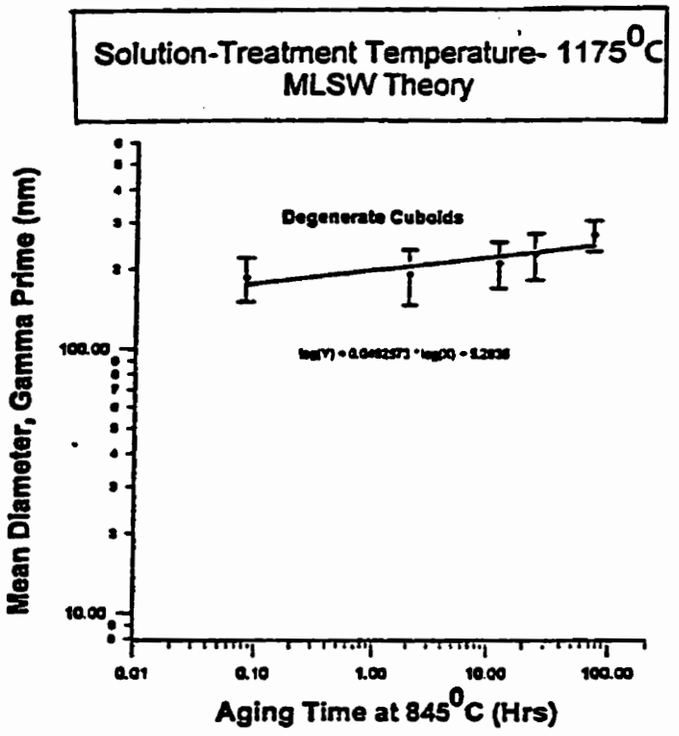

Figure 37 Mean Diameter (cubic edge length) of γ′ as a Function of Aging Time at 845°C for 1175°C ST./2 hrs.

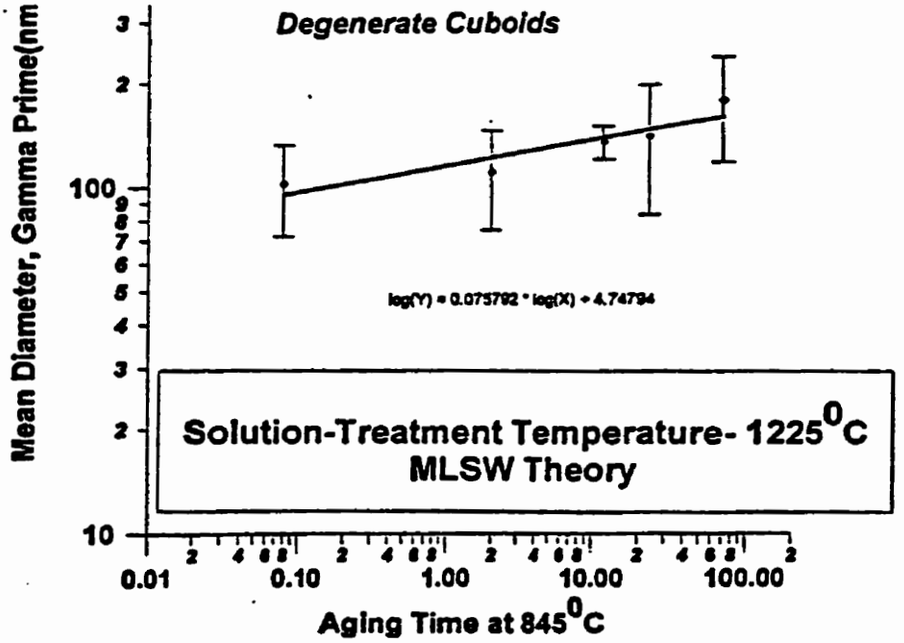

Figure 38 Mean Diameter(cubic edge length) of γ′ as a Function of Aging Time at 845°C for 1225°C ST./2 hrs.

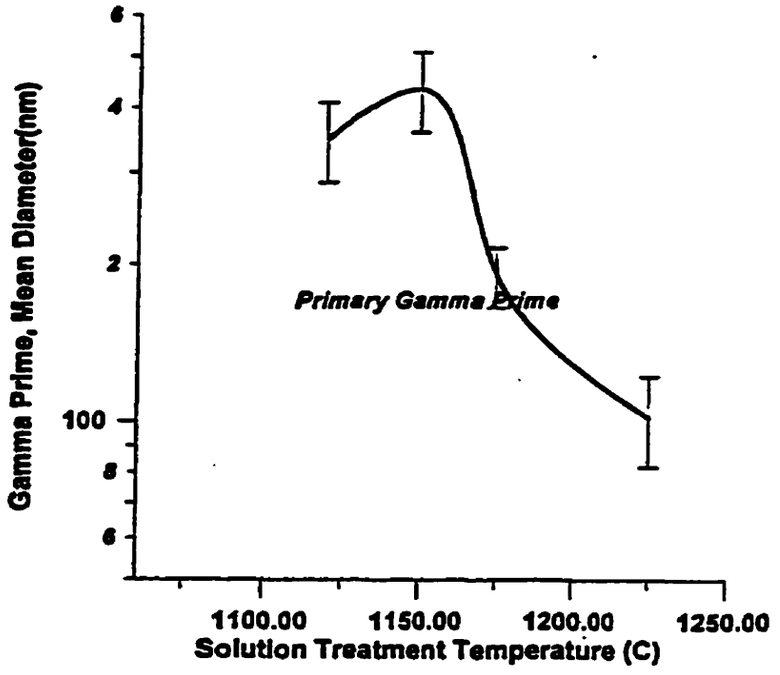

Figure 39 Variation of Primary γ′ Size with Solution-Treatment Temperature.

4.9.2. Lifshitz-Slyozov encounter modified (LSEM) Theory of Coarsening Kinetics

Another approach in developing an understanding of the coarsening of γ′ in Ni-base superalloys is the LSEM theory. The coarsening rate equation of the LSEM theory is as follows[17]:

$$\bar{r}^3 - \bar{r}_0^3 = K_e \frac{8}{9} \frac{D\gamma V C_e t}{RT}$$

If the above equation is applied to the present study, the plot of mean γ′ size as a function of $t^{1/3}$ should be a straight line. This behavior is observed in Figures 40 and 41. The relationship is approximately linear and small deviations can be attributed to the experimental error in the measurement process.

4.9.3 Calculation of Activation Energy for the Coarsening of Secondary γ′ Spheroids in the 1120°C Solution-Treated and Aged Specimen.

LSEM theory of coarsening was used to calculate the activation energy for coarsening of secondary γ′ spheroids. Data for coarsening of γ′ spheroids at 750°C and 950°C (aging) following 1,120°C solution-treatment were taken from literature [17]. The measured values on aging at 845°C were used in this calculation. The corresponding equation for coarsening can be written as,

$$\bar{r}^3 - \bar{r}_0^3 = K_i t \ , \text{or}$$

$$(\bar{r}^3 - \bar{r}_0^3)^{1/3} = kt^{1/3}, \text{where} \quad k = \left(\frac{2\gamma DCV^2}{\rho^2 RT}\right)^{1/3}$$

The activation energy was determined from the slope of a plot of $\ln(k^3T/C)$ against 1/T. The associated data and the calculations are shown in Table 11, 12 respectively. Figure 42 shows a plot of d as a function of $t^{1/3}$ which was used to calculate the value of '*k*' for the above equation. The activation energy of the coarsening process is calculated from Figure 43. The data for C, concentration of solute (γ′ forming elements) in equilibrium with a particle of infinite radius, is not available in the literature. Footner et al. have estimated C for Nimonic alloys and IN-739 to be 2×10^{-8} mol/m^3[17]. If it is assumed that this is the value for IN-738 then the value of activation energy for the coarsening of secondary γ′ is calculated to be 241 KJ/mol K.

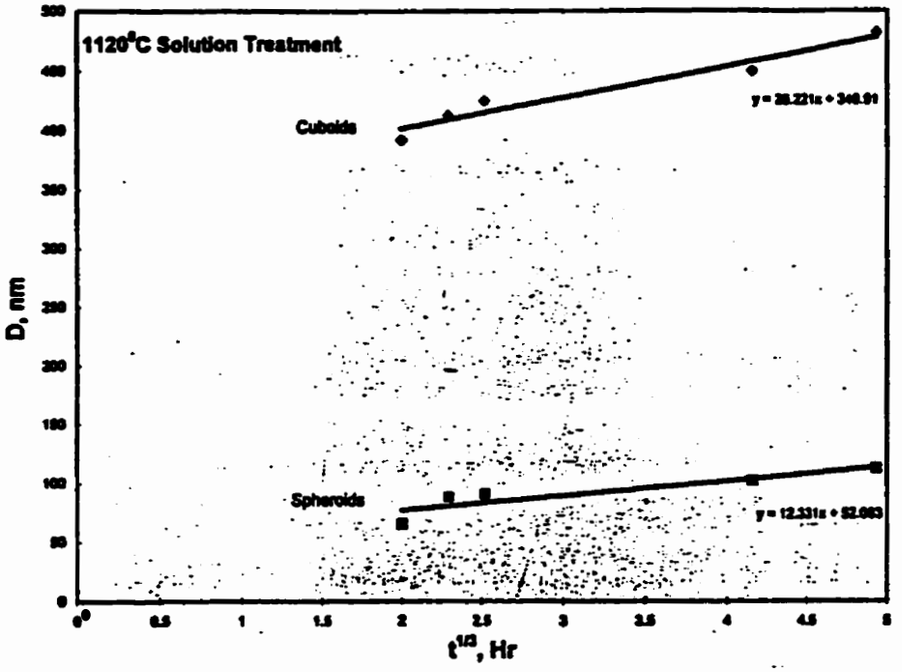

Figure 40 Coarsening Rate for γ′ Precipitates (LSEM Theory) for 1120°C STA.

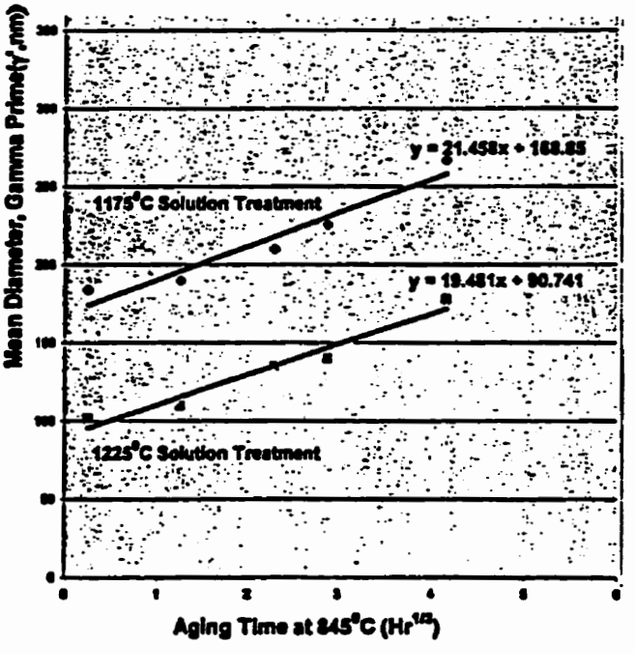

Figure 41 Coarsening Rate for γ′ Precipitates (LSEM Theory) for 1175°C and 1225°C STA.

Table 11 Secondary γ' Precipitate Size for Various Aging Temperatures and Lengths of Time

Temperature	Secondary γ' Diameter(nm)	$t^{1/3}$(hrs)
750°C[17]	31	3.72
	50	7.2727
845°C[Present work]	65	2
	87.5	2.289428485
	90	2.5198421
	102	4.160167646
	112	4.932424149
950°C[17]	35	7.2727
	92	10

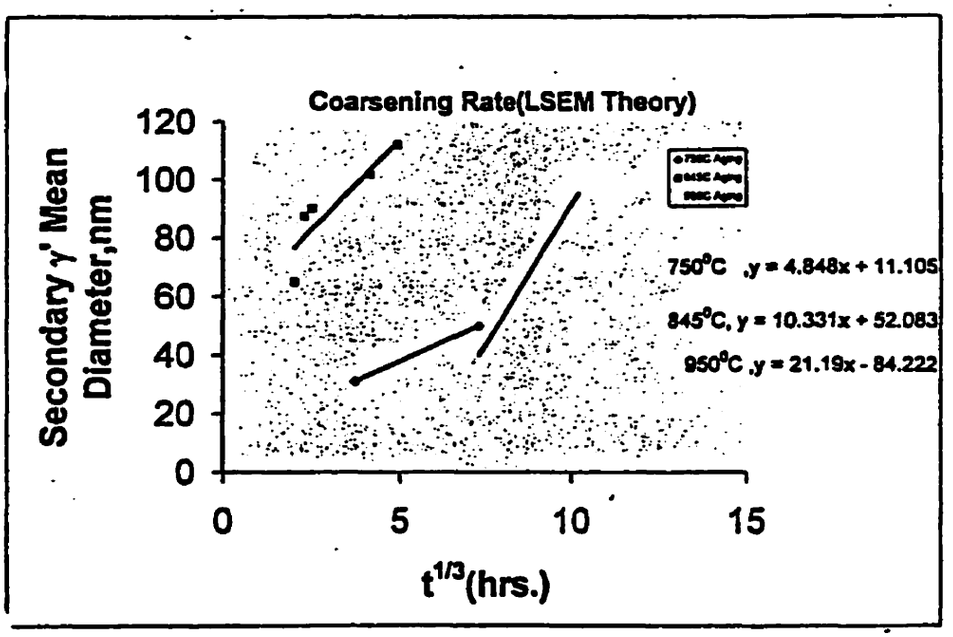

Figure 42 Plot of Particle Diameter with $t^{1/3}$ for Secondary γ' Precipitates

Table 12 Calculation of Parameters for Coarsening Rate (LSEM Theory)

T(°C)	T(°K)	k(Slope of d - t^1/3 plot)	C(approx.),mol/m^3	1/T(K^-1)	Ln(k^3 T/C)
750	1023	4.848	2.00E-04	0.00097752	22.4561208
845	1118	10.331	2.00E-04	0.00089445	24.84452219
950	1223	21.19	2.00E-04	0.00081766	27.08942854

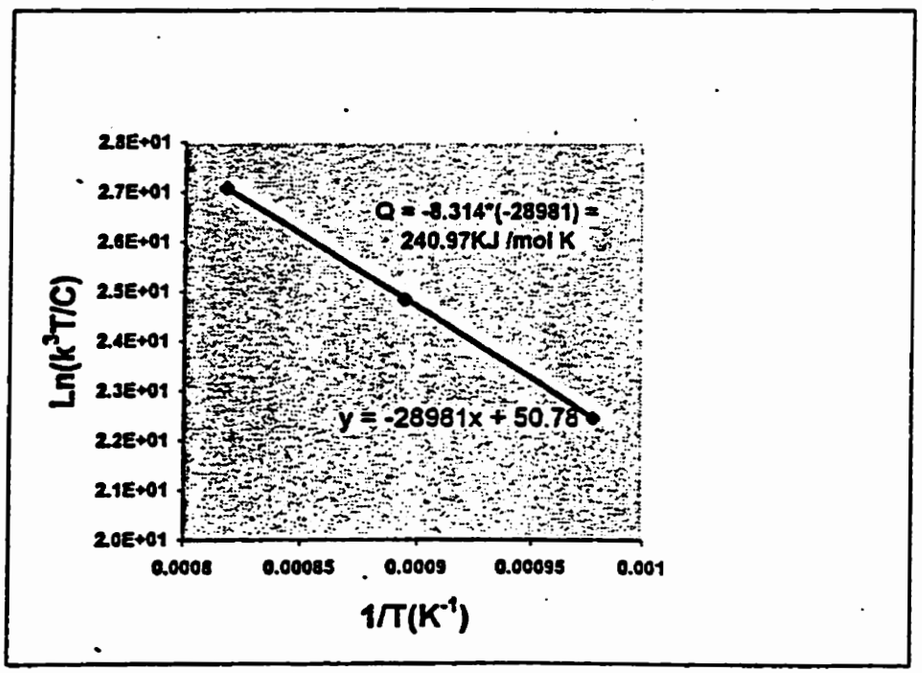

Figure 43 Plot of ($\ln k^3T/C$) with (1/T) for Activation Energy Calculation for Secondary γ′ Particle Coarsening.

4.10 Evaluation of Coherency Hardening in IN-738 as a Strengthening Mechanism

4.10.1 Calculation of Coherency Strain from the Misfit Strain δ

IN-738 is an extremely difficult-to weld alloy due to its susceptibility to microfissuring in the heat affected zone. The cracking was found to be caused mainly by the large shrinkage caused by the precipitation of γ′ particles as a result of cooling from the γ′ solvus temperature[43]. Thus it is important to quantify this shrinkage strain, or the coherency strain. Referring to the data for the overaged sample given in Table 10, the misfit is given by, $\delta=(a_{\gamma'} - a_{\gamma})/ a_{\gamma'}$, and is equal to 0.0029. The coherency strain, $\varepsilon =(2/3\delta)$ is 0.00193 for this overaged sample. Using the value of a_{γ} for the 1120^0C solution-treated and aged sample from Table 10, the value of ε for the standard heat treated sample was calculated to be to be 0.003233.

4.10.2 Calculation of Coherency Strain Using the Precipitation-Hardening Equations

Individual linear conversion of hardness to yield or flow stress is valid for some materials in particular strength ranges. On this basis, there exists a relationship of the type, $\sigma y \approx 2Hv$, for IN-738,[27]. From this approximation it is possible to calculate the coherency strains due to secondary γ′ precipitation. These calculations are tabulated in Table

13. The procedure was as follows:

Assuming $\sigma y \approx 2Hv$, the incremental flow stress due to secondary γ' precipitation can be evaluated as $\Delta\tau \approx 2\Delta Hv$. Another assumption made here is that the solid-solution hardening contribution remains nearly the constant for the underaged, peakaged, and overaged conditions[27].

By, rewriting the equation 29 from the literature review[36] one arrives at,

$$|\varepsilon| = [\frac{\Delta\tau}{3G}]^{2/3}(\frac{b}{rV_F})^{1/3},$$

where G is the shear modulus($7.4 \times 10^{10} Nm^{-2}$), b is the Burger's vector (0.254nm), V_F is the volume fraction of secondary γ' precipitates, and r is the γ' particle radius[27]. From equation 21 in literature review, the critical strain ε_c for IN-738 containing 45% volume fraction of γ' particles is calculated to be 0.003197.

If this value is compared with the coherency strain ε obtained for the overaged sample in Table 10 which is 0.00193, ε is 62% of ε_c, and therefore it is obvious from the discussions in the literature review (section 2.9.4) that order hardening also contributes significantly to the hardening process in IN-738. Assuming a 50-50% contribution from the misfit hardening and order hardening, $\Delta\tau$ in the above equation is taken to be half the incremental flow stress due to secondary γ' precipitation, and the calculated coherency strain values are reported in the last column of Table 13. Figures 44, 45 and 46 show the variation in hardness H_v, the inter-particle spacing (primary/secondary γ') L and the coherency strain ε with aging time for 1,120°C, 1,175°C and 1,225°C solution treatment, respectively. It is seen from Table 13 that coherency strains are the highest for the hardest sample while the interparticle spacing

(secondary γ') is the lowest. The inter-particle spacing begins to increase after the peak aging time due to coarsening and competitive growth. The coherency strains were higher for 1,225°C ST sample as compared to 1,175°C ST sample. One more thing worth noting is the fact the calculated coherency strain for the overaged sample in Table 13 is 70% of the coherency strain computed using the misfit strain. This error could be due the last assumption made involving a 50-50% contribution from coherency and order hardening.

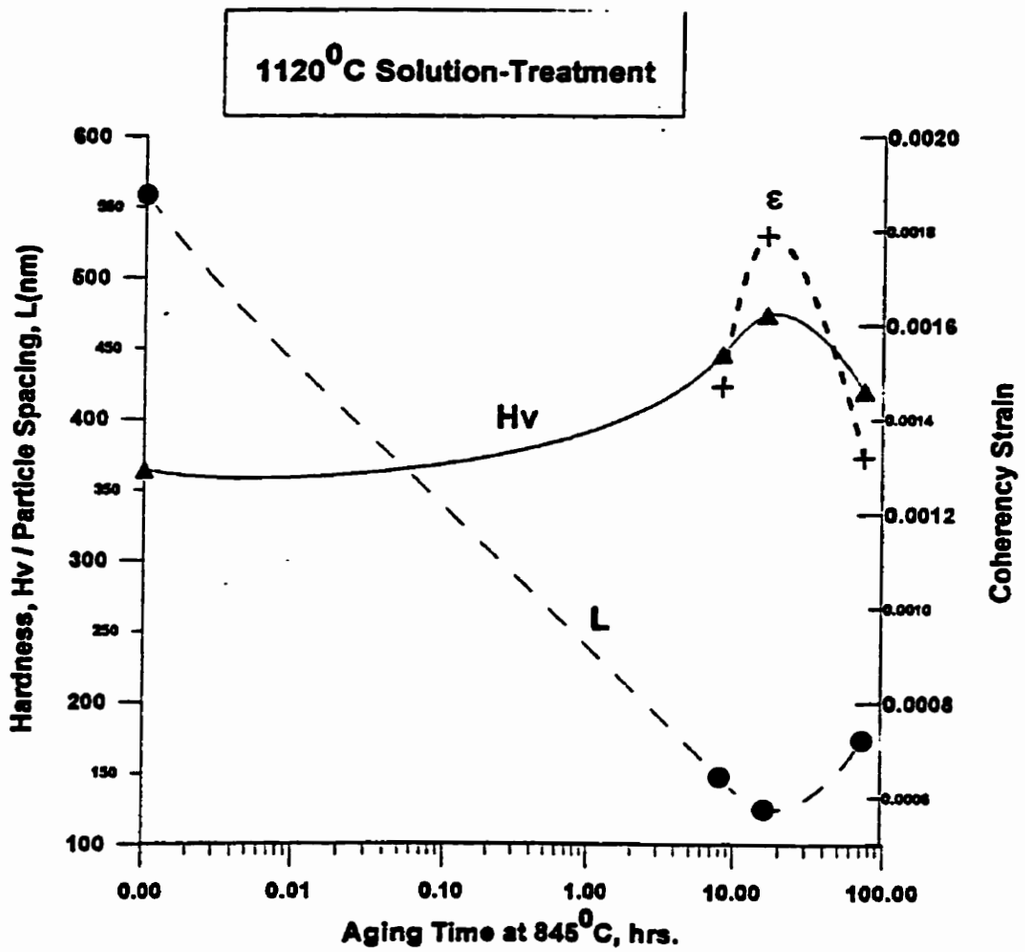

Figure 44 Variation in Hardness, Particle Spacing and Coherency Strain with Aging at 845 °C following solution-Treatment at 1120 ° C.

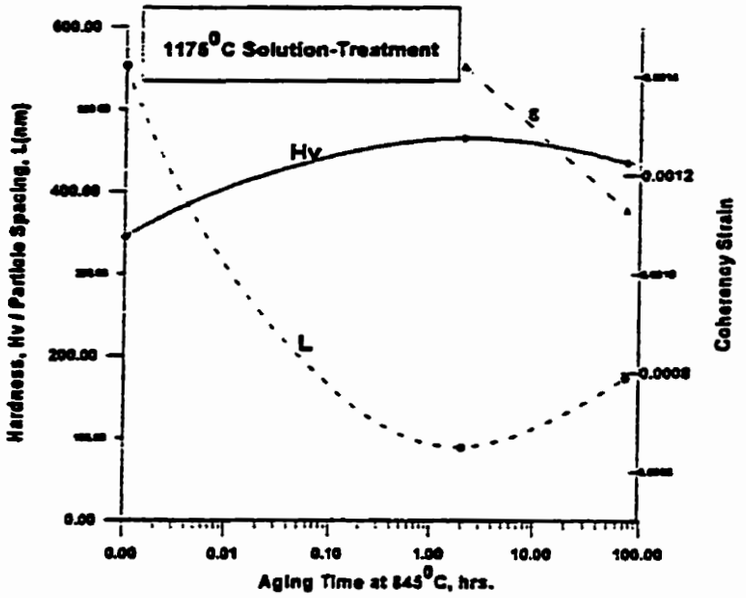

Figure 45 Variation in Hardness, Particle Spacing and Coherency Strain with Aging at 845 °C following Solution-Treatment at 1175° C.

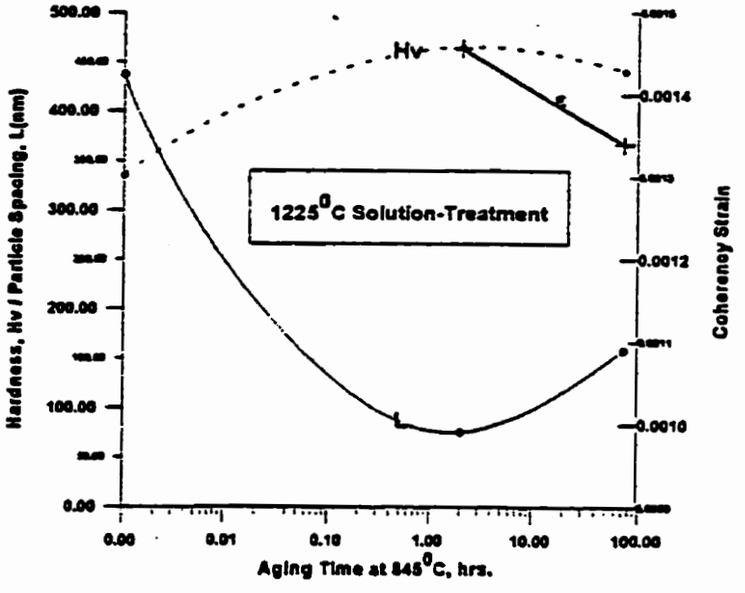

Figure 46 Variation in Hardness, Particle Spacing and Coherency Strain with Aging at 845 °C following Solution-Treatment at 1225° C.

Table 13: Calculation of coherency strain as a function of heat treatment for IN-738

Heat - Treatment	Precipitation Nature					
	Cuboidal primary γ' (VF / size (nm))	Spheroidal secondary γ' (VF / Size (nm)	Hardness Measured, Hv*	Particle Spacing, L(nm)	$\Delta\tau \sim 2\Lambda Hv$ (Mpa)**	Coherency Strain (ε) $
1120^0C/2 hrs (B.Q.)	20/347	---	364	558.87	---	---
1120C/2/845^0C/8 hrs (A.C.)	20/412.5	15/70	446	147.9414	164	0.00147
1120^0C/2/845^0C/16hrs (A.C.)	20/425	23/90	474	125.2065	220	0.00179
1120^0C/2/845^0C/72hrs (A.C.)	20/450	23/125	420	173.898	112	0.00132
1175^0C/2 hrs(B.Q.)	9.8/184	---	345	552.68	---	---
1175^0C/2/845^0C/2 hrs(A.C.)	9.8/213	33/100	465	89.05749	240	0.00142
1175^0C/2/845^0C/72 hrs(A.C.)	9.8/318	33/195	435	173.6621	180	0.00113
1225^0C/2 hrs(B.Q.)	4.95/90	---	335	437.5048	---	---
1225^0C/2/845^0C/2 hrs(A.C.)	4.95/90	38/105	465	75.41313	260	0.001456
1225^0C/2/845^0C/72 hrs(A.C.)	4.95/90	38/220	440	158.0085	210	0.00134

* 30 Kg Load
** Increment in Flow-Stress due to the precipitation of secondary gamma prime precipitates.
$ Constrained Lattice Strain, $\Delta\tau$ used in this calculation is half the $\Delta\tau$ listed in the previous column.
A.C. Air Cooling
B.Q. Brine Quenching

4.11 Inter-Granular Cracking in IN-738 due to Quenching Stresses

Figures 47(a-c) show inter-granular cracking in a sample solution-treated at 1,225°C and brine-quenched. The situation was the same for 1,150°C and 1,175°C ST samples. A high cooling rate from 1,225°C did not allow the precipitation of grain-boundary $M_{23}C_6$ as observed in Figure 47(b). Liquation of grain-boundary MC carbides also assisted in crack coalescence as seen in Figure 47(c).High aging contraction stress occur in IN-738 along with the quenching stresses when the samples are brine-quenched from the solution-treatment temperatures. These stresses are sufficient for the initiation and propagation of inter-granular cracks along the boundaries with or without $M_{23}C_6$ carbides for the specimen solution-treated at temperatures of 1,150°C and above.

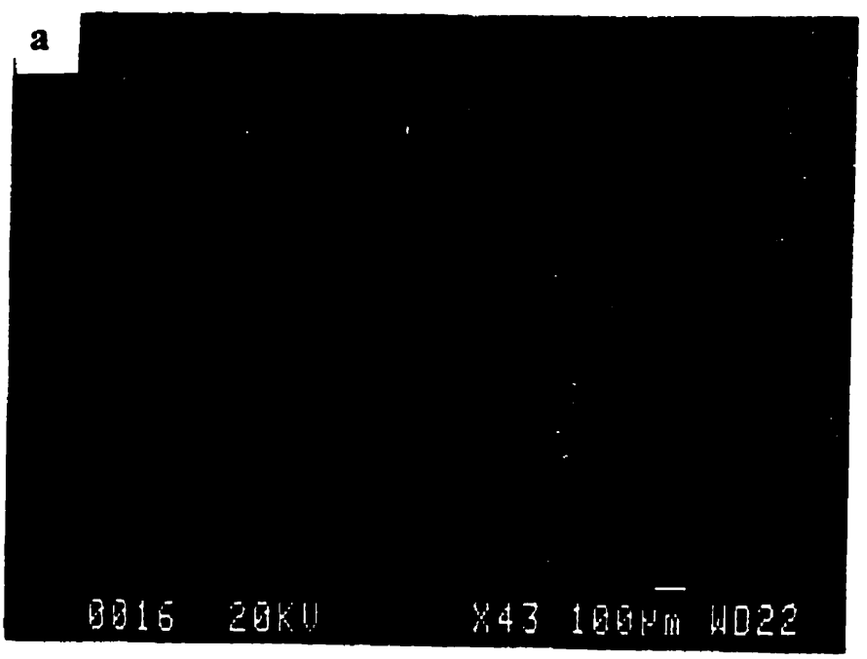

Figure 47 (continued)

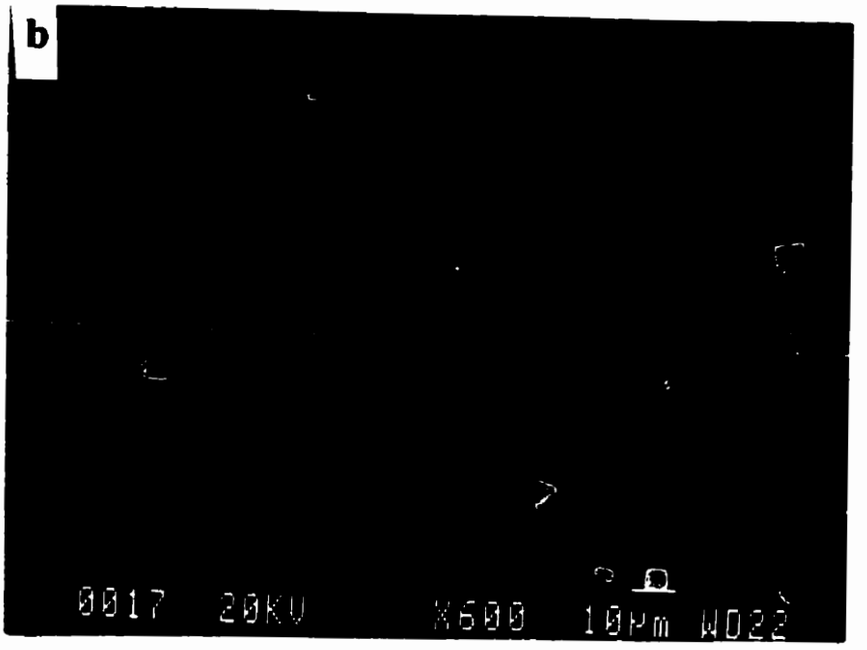

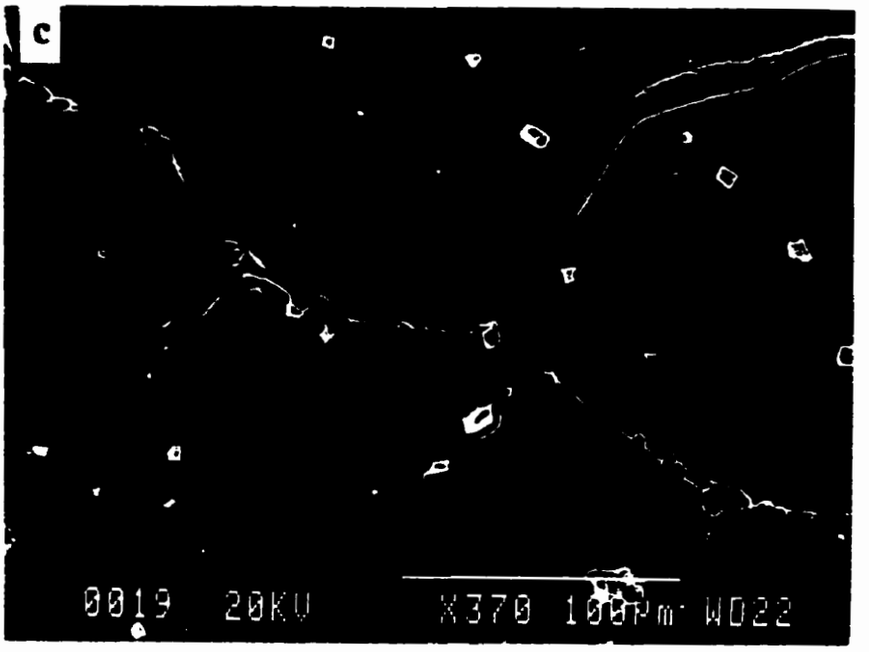

Figure 47: Inter-Granular Cracking in a Sample Solution-Treated (a) at 1225°C/BQ, (b) SEM Micrograph Showing Clean Grain Boundaries Free from $M_{23}C_6$

Precipitation, (c) SEM Micrograph Showing Liquation of Grain Boundary Carbides that Enhanced Crack Linkage and Propagation.

The observed intergranular cracking is attributed to the presence of shrinkage or the aging contraction stresses. A higher solution-treatment temperature of 1,225°C takes almost 40% volume fraction of γ' into solution, and depending on the cooling rate, due to its inherent extremely fast precipitation kinetics, secondary γ' particles precipitate in a very fine spheroidal form in various sizes ranging from a few to about 50 nanometers, and with varying volume-fractions.

Intergranular cracking also occurred on quenching specimen from a temperature of 1,060°C, which had a continuous film of $M_{23}C_6$ carbides on the grain boundaries. Therefore an overaged sample (1,120°C/2hrs (A.C.)/ 845°C/72 hrs) was further aged at 1,060°C for half an hour and then water quenched. The overaging produced a semi- continuous film of $M_{23}C_6$ carbide particles on the grain-boundaries. The temperature of 1,060°C is slightly above the solvus of $M_{23}C_6$ and resulted in some dissolution/globulization of $M_{23}C_6$ particles. The quenching step following this treatment was not aided by aging contraction (shrinkage) stresses since secondary γ' precipitation did not occur.

Figure 48(a & b) still show the presence of grain-boundary cracks. The possible explanation is that the $M_{23}C_6$ particles liquated at 1,060°C resulting in the formation of grain boundary liquid film. This film would be extremely weak and embrittling[44,45] and

with minimal quenching stresses result in grain-boundary cracks during cooling. The resolidified film of $M_{23}C_6$ can be observed along the grain-boundary crack in a high magnification micrograph, Figure 48(c). A semi quantitative EDS analysis showed that the film region was richer in Chromium, Molybdenum, Niobium, Tantalum and tungsten and had a lower concentration of Aluminum and Titanium as compared to the matrix. This also suggests that the zone near the grain-boundary could be a γ' free zone which is basically $Ni_3(Al, Ti)$.

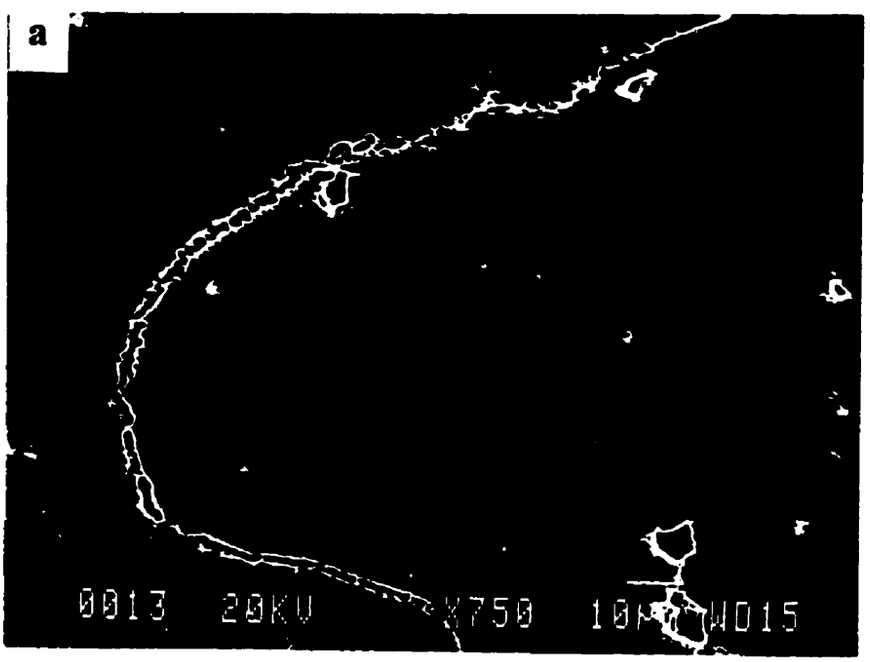

Figure 48 (continued)

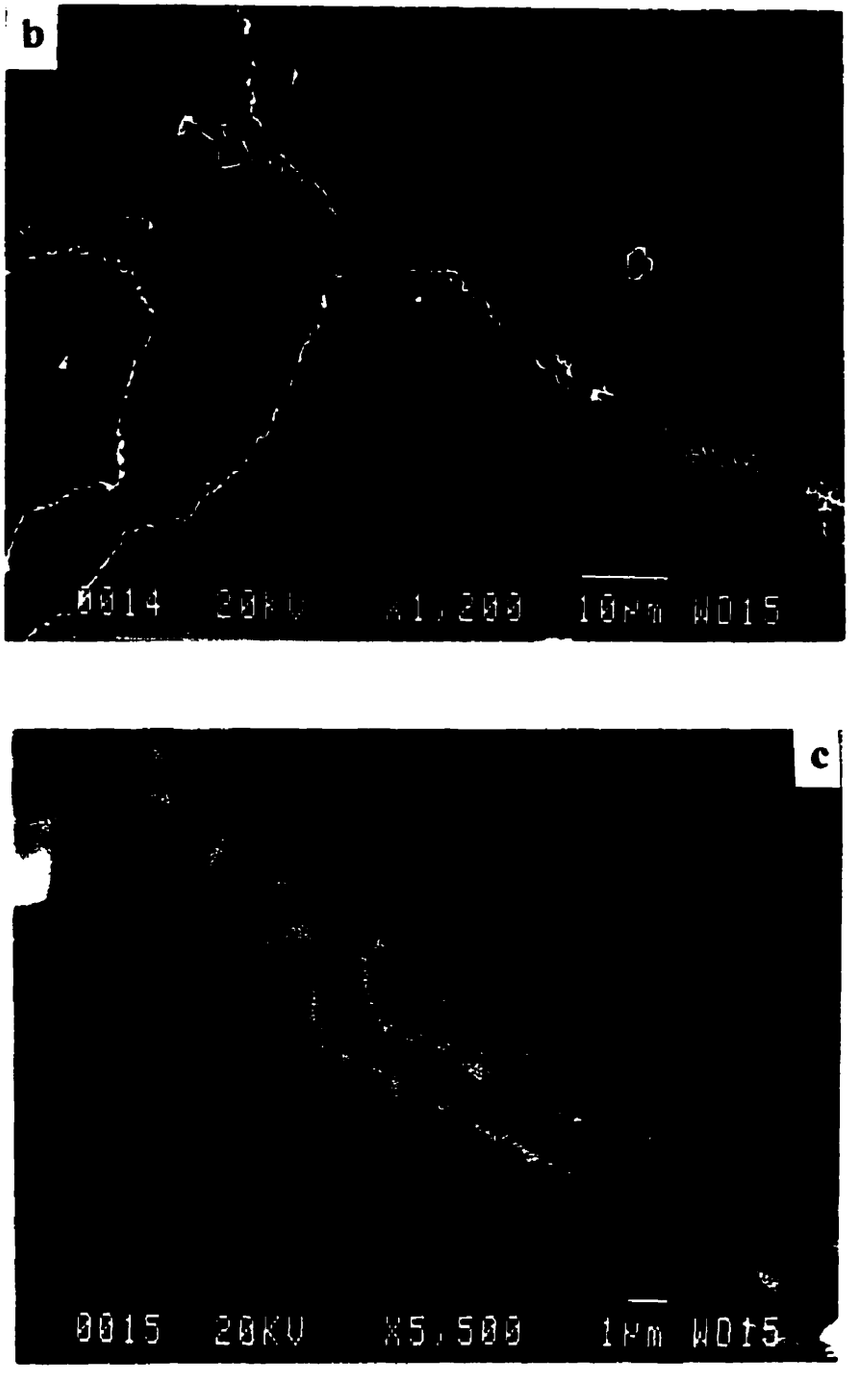

Figure 48: SEM Micrograph Showing (a) Semi-Continuously Cracked Grain Boundary, (b) Continuous Grain Boundary Crack due to $M_{23}C_6$ Liquation and Tear, (c) High Magnification SEM Micrograph Showing Resolidified Grain Boundary Liquid Film.

4.12 General Conclusions of Microstructural Analysis

As received Microstructure

a) The cast IN-738 billet contained dendritic grains at the periphery and central equiaxed grains with a large grain size. The dendritic microstructure was cored. The interdendritic region was found to be rich in γ′ forming elements such as Al and Ti.

b) The casting micropores occupied a volume fraction of about 0.5%, and owing to the larger grain size of the material do not adversely affect the mechanical properties.

c) Figure 16b shows the absence of fine $M_{23}C_6$ carbide particles, both in the grain interior and on the grain boundary.

d) The TEM micrograph of figure 16d shows an approximately cuboidal and unimodal γ′ precipitate morphology. The volume fraction of these γ′ particles was about 42%.

Solution-Treated Microstructure

a) The grain structure showed a reduced coring with solution-treatment and reduced further with increased solution-treatment temperatures. The grain size increased by 50% at the highest solution treatment temperature. The volume-fraction of primary γ′ particles decreased consistently with increasing ST temperatures but remained a visible fraction at ST temperature of 1225^{0}C. The size of primary γ′ particles first increased with increase in ST temperature from 1120^{0}C to 1150^{0}C, and then decreased with further increase in temperatures.

b) The specimens solution-treated at 1175^{0}C and 1225^{0}C and aged marginally (10

minutes) at 845^{0}C showed the presence of discrete, globular $M_{23}C_6$ carbide particles along the grain boundaries (figure 21b). This observation suggested that the dissociation of primary carbides began during the ST (2 hrs.) step, and since the $M_{23}C_6$ solvus is below the ST temperature, it could precipitate out only during the aging step.

c) The samples solution-treated and brine-quenched at 1150^{0}C and above showed extensive quench cracks along the grain boundaries (Figures 47(a-c)). The quenching stresses, combined with aging-contraction stresses due to secondary γ' precipitation locally along the grain-boundaries, are the most likely causes for such a reaction. A heavy precipitation of fine secondary γ' particles along the grain-boundaries instantly hardens the grain-boundary region locally. The resulting brittle boundary deforms heterogeneously with the matrix under the influence of quenching stresses and gets cracked. Further, the liquated primary carbide particles on the boundaries act as the potential sites for crack initiation.

Solution-Treated and Aged Microstructure

a) The primary MC carbide particles were not stable at the aging temperatures following the ST step. The carbide particles reacted with the matrix at the interface to form secondary γ' particles in the matrix, and $M_{23}C_6$ carbide particles on the grain boundaries. The primary carbide was a Ta based carbide as opposed to $M_{23}C_6$ carbide which was Cr based. The carbon atoms diffused away from the dissociating primary carbide and precipitated on the grain-boundaries as shown in Figure 20a. Very few secondary carbide particles were noted in the grain interior. On the contrary, a highly overaged sample

(Figure 20b) showed a different dissociation reaction altogether, where the primary carbide reacted with the matrix to produce finer MC carbide particles. The resulting MC carbides then followed the usual dissociation reaction and transformed into grain interior $M_{23}C_6$ carbide particles. The precipitation of grain-interior carbide particles could be associated with the already saturated grain-boundaries with the similar carbide particles.

b) The underaged specimens showed a discrete precipitation of $M_{23}C_6$ carbide particles on the boundaries. This carbide distribution changed quickly to a continuously linked particle network on the boundary for the peak-aged specimen.

c) An overaged specimen, 1120^{0}C STA, when subjected to a temperature of 1060^{0}C (5 minutes) and quenched showed grain-boundary cracks(Figures 48(a-c)). These cracks were caused due to the liquation of continuously linked $M_{23}C_6$ carbide particles, at 1060^{0}C, which is above the solvus for $M_{23}C_6$ (1025^{0}C). The quenching stresses acted on the already liquated, brittle film along the boundary and caused tears. Another overaged specimen when held at 1060^{0}C for half an hour instead, and quenched, showed much reduced cracking. The grain-boundaries $M_{23}C_6$ carbide particles dissolved/globulized at the above solvus temperature treatment. The resulting discontinuously liquated particles on the grain boundaries could not link up to form a grain boundary film.

d) Aging for 24 hours at 845^{0}C (1120^{0}C ST) provided for the growth of primary cuboidal and secondary spheroidal γ' particles resulting in a distinct bimodal distribution (each about 20% volume fraction). This heat-treatment has been accepted as the standard one and results in the peak aged condition.

e) The overaged sample for the 1175^{0}C and 1225^{0}C ST showed unimodal distribution of

degenerated γ′ particles indicating that the growth was competitive and that they eventually joined the primary ones and grew together.

f) The extraction replica images in Figures 33(a-d) show that the overaged cast IN-738 contains a noticeable volume-fraction of eutectic islands. These regions had a γ′ particle distribution quite different from that observed in the matrix, which is the major strengthening phase in this material. These regions would, therefore, deform differently than the matrix depending upon the local strength, and result in an inhomogeneous deformation. This aspect needs to be examined in greater detail and ways and means must be found to minimize the presence of these eutectic islands, in solution treated and aged condition.

g) Footner et al. found that for long term aging of γ′ particles in cast IN-738, LSEM theory gave the best fit to the experimental data. Therefore, LSEM theory was used in this study to calculate the activation energy for short term coarsening of secondary γ′ particles. The value for the activation energy is comparable with the activation energy for coarsening of γ′ particles in some other Ni base superalloys.

h) The principal cause of heat affected zone microfissuring in this material is shrinkage / misfit strain resulting from the precipitation of secondary γ′ particles during cooling from the welding temperatures[43]. Thus a measure of coherency strain provides a measure to evaluate the susceptibility of the material to HAZ cracking during weld repairs.

Chapter 5

CONCLUSIONS

1) The as-received cast IN-738 had a coarse grain-size (about 600μm) and a cored dendritic microstructure with a small volume-fraction of casting micropores. The primary MC carbide (Ta based) occupied a volume-fraction of about 0.7%. The grain-boundaries were devoid of any secondary carbide particles. The unimodal and approximately cuboidal primary γ′ particles occupied a volume-fraction of about 42%.

2) The grain-size increased marginally from 700μm to 900μm for the solution-treated specimens at temperatures of 1120^{0}C and above and upto 1225^{0}C. The grain-boundaries were still devoid of any secondary carbide particles but showed some liquated primary carbide particles. The volume fraction of primary γ′ particles solution-treated at temperatures in the range of 1120^{0}C-1225^{0}C decreased progressively from 20.1% to about 5%. The volume-fraction analysis indicated that the solvus of primary γ′ particles was higher than the 1160^{0}C-1175^{0}C range suggested by Steven and Flewitt[27].

3) The brine quenched samples from the solution-treatment temperatures showed extensive intergranular cracking. Quenching stresses along with aging contraction stresses due to an inherent fast precipitation kinetics for the secondary γ′ particles were responsible for the observed cracking.

4) The grain-size remained constant at the aging temperatures. The primary MC carbide particles lost their integrity at ST temperatures and dissociated profusely to produce fine secondary $M_{23}C_6$ particles with aging. These secondary carbide particles initially occurred as discrete particles on the grain-boundaries and with continued aging changed to a continuous distribution on the grain-boundaries. Only long term aging showed the presence of these particles in the grain interiors. Aging resulted in the growth of γ' particles. Only the ST temperature of 1120^0C showed a distinct bimodal distribution. The overaged microstructure for the 1175^0C and 1225^0C consisted of a unimodal distribution of degenerate γ' particles.

5) The activation energy for the coarsening of secondary γ' particles using the LSEM theory was 241 KJ/mol K and is in a reasonable agreement with the value of 259KJ/molK calculated by Henderson etal.[45].

6) The solvus temperature of grain-boundary $M_{23}C_6$ carbide particles was found to be about 1025^0C and they liquated/dissolved at higher temperatures. The liquation of continuously linked fine carbide particles on the grain boundaries resulted in the formation of a brittle liquid film on the grain boundary. An overaged specimen when reheated to a temperature of 1060^0C and quenched, again showed extensive intergranular cracking. This time the cracking was due to the tearing of the grain-boundary liquid-film formed due to the melting of continuously linked fine carbide particles on the boundaries (overaging phenomenon), when the quenching stresses (negligible shrinkage stresses due to the

absence of secondary γ' precipitation) acted on the brittle film.

7) The sensitivity of cast IN-738 to HAZ microfissuring can be directly related to the amount of coherency strains in the material due to secondary γ' precipitation. These strains were always lower for the overaged material compared to the peak-aged and the underaged material.

REFERENCES

[1] Bieber,G.C. and Mihalisin,R.J., 2nd International Conference of on the Strength of Metals and Alloys, Asilomer, ASM Vol. IV, p. 1031.

[2] "Alloy IN-738: Technical Data" INCO,New York, p. 1-11.

[3] Fahrmann ,M., et al.,1995, Acta Metall.,Vol.43.,No.3, p. 1007.

[4] Gandin,A., et al., Met. Trans. A, Vol. 26A, 1995, p. 1543.

[5] Qiu,Y.Y.,1995,Scripta Mettalugica *et* Materialia,Vol.33,No.12, p. 1961.

[6] Standard Aerospace Ltd., Private Communication.

[7] Koul,A.K. and Gessinger,G.H.,1983, Acta Metall.,Vol. 31,No.7, p. 1061.

[8] Kelly, A, Nicholson, R.B., eds., 1971, 'Strengthening Method in Crystals' John Wiley and Sons, INC., Newyork, p. 12.

[9] Ardell,A.J.,Metallurgical Trans.,Vol.16A,Dec.1985, p. 2131.

[10] Sullivan,P.C. and Donachie,M.J.,1966,Metals Engineering Quaterly,1967, p. 250.

[11] Metals Handbook,Vol.2 ,10th Edition,ASM International, p.1143.

[12] Garosshen,T.J. and Mccarthy,G.P., Met. Trans. A, Vol. 16A, 1985,p. 1213.

[13] Standard Aerospace Ltd., Private Communication.

[14] Rebecca,A.M. and Ebert,L.J., Scripta. Met. Vol. 17, 1983, p. 1983.

[15] McColvin,G.M., Oct. 1977, Metal Science, p. 447.

[16] Duvall,S.D. and Owczarski,W.A.,1971,Welding Research Supplement, p. 401.

[17] Footner,P.K. and Richards,B.P.,Journal of Material Science 17(1982), p. 1007.

[18] Donachie,J.M.,Jr., Superalloys, Metals Park, Ohio, ASM 1984, p. 102.

[19] Hoffelner,W., et al., Z. Werkstofftech. 10, 1979, p. 84.

[20] Larson,J.M.,1976,Metallurgical Trans.,Vol. 7A, 1976, p. 1497.

[21] Bradley, E.F. ed., "Superalloys: a Technical Guide" Metals Park, Ohio, ASM International, 1988, p. 58.

[22] Castillo,R. and Koul,A.K., High Temperature Alloys for Gas Turbines and other Applications, 1986 II (Proc. Conf.), Liege, Belgium, p. 1395.

[23] Venkateswaran,P.K. et. al.., Mater. Sci. Eng. , 1973, 11, p. 255.

[24] Rong,Y.H., et al., Electron Microscopy 1986, Vol. 1[Proc. Conf.], Kyoto Japan, 1986, p. 879.

[25] Koul ,A.K. and Castillo,R.,Metallurgical Trans.,Vol.19A,Aug. 1988, p. 2049.

[26] Koul,A.K. and Thamburaj,R., 1984,Metallurgical Trans., Vol. 16A,1985, p. 17.

[27] Steven,R.A. and Flewitt,P.E.J.,Journal of Material Science 13(1978), p. 367.

[28] Gerold,V. and Haberkorn,H., Phys. Stat. Sol., 16, 1966, p. 675.

[29] Pollock,T.M. and Argon,A.S., Acta. Metall. Vol. 40,1, 1992, p. 1.

[30] Tien, J.K. and Copley,S.M., Met. Trans. Vol. 2, 1971, p. 215.

[31] Chung,W.D. and Chaturvedi,M.,1971,Metal Science Journal,Vol.6,1972, p. 134.

[32] Mukherji,D.,Jiao,F.,Chen,W. and Wahi,R.P., 1990,Acta Metall.,Vol . 39, No.7,1991, p. 1515.

[33] Pandey,C.M.,Satyanarayana,V.V.D. and Taplin,M.R.D.,Materials Science and Technology,Nov. 1994, p. 936.

[34] Merrick,H.F., Met. Trans., Vol. 4, 1973, p. 885.

[35] Kriege,O.H. and Sullivan,C.P., Trans. ASM, 1968, Vol 68, p. 278.

[36] Nembach,E. and Neite,G., 'Precipitate hardening of Superalloys by Ordered Particles', Progress in Materials Science, Vol. 29, 1985p. 213.

[37] Cho,G. and Ku,S., ' Elasticity effects on the microstructure of alloys containing coherent precipitates', Progress in Materials Science, Vol. 40 No. 2, 1996, p. 124.

[38] Yafang,H., 'The coarsening behavior of γ'' and γ' particles in IN-718' , M.Sc. Thesis, 1981, p. 40.

[39] Smallman,R.E., 'Modern Physical Metallurgy' published by Butterworths, London, III[rd] ed., 1970, p. 433.

[40] DeHoff,T.R.,Braun,D.J. and McCall,L.J.,Microstructural Science,Vol.11, p. 79.

[41] Quested,P.N., Henderson,P.J. and McLean,M.,ActaMetall.,Vol.36, No.10,1988, p. 2743.

[42] Stolz,W.,Kny,E.,Stickler,R. and Goretzki,H.,J.Vac.Sci.Technology, 17(5),1980, p. 1208.

[43] Haafkens,M.H. and Matthey,G.H.,Welding Journal ,Nov.1982, p. 25.

[44] Radhakrishnan,B. and Thompson,R.G., Scripta Metallurgica, Vol. 24, 1990, p. 537.

[45] Nakkalil,R., et al., Scripta Metallurgica Vol. 26, 1992, p. 1599.

[46] Mukherji,D.,et al., High Temperature Materials for Power Engr. 1990, II (Proc. Conf.), Liege, Belgium, p. 1067.

[47] Stevens,R.A. and Flewitt,P.E.J., Acta Metall. Vol. 29, 1981, p. 867.

[48] Henderson,P.J. and Mclean,M., Acta Metall. Vol. 31, No. 8, 1983, p. 1203.